Nanoscale Thermal Management with Hybrid Nanostructure Using Bio Nano Process

February 2017

CHAO HE

Graduate School of Materials Science

Nara Institute of Science and Technology

Abstract

Development of nanoscale heat control methods and devices featuring an operating principle which proactively utilizes the heat generation on a nanoscale is strongly expected. Under a thermoelectric field, understanding the nanoscale behaviors of heat transport, and controlling and using the characteristics thereof will become strongly important. In the nanoscale, the heat transport in a material should be treated in terms of the transport of phonons. There are several ways to control heat transfer such like fabrication of nanostructure. However, some nanostructure's scale is less than the mean free path of phonons (1 nm-100 μm), the correct understanding of heat transfer and designing is impossible unless transport of phonons are controlled. Therefore, in this study, the purpose is to ensure the establishment of a nanocomposite structure with hybrid of organic and inorganic materials for controlling the thermal conductivity. However, a finely controlled nanostructure is difficult to realize. Therefore, bio nano process (BNP) was utilized to fabricate the nanostructure due to uniform protein ferritin shape and capacity.

Fabrication of distance controlled nanoparticle array

BNP was utilized to fabricate the nanostructure and bring in the hybrid of organic and inorganic materials. As optimized conditions, ferritin concentration of 0.01 mg/ml and ammonium acetate ion concentration of 10 mM, were used in the experiment. In order to control a separate distance (SD) of nanoparticles (NP), polyethylene glycol was modified on ferritin surface. The PEG-ferritin with molecular weight of 2k, 5k, 10k and 20k were dropped on the samples and held for 3 min. During this incubation

time, PEG-ferritins adsorbed on to the SiO_2 surface. Then, the solution was removed utilizing the spin coater. Finally, the NPs on the samples were observed using SEM (Fig. 1). To analyze the distribution of NPs, the radial distribution function (RDF: g'(r)) was introduced into this study. The calculated RDF using SEM images are shown in Fig. 2. As the results shown, SD increase along with PEG weigh increase. In solution, length of PEG is much longer than Debye length of ferritin, which means repel force of PEG became main reason for SD control.

Thermal conductivity of nano-composite film

For investigation of thermal conduction by nanostructures, effect of grain boundary and electric current should be avoided, therefore, amorphous insulator material SiO_2, was selected as a thin film material. PEG20k-ferritin was chosen to fabricate nano-composite structure, due to mean free path of SiO_2 have a large distribution range (10 nm-1 μm). After the control of protein distribution, SiO_2 was deposited directly on PEG-ferritin with iron core. The processes were repeated. The samples within 0, 3 and 5 layers of protein were fabricated. The nanostructure was confirmed by cross-sectional TEM images (Fig. 3). The dots in the SiO_2 film show the white shell and black core which were assumed as protein ferritin with PEG and FeO_x NPs, respectively.

After setup and optimization of 3ω measurement system, samples were evaluated for thermal conductivity in out-plane direction. Changes of thermal conductivity (Δκ) were contrasted between nanostructure with and without organic shells (Fig. 4). And the results of measurement indicated

that protein shell have efficient effect on phonons scattering, thus thermal conductivity decrease. On the other side, thermal conductivity increased due to NPs material which have a higher thermal conductivity than film. The organic shell can cut off the phonons at mean free path of the layer thickness.

Conclusion

According to results, hybrid nanostructure using BNP can control a materials' thermal conductivity by protein shell or different core materials. Hybrid nanostructure show excellent performance for protein in nanoscale scattering phonon effectually, and thermal conductivity was decreased much.

Acknowledgements

First of all, I am very grateful and thankful to Prof. Yukiharu Uraoka, my principal adviser, for his supervision, continuous guidance, and kind encouragement through discussions for the duration of this work.

I would like to express my gratitude to Prof. Ichiro Yamashita, Prof. Hisao Yanagi and Assistant Prof. Takashi Matsuo for their supervision and critical comments for improving this thesis.

I am also indebted to Assistant Prof. Yasuaki Ishikawa for technical support and helpful advices. I wish to express my deepest thanks and appreciations to Assoc. Prof. Mutsunori Uenuma for helpful discussions, valuable advices, precious guidance and technical supports. I am also indebted to Assistant Profs. Masahiro Horita, Assistant Profs. Mami Fujii and Juan Paolo S. Bermundo for their helpful supports.

I am very appreciate Mr. Fumio Okamoto, Mr. Ryoichi Honda, Mr. Ryota Matsuyama, Dr. Hiroki Kamitake Ban and Dr. Takahiko, for their kind advices and technical supports during this work. And express gratitude to Prof. Hideaki Adachi, Mr. Tomotsugu Yoshida, Mr. Shunsuke Takenouchi, Mr. Hiroyuki Nagao, Mr. Shun Okazaki, Mr. Toyoda Kenichi, Mr. Yuma Karaki and Mr. Yuki Hashima, for their kind advices in discussions.

I would like to express my appreciation of Ms. Yukiko Morita and Ms. Fuyuko Takao for their great support and kindness in my daily work. I would also like to extend my gratitude to Mr. Noritaka Koike, Ms. Yoshiko Nishikawa, Ms. Sakiko Fujita, Mr. Yasuo Okajima, Mr. Kazuhiro Miyake,

and Mr. Masahiro Fujihara for technical help.

I sincerely acknowledge Prof. Ctirad Uher, Mr. Si Hui, Dr. Hang Chi and all members of the Ctirad Uher research group in the University of Michigan, for their support, technical advice, and helpful discussions while I was in Ann Arbor, USA.

I would like to extend my great appreciation to Dr. Yasuhiko Shinoda, Mr. Naoto Kuriyama, Mr. Ayumi Iwata and Ms. Hisashi Mizuno from Toyoda Gosei Co. for their pioneering work and instruction regarding device fabrication. I deeply thank Mr. Shinji Araki, Mr. Yuta Fujimoto, Mr. Yuki Tawa, Mr. Xudongfang Wang and Mr. Daiki Senaha as the members or ex-member of TE group for helpful discussions and technical help.

Thanks should also appreciate Dr. Li Lu for her helpful advice and supports. I wish to acknowledge Dr. Emi Machida, Dr. Yumi Kawamura, Dr. Satoshi Saijo, Dr. Yoshihiro Ueoka, Dr. Koji Yamasaki, Dr. Takahiro Doe, Dr. Haruka Yamazaki, Dr. Koji Yoshitsugu, Dr. Yana Mulyana, Dr. Satoshi Urakawa, Mr. Keisuke Kado, Mr. Kyohei Nabesaka, Mr. Seiya Yoshinaga, Mr. Daisuke Hishitani, Mr. Yukihiro Osada, Mr. Yunjian Jiang, Mr. Chaiyanan Kulchaisit, Ms. Kahori Kise, Mr. Yang Liu, Mr. Shunsuke Uchiyama, Mr. Itaru Raifuku, Ms. Hiromi Okada, Mr. Yuki Tada, Mr. Song Zhang, Mr. Kento Oikawa, Mr. Yusuke Kawamura, Mr. Yuta Tominaga, Mr. Kazuki Noguchi, Mr. Takuya Akano, Mr. Takuya Oshima, Mr. Kenta Komari, and all members in the various laboratories for their understanding and for sharing good times during this research work.

Finally, I would really like to thank my parents, wife, daughters and all my

families and friends for their understanding, support, and encouragement.

Table of Contents

● Chapter 1

1 Introduction

1.1 Background

Along with the increase of awareness of the deleterious effect of global warming on the planet's environment, a renewed requirement for long-life electrical power sources and high efficiency devices is becoming clear. Around 34% of the total energy consumed from primary energy sources such as fossil fuels are effectively used while the remaining 66% is released to the natural environment as waste heat in the world today. Particularly, the waste heat below 150 ℃ almost takes over 50% in total waste heat. Low temperature waste heat is difficult to utilize because it is localized and diluted. Thermoelectric converter can just convert thermal energy into electric energy. Thus, the studies of thermoelectric have attracted more and more attention. Thermoelectric conversion is an excellent way to harvest waste heat for power generation.

Thermoelectric studies started in 1821 when the Seebeck effect is discovered. However, the efficiency in current thermoelectric research is still too low for wide application. New materials and their structures have been found recently and on the basis of presented novel properties, thermoelectric devices will be widely used in short future.

There are three important effects in thermoelectric effect; Seebeck effect ($V=S\cdot\Delta T$ where V is generated voltage, S is Seebeck coefficient, ΔT is the difference of temperature), Peltier effect ($q=\pi\cdot I$ where q is thermal current, π is Peltier coefficient, I is electric current) and Thomson effect ($q=\beta\cdot I\cdot$

ΔT, where q is thermal current, β is Thomson coefficient, I is electrical current, ΔT is the difference of temperature). This study focuses on Seebeck effect by which heat energy can be converted into electrical energy. And the π structure is always composed of thermoelectric device (Fig. 1.1).

Recently, because of the development of theoretical and computational methods, the thermoelectric efficiency has been greatly improved. Applications of thermoelectric effect have almost become possible, although challenge. One of the basic problems is the thermoelectric figure-of-merit, $ZT=\sigma S^2T/\kappa$, where σ is electric conductivity, κ is thermal conductivity which consists of lattice thermal conductivity κ_p and electron thermal conductivity κ_e. This figure-of-merit can provide the efficiency or performance of a thermoelectric material. Therefore, the evaluation of a thermoelectric material is defined by σ, T and κ. But these parameters are not independent, for example the optimization of Seebeck coefficient for materials will change the electrical properties. Some process such as doping can increase the density of electrons, thus σ increased, but Seebeck coefficient and thermal conductivity will also change (Fig. 1.2). Thus, optimization of ZT is the most difficult problem.

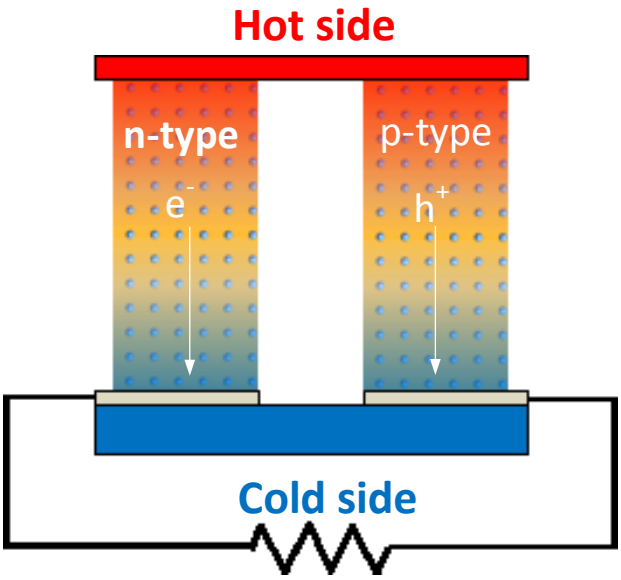

Figure 1.1 π structure of thermoelectric device.

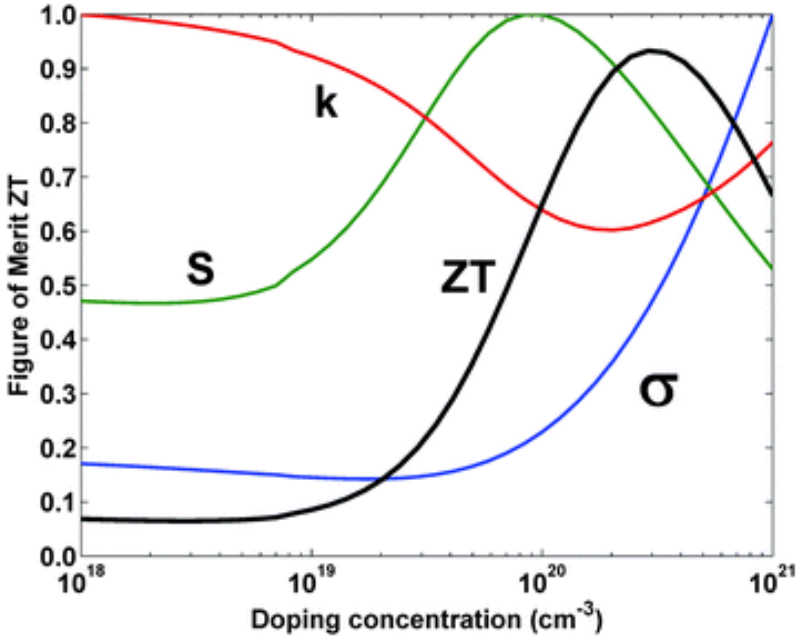

Figure 1.2 Normalized thermoelectric properties and *ZT* versus doping concentration at 300 K for n-type $Si_{80}Ge_{20}$.

According to recent developments in thermoelectric materials, it is possible that this problem will be overcome soon. The thermoelectric field has gotten

remarkable developments in improving thermoelectric properties due to the recently gained possibility to fabricate nanostructured materials such as quantum dots[1], superlattices[2], nanowires[3, 4], and nano-composites[5–8]. The highest value of *ZT* in recent report can almost reach up to 2.8, since one way to achieve high efficiency is nano-composited material. The common point for all these researches is the reduction of thermal conductivity. However, nanoscale thermal analysis is very difficult, especially, the nanoscale thermal analysis in amorphous materials. The heat transport in a material should be treated in terms of the transport of electrons and phonons. For electrons, from the Wiedemann-Franz law:

$\kappa_e = LT\sigma$ (1-1),

where κ_e is thermal conductivity by electrons, L is Lorenz number, T is temperature, σ is electrical conductivity, we know current of electrons work for thermal conduction. On the other hand, phonons' contribution to thermal conductivity can be written as the following formula

$\kappa_L = \frac{1}{3}\int_0^{\theta_D/T} C(x)\nu l(x)dx$ (1-2),

where κ_L is thermal conductivity by phonons, θ_D is Debye temperature, *C(x)* is specific heat for phonons at frequency x, ν is group velocity of phonons, $l(x)$ is the mean free path for phonons at frequency x. The formula 1-2 is under Debye approximation which fit acoustic phonon modes, except optical phonon modes which have minute contribution to thermal conductivity because of low group velocity. For an isotropic system, the common formula for both acoustic and optical phonon modes is

$\kappa_L = \frac{1}{3} C v l$ (1-3).

The Wiedemann-Franz law can describe pure metal perfectly in all temperature regions and do main contribution of thermal conductivity for normal metal and degenerate semiconductor (Figure 1.3). But for nondegenerate semiconductors and insulators, phonons mainly work for thermal conduction. Furthermore, in thermoelectric field, the dimensionless figure-of-merit can be written as $ZT = \frac{S^2}{L}(1 + \frac{\kappa_L}{\kappa_e})^{-1}$ (1-4)[12].

From formula 1-4, we know that the figure-of-merit increase along with the decrease of thermal conductivity in phonons' part. Therefore, this research focuses to reduce thermal conductivity by phonons. The concept of phonons is rather old since it was discovered around the beginning of the 20th century. Nevertheless, the understanding and the control technologies of heat based on phonons were much delayed compared to electronic properties and optical properties, since deep understanding and control have rarely been necessary for device development to date. Especially for thermoelectric materials, one of the most important ways to obtain improvement of the systems' efficiency is to introduce nanostructures into materials[9-11], to reduce thermal conductivity. In all examples of nanostructures, nanoporous or thin films including organic or inorganic nanoparticles are made of not only materials with well electric properties such as BiTe but also materials which are supposed to be insulator such as SiO_2, *a*-Si, etc.[13-15] The data about thermal conductivity and electrical conductivity for materials indicate that there are advantages and disadvantages for both organic and inorganic materials

(Figure 1.3). Organic materials usually have low electrical and thermal conductivity while inorganic materials are on the opposite spectrum. Consequently, the mixture of inorganic and organic materials can be expected as a great improvement for both thermal and electrical properties.

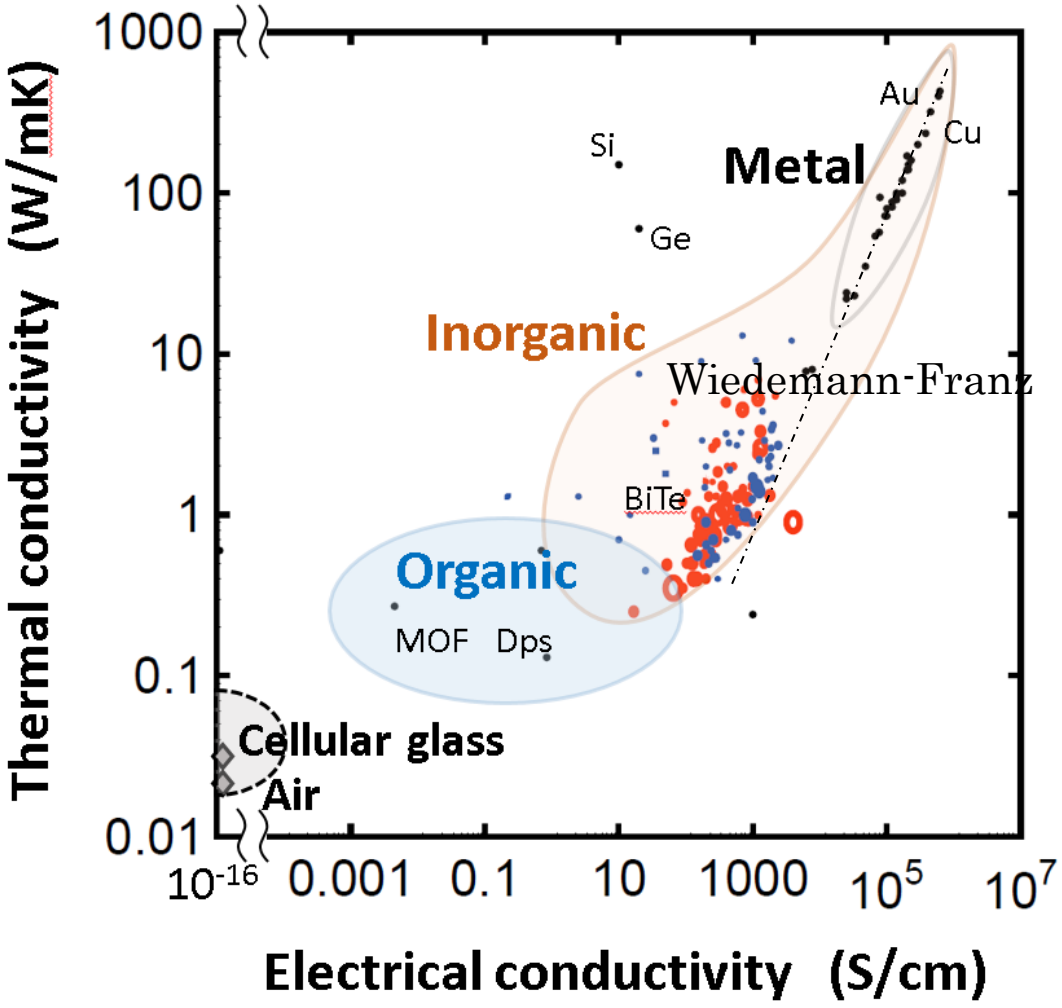

Figure 1.3 Relation between thermal conductivity and electrical conductivity for different materials[16].

1.2 Nanoscale Thermal Conduction

Although thermal conduction at nanoscale is becoming progressively notable along with nano-technology improvements, there are several typical issues such as ensuring that nanoscale devices functionally and reliably work. The study of nanoscale thermal conduction not only benefits the thermal conductivity decrease in thermoelectrics but also consists of critical evaluation of nanoscale electronic devices. Even though the analysis of nanoscale thermal conduction becomes increasingly important for refinement of electronic devices. The problems of heat generation and dissipation by miniaturized devices on a nanoscale work as limiting factors against advanced performances. To resolve such problems, the development of nanoscale heat control methods is strongly expected. In the thermoelectric field, how to control thermal flow by nanostructures can enable more efficient energy conversion.

Even though scale is the sole difference, thermal conduction in macro- and microscales is significantly different. Because when the scale of the structure is near the phonons' mean free path or wavelength, the classical rule for thermal conduction may not be so accurate[17, 18]. For example, the Fourier law ($q = -k\nabla T$) fails when predicting nano-composited structure. Therefore, in the present proposal, the purpose is set out to ensure the innovation of materials and devices by deepening the understanding of heat in the nanoscale region from the perspective of nanoscience, thereby establishing heat control and utilizable technologies. Here, the new theoretical discipline to manipulate the transport of phonons and control the transport of heat by

handling the heat transport with the manipulation of phonons and using artificial structures will be utilized as phonon engineering.

The strategies to reduce thermal conductivity are to decrease the specific heat and average group velocity by changing the dispersion relations or shortening the mean free path by boundary or interface scattering as known from formula 1-3. All these three parameters are related with each other by the phonons' frequency (formula 1-2) or scale of the artificial nanostructure[12]. Therefore, this study discuss the thermal conductivity from the mean free path (MFP) and nanostructure's scale. MFP can be written as

$$l(\omega) = v\tau(\omega) \quad (1\text{-}5)$$

where $\tau(\omega)$ is the relaxation time at frequency ω. The behavior of thermal conduction is totally different depending on the different wavelengths of phonons. For instance, phonons with a wavelength comparable to or smaller than the atoms' distance scale, have high energy and short MPF. All those phonon modes does not contribute much to heat transfer because of U process (Umklapp-process) and scattering by boundary or impurities. These modes are called thermal conductivity accumulation[19-21]. For *a*-Si, the thermal conductivity accumulation's MFP band is predicted in the region of 10 nm-1 μm. If the phonons' MFP is much shorter than nanostructure scale or roughness, the phonons' behavior will appear as diffusive transfer mode. On the other hand, if the phonons' MFP is comparable to or longer than scale or roughness of nanostructure, the phonons' behavior will appear as ballistic transfer mode. Furthermore, in the condition of wavelength much longer than nanostructure scale or roughness, the phonon acts as classic wave mode, and

coherent effects can be observed easily[22]. All these relations between phonons' wavelength and nanostructure scale can be comparable to the relation between phonons' MFP and nanostructure unit scale which will be discussed later in chapter 5.

1.3 Bio Nano Process

Organisms including us, consist of organic and inorganic matters which are highly self-organized. This bottom-up type structure with higher order has various properties such as physiological functions or excellent mechanical properties. Proteins, very important components of organisms, are organized by 20 kinds of amino acids, which have various appearances and functions. Organisms use the mechanism by which protein can be synthesized mistake-free by gene sequence. Proteins has also have direct relationships with the organism performance, thus, without right transcription, the organism's functions and structures cannot be kept stable. Similar to the fabrication process of nanostructure, the uniform structure is a critical point to be expected.

This research also focuses on Bio Nano Process (BNP) which uses proteins to fabricate nanostructure. BNP is a biological technology using biomineralization of biological supramolecule, which is highly self-organized and selectively adsorbed, to fabricate nanostructure. Biomineralization is the process by which living organisms produce minerals. These minerals often form structural features such as seashells and the bone

in mammals and birds. Through BNP, there are several methods to create nanostructure as follows:

(1) Spherical shell proteins or viruses including cavities, are used to synthesize nanoparticles or nanorods, etc. inside the things by biomineralization. The inorganic materials synthesized inside cavities should be synthesized uniformly according to structure of biological supramolecules which are used as template materials.

(2) According to the technology of self-organization or selective adsorption, create the designed structure using biological supramolecules.

(3) Finally, after the biological supramolecules are removed by thermal treatment or film deposited, etc. functional nanostructures will be created.

There are a lot of devices such as one electron transistor[23], ReRAM (resistive random access memory) [24, 25], Dye Sensitized Solar Cell (DSC) [26], thermoelectrics[27], etc. that have been fabricated by BNP, most recently. According to schematic figures of BNP (Figure 1.4), BNP is a combination of bottom-up technology using protein and top-down processes such as photolithography, to fabricate difficult nanostructures. Furthermore, the next-generation devices are expected. Even though there are many kind of biological supramolecules such as proteins, virus, etc, in this research, cage protein ferritin was used as biological supramolecules.

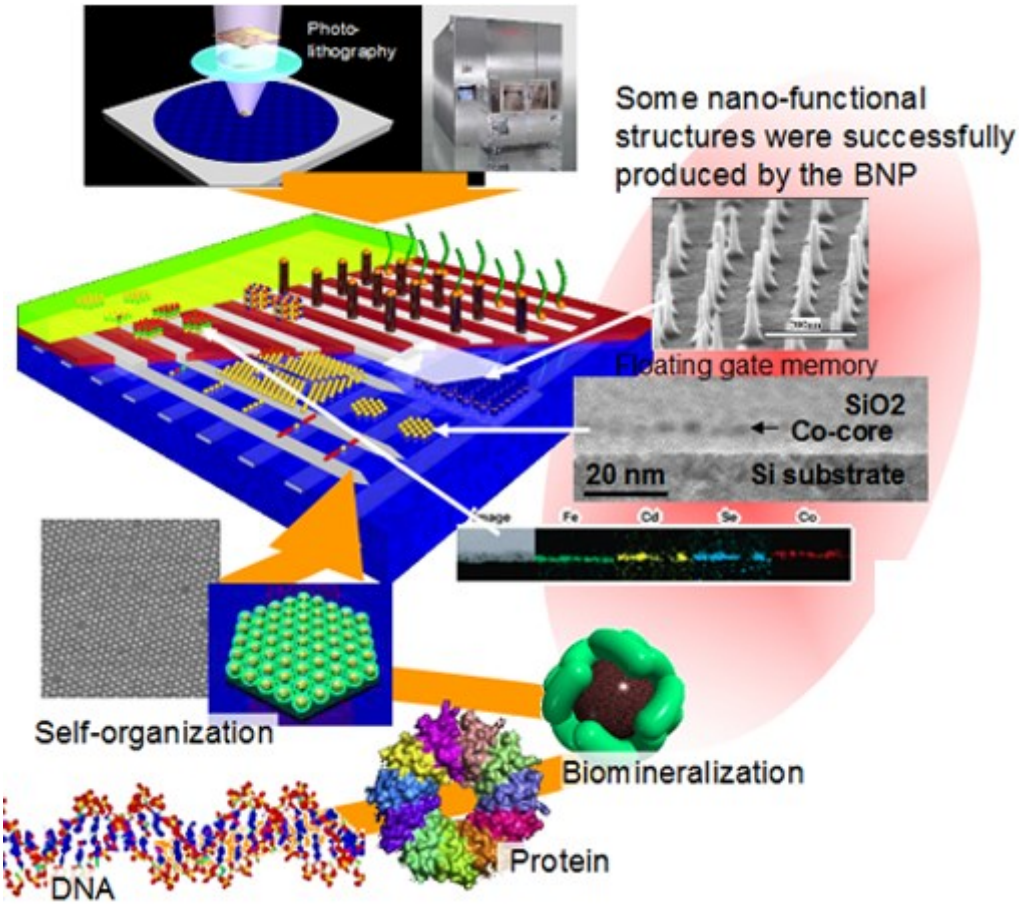

Figure 1.4 Schematic figures of Bio Nano Process[28].

Ferritin is a universal intracellular protein which stores or releases iron in a controllable process to keep the iron balance in living organisms. The protein is produced by almost all living organisms, including algae, bacteria, higher plants, and animals. For human beings, it acts as a buffer against iron deficiency and overload. Ferritin is self-organized by 24 monomer-subunit of protein and the molecular weight is about 460000 Da. These subunits have two types, the light (L) and the heavy (H) type with an apparent molecular weight of 19 kDa or 21 kDa, respectively. In this study, the ferritin we used only consists L type subunits and is known as L-ferritin, because L-ferritin

has better thermal stability. The residues on N-terminal of the subunit are considered as a reason for structural instability when pH value is changed. Recombinant ferritins (Fer4, Fer8) where 4 or 8 residues are removed from ferritin's N-terminal amino acid are also widely used. The shape of ferritin is cage-like with inner-diameter about 7 nm and outer-diameter about 12 nm[29] (Figure 1.5). There are some oxidation states in the active site on ferritin's subunit. At these positions, after oxidation of ferrous ions, ferrihydrite ($5Fe_2O_3 \cdot 9H_2O$) consisting of about 4000 iron atoms exist inside ferritin is considered to have a crystal structure. Ferritin without ferrihydrite core is called apoferritin.

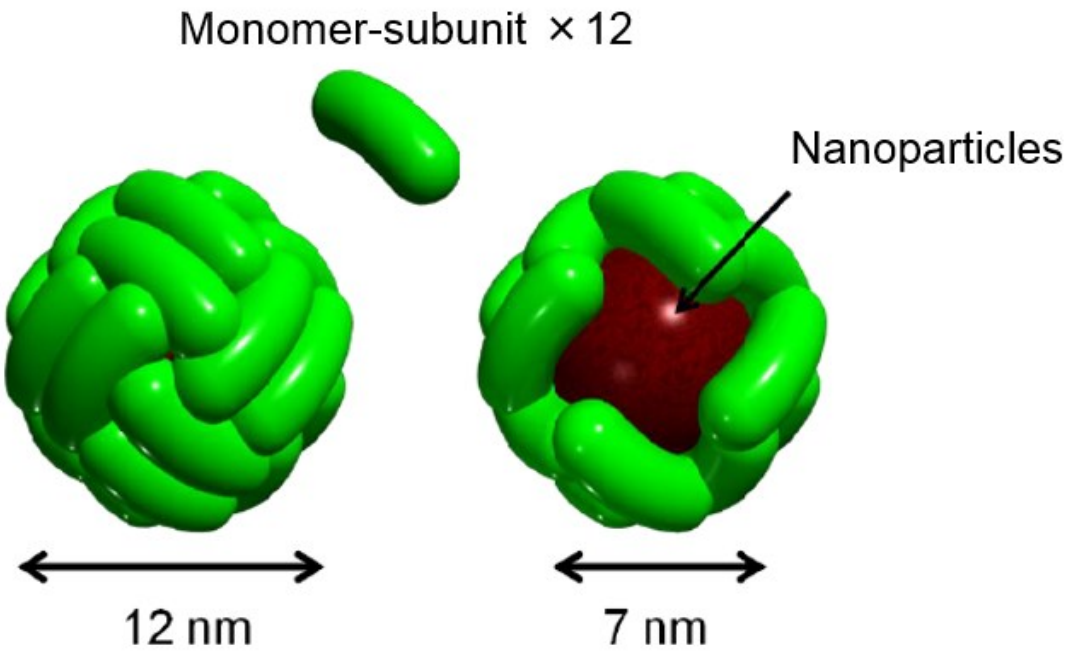

Figure 1.5 Schematic figure of ferritin.

In nature, ferritin contains iron ions, but it also has ability to contain other

metal ions in order to synthesize many kinds of nanoparticles as previously reported. For instance, oxides such as Co_3O_4, NiO_x, InO_x, etc. or sulfides such as Au_2S, CdS, etc. have already been reported as ferritins' possible cores. Through this method, uniform nanoparticles can be created because the synthesis is almost only occurs inside the ferritin. The ability of adsorption on ferritin surface can be improved by changing the gene sequence. On the other hand, the attachment surface also can be modified in order to fabricate nanoparticles' distribution pattern from one to three dimensions. Furthermore, surface of ferritin also can be modified to create nanoparticles' distribution which will be introduced in chapter 2.

1.4 Purpose of This Study

Along with refinement of devices and materials to nanoscale, nanostructure should be employed as a solution for problems in nanoscale thermal conduction. Therefore, analysis of thermal conduction in nanostructure is necessary. However, behaviors of thermal conduction in nano size are different from those in bulk. It is necessary to establish a new understanding that should be referred to as the thermal nano-science and the thermal nano-engineering. For the thermoelectric field, in all main research directions of thermoelectric conversion, there are two primary approaches taken to overcome thermoelectric low figure-of-merit challenges. One approach

focuses on creating new materials: researchers try to synthesize complex materials which have the desired properties. These materials have very complex crystal structures which present a low lattice thermal conductivity. The other approach focuses on creating nanostructured materials. By using simple materials through fabrication of nanostructures, it is easier to optimize thermoelectric properties. This study uses a nano-composite structure which is one remarkable method of nanostructured forms to control lattice thermal conductivity.

The research include heat measurement, theoretical simulation of phonon transport, and fabrication of composite nanostructures. All these studies aim at analysis of the nanostructure effect on thermal conduction. After optimization of the nanostructure, phonon transport control by nanostructures can be expected. Furthermore, it is also possible to create new technologies for improvement of materials and devices.

References

[1] T. C. Harman, P. J. Taylor, M. P. Walsh and B. E. LaForge, Science, 2002, 297, 2229. (2) R. Venkatasubramanian, E. Siivola, T. Colpitts and B. O'Quinn, Nature, 2001, 413, 597.

[2] A. I. Hochbaum, R. Chen, R. D. Delgado, W. Liang, E. C. Garnett, M. Najarian, A. Majumdar and P. Yang, Nature, 2008, 451, 163.

[3] A. I. Boukai, Y. Bunimovich, J. Tahir-Kheli, J.-K. Yu, W. A. Goddard Iii and J. R. Heath, Nature, 2008, 451, 168.

[4] B. Poudel, Q. Hao, Y. Ma, Y. Lan, A. Minnich, B. Yu, X. Yan, D. Wang, A. Muto, D. Vashaee, X. Chen, J. Liu, M. S. Dresselhaus, G. Chen and Z. Ren, Science, 2008, 320, 634.

[5] Y. Ma, Q. Hao, B. Poudel, Y. Lan, B. Yu, D. Wang, G. Chen and Z. Ren, Nano Lett., 2008, 8, 2580.

[6] X. W. Wang, H. Lee, Y. C. Lan, G. H. Zhu, G. Joshi, D. Z. Wang, J. Yang, A. J. Muto, M. Y. Tang, J. Klatsky, S. Song, M. S. Dresselhaus, G. Chen and Z. Ren, Appl. Phys. Lett., 2008, 93, 193121.

[7] G. Joshi, H. Lee, Y. Lan, X. Wang, G. Zhu, D. Wang, R. W. Gould, D. C. Cuff, M. Y. Tang, M. S. Dresselhaus, G. Chen and Z. Ren, Nano Lett., 2008, 8, 4670.

[8] M. I. Flik, B. I. Choi and K. E. Goodson, Trans. ASME, J. Heat Transf. 114, 667 (1992).

[9] Venkatasubramanian, R.; Siivola, E.; Colpitts, T.; O'Quinn, B. Thin-Film Thermoelectric Devices with High Room- Temperature Figures of Merit. Nature 2001, 413, 597–602.

[10] Hsu, K. F.; Loo, S.; Guo, F.; Chen, W.; Dyck, J. S.; Uher, C.; Hogan, T.;

Polychroniadis, E. K.; Kanatzidis, M. G. Cubic AgPbmSbTe2þm: Bulk Thermoelectric Materials with High Figure of Merit. Science 2004, 303, 818–821.

[11] Poudel, B.; Hao, Q.; Ma, Y.; Lan, Y.; Minnich, A.; Yu, B.; Yan, X.; Wang, D.; Muto, A.; Vashaee, D..; et al. High-Thermoelectric Performance of Nanostructured Bismuth Antimony Telluride Bulk Alloys. Science 2008, 320, 634–638.

[12] C. Dames and G. Chen, Thermoelectrics Handbook: Macro to Nano, Chapter 42, CRC Press, ed. D. Rowe (2005).

[13] Yuping He, Davide Donadio, Joo-Hyoung Lee, Jeffrey C. Grossman, and Giulia Galli. Thermal Transport in Nanoporous Silicon: Interplay between Disorder at Mesoscopic and Atomic Scales ACS Nano 2011, VOL. 5, NO. 3, 1839-1844.

[14] Xinyu Wang, Kevin D. Parrish, Jonathan A. Malen & Paddy K. L. Chan Modifying the thermal conductivity of small molecule organic semiconductor thin films with metal nanoparticles Scientific Reports 5, Article number: 16095 (2015).

[15] Jin, Y., Nola, S., Pipe, K. P. & Shtein, M. Improving thermoelectric efficiency in organic-metal nanocomposites via extra-low thermal boundary conductance. J. Appl. Phys. 114, 194303 (2013).

[16] Mutsunori Uenuma, Chao He, Ichiro Yamashita and Yukiharu Uraoka, Improved Thermoelectric Properties Using Protein Assisted Nanostructure, ICOT 2016, Kyoto, Japan

[17] M. I. Flik, B. I. Choi and K. E. Goodson, Trans. ASME, J. Heat Transf. 114, 667 (1992).

[18] C. L. Tien and G. Chen, Trans. ASME, J. Heat Transf. 116, 799 (1994).

[19] F. Yang and C. Dames, Phys. Rev. B 87, 035437 (2013).

[20] D. G. Cahill and R. O. Pohl, Solid State Commun. 70, 927 (1989).

[21] Jason M. Larkin and Alan J. H. McGaughey, Physical Review B 89, 144303 (2014).

[22] Martin Maldovan, Nature Materials, Vol 14, July 2015.

[23] S. Kumagai, S. Yoshii, N. Matsukawa, K. Nishio, R. Tsukamoto, and I. Yamashita, "Self-aligned placement of biologically synthesized Coulomb islands within nanogap electrodes for single electron transistor," Applied Physics Letters, vol. 94, Feb 23 2009.

[24] M. Uenuma, T. Ban, N. Okamoto, B. Zheng, Y. Kakihara, M. Horita, et al., "Memristive nanoparticles formed using a biotemplate," Rsc Advances, vol. 3, pp. 18044-18048, 2013.

[25] M. Uenuma, B. Zheng, K. Kawano, M. Horita, Y. Ishikawa, I. Yamashita, et al., "Guided filament formation in NiO-resistive random access memory by embedding gold nanoparticles," Applied Physics Letters, vol. 100, Feb 20 2012.

[26] I. Inoue, K. Watanabe, H. Yamauchi, Y. Ishikawa, H. Yasueda, Y. Uraoka, et al., "Biological Construction of Single-Walled Carbon Nanotube Electron Transfer Pathways in Dye-Sensitized Solar Cells," Chemsuschem, vol. 7, pp. 2805-2810, Oct 2014.

[27] M. Ito, N. Okamoto, R. Abe, H. Kojima, R. Matsubara, I. Yamashita, et al., "Enhancement of thermoelectric properties of carbon nanotube composites by inserting biomolecules at nanotube junctions," Applied Physics Express, vol. 7, p. 065102, 2014.

[28] 山下一郎 , バイオと無機材料の融合による新しいナノプロセス バイオナノプロ セスとウエットテクノロジー .

[29] I. Yamashita, "Fabrication of a two-dimensional array of nano-particles using ferritin molecule," Thin Solid Films, vol. 393, pp. 12-18, Aug 1 2001.

● Chapter 2

2 Control for Separated Distribution of Nanoparticles

2.1 Introduction

Nanoparticles (NPs) have recently attracted great interest because of their potential to be used as components in nanotechnology. Therefore, many methods to produce NPs have been studied. Physical methods include grinding materials, laser abrasion, and ion injection. Chemical methods include the sol−gel method and the trioctylphosphine oxide (TOPO) method. Using a nanometric cavity for synthesizing NP is another method[1]. This method has been known as Bio Nano Process. In this method, apoferritin is used as a cage to transport metal complex NPs. There are many applications for these NPs such as solar device or memory, which need to distribute NPs array on a solid surface. In this situation, NPs and their separation distances (SD) play important roles in producing functional nano-composite structures. To achieve controlled structure in nanoscale, BNP was proposed to be used[2]. As an important part of BNP, ferritin protein molecule consists of 24 polypeptide subunits. The ferritin protein shell with inner and outer diameters of 7 nm and 12 nm, respectively. Its outer face can be modified to change conditions of adsorption[3, 4](Fig. 2.1). The process has been developed to make two dimensional array of ferritin with NP on a SiO_2 surface, which produces independent NP array after protein shell elimination. By using the apoferritin cavity, a lot of homogeneous NPs have previously been synthesized[5−11]. The interaction between ferritin and substrate surfaces has been identified as significant research[12−15] along with more general

considerations concerned with NP adsorption[16]. Numerous NP nanostructures have been fabricated utilizing ferritins[17–27]. Although the process was intensively studied[28, 29], detailed analyses are not sufficient. Moreover, new analysis methods should be developed. Many conditions affect the ferritin adsorption density. PEGylated ferritin (ferritin modified by polyethylene glycol) with different length of PEG and different concentrations of ammonium acetate solution was used to analyze the relationship between adsorption and effective conditions in detail. After that, nano-composite structure can be fabricated further.

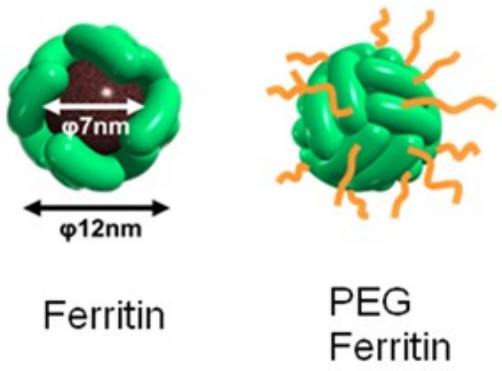

Figure 2.1 Schematic figure of ferritin protein with iron core and PEGylated ferritin.

2.2 Preparation of PEG-ferritin

2.2.1 Synthesis procedure

At first, preparation and purification of Fer8 which is a new type of ferritin are necessary. The Fer0 which is a basic type of ferritin consist of all L-type ferritin sub-unites. And Fer8 is the ferritin wherein 8 amino acid residues are removed from N-terminal of Fer0 (Fig. 2.2). Because of this change, Fer8

surface is negatively charged, giving less steric hindrance to makes it easier to modify the ferritin surface. Finally, the protein concentration determination will be done by Lowry method.

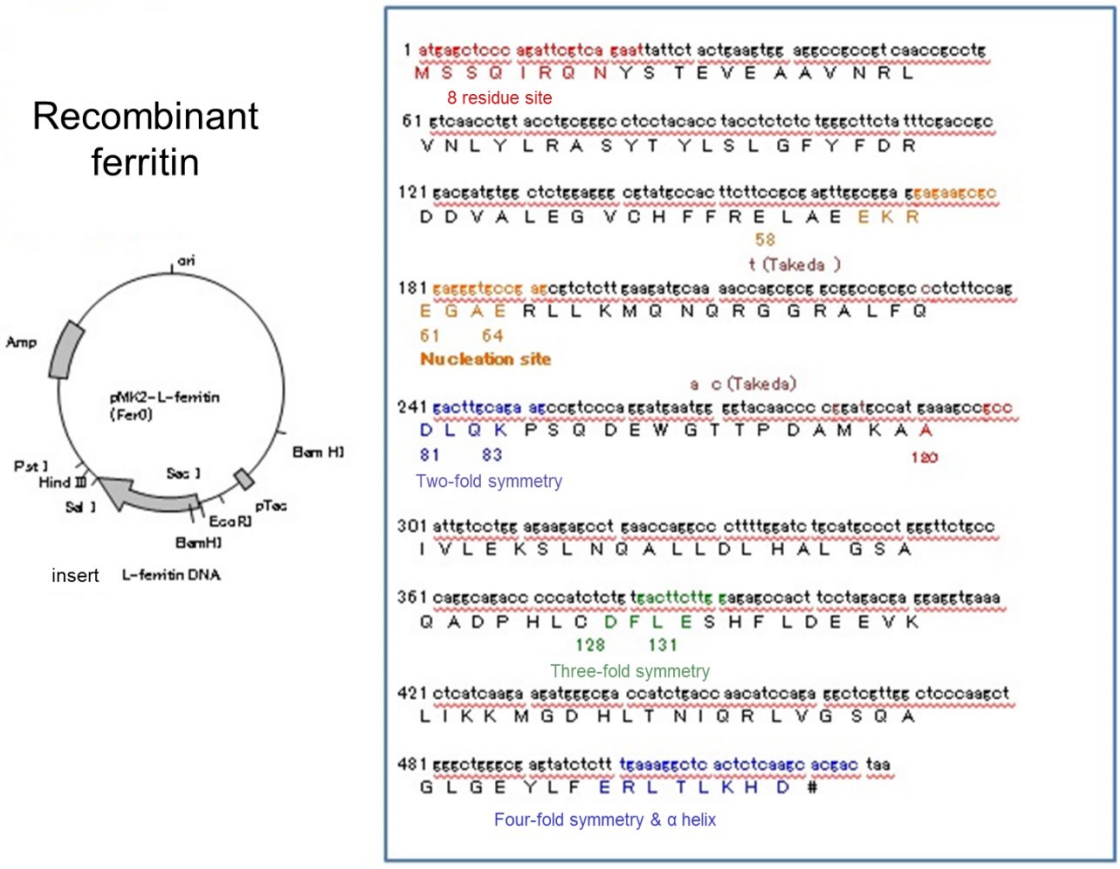

Figure 2.2 Base sequence of Fer0 and Fer8[30].

Then, the lysine residues on the surface of ferritin were reacted with PEG succinimide ester (NHS-PEG-OMe). The detail of experimental protocol is described below:

I. Weigh designed amount of NHS-PEG-OMe, which was bought from

outside, per subunit of ferritin in a falcon tube.

II. The powder described above was dissolved in 5.0 mL of 100 mM potassium phosphate buffer (pH = 8.2), and was filtrated by 0.20 μm membrane filter (ADVANTEC, DISMIC-25CS).

III. Fer8 (1.0 mg) with an iron core dissolved in 100mM phosphate buffer (pH = 8.2) was mixed with the PEG derivative solution in step 2. Adjust the final concentration of ferritin to 0.2 mg/mL.

IV. At 4°C, the reaction solution from step 3 was kept in a dark place for 60 hours.

After completion of the reaction (Figure 2.3), the solution was transferred to a dialysis tube and dialyzed three times by 100 mM solution (pH = 7.0) of HEPES-NaOH in order to remove PEG in solution. Then the concentration of protein was confirmed by Bradford protein assay.

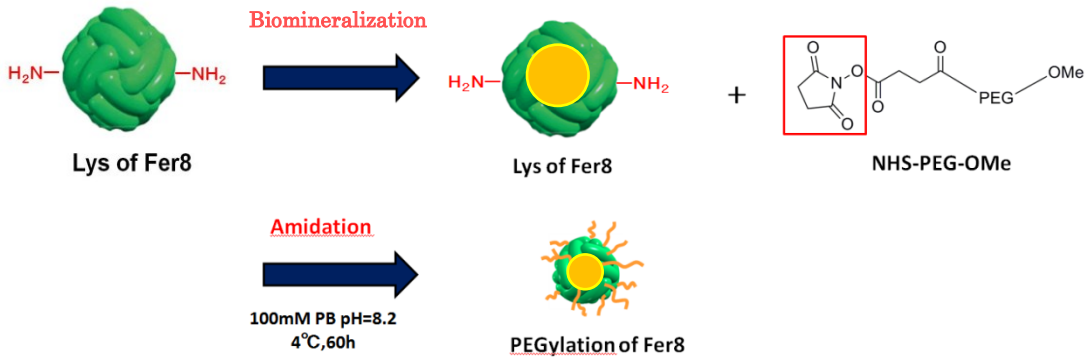

Figure 2.3 Process of modification on ferritin surface.

2.2.2 Characterization of PEG-ferritin

In order to research the mechanism of adsorption of PEG-ferritin to the substrate, the PEG-ferritins were characterized by some spectroscopic methods and calculation. Debye length of PEG-ferritin in solution can be calculated, but the real length of PEG layer on ferritin in solution still needs to be measured. Furthermore, the basic issues like proving the modification on ferritin must be confirmed at first. Thus dynamic light scattering (DLS) measurement and matrix assisted laser desorption ionization time-of-flight mass spectrometry (MALDI-TOF/MS) measurement were done.

From the result of MALDI-TOF/MS analysis (Figure 2.4), attachment of PEG on the Fer8 (Fe) is confirmed and that 2-3 PEGs are attached per ferritin subunit. That means almost 48-72 PEGs are attached per ferritin. In addition, this density is thought to make an interaction between each ferritin when adsorption occurs. Otherwise, the DLS measurement results shown in Table 2.1 indicate the real diameters of PEG-ferritin in solution. In other words, the PEG layer on ferritin interacts with each other strong in those distances. These data will be inputted into a simulation as the rigid balls' diameters.

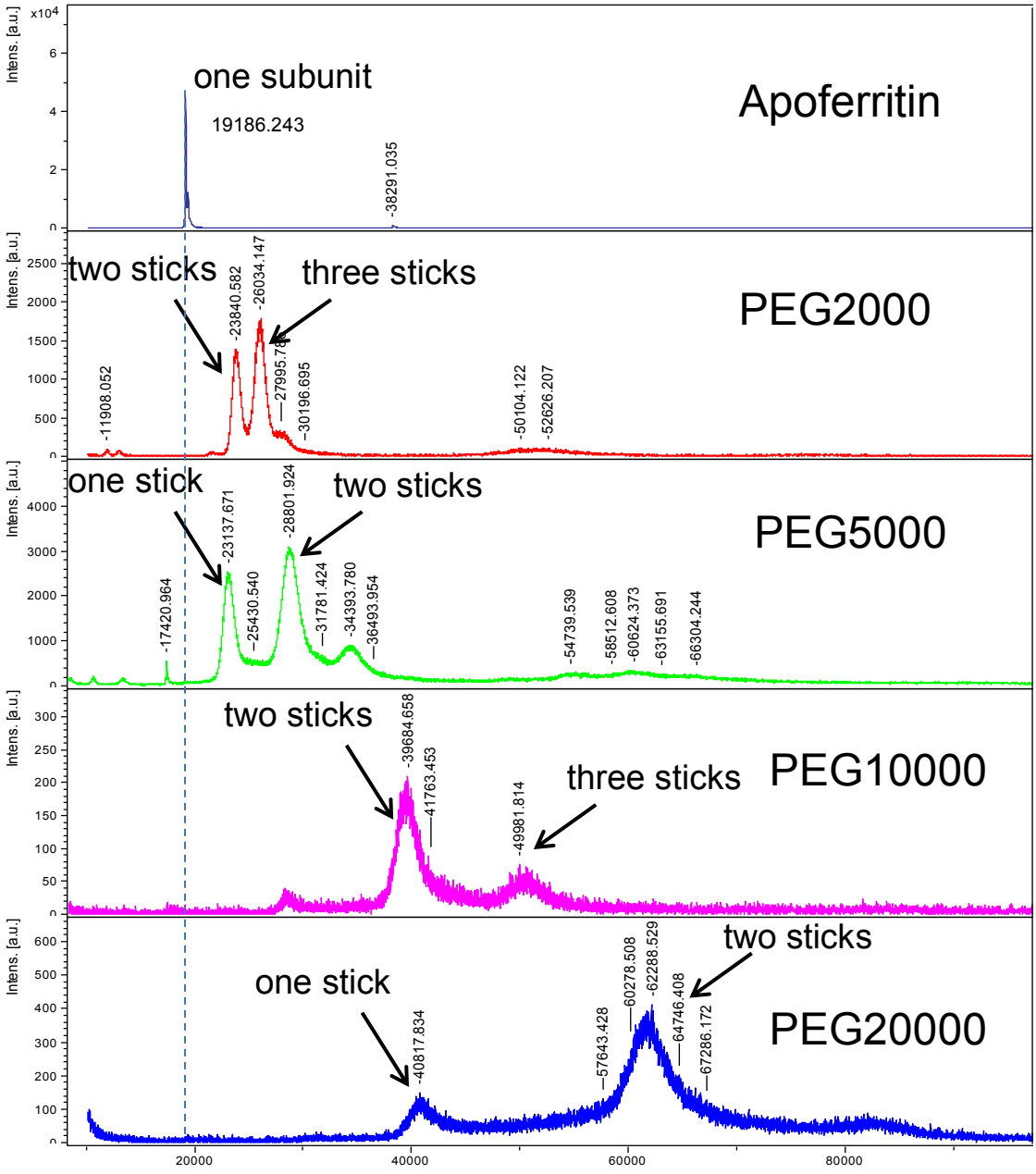

Figure 2.4 Results for analysis of apoferritin, PEG2000, 5000, 10000, 20000-ferritin by matrix assisted laser desorption ionization time-of-flight mass spectrometry (MALDI-TOF/MS).

Table 2.1 Dynamic light scattering (DLS) measurement results for apoferritin, PEG2000, 5000, 10000, 20000-ferritin. Measurement conditions in protein density of 0.2 mg/ml and NaCl solution concentration of 10 mM.

PEG	w/o	2000	5000	10000	20000
Diameter	12.7 nm	17.0 nm	24.6 nm	35.8 nm	45.2 nm
PEG-length		2.2 nm	6.0 nm	11.6 nm	16.3 nm
Zeta potential	-12.8 V	-7.9 V	-4.8 V		

2.3 Control of Separated Distance of Nanoparticles by Ion Strength

There are many methods to control SD of NPs. For example, making adjustment of protein concentration is most simple way to control the density of adsorption on substrate, in other words, control SD of NPs. Changing ion strength in solution or chemical modification of ferritin both focus on

protein-protein interaction directly. Of course, the conditions of experimental process also have effects on SD control. Among all methods, just choosing one may not work well. Therefore, optimization of methods will be discussed in this research. But first of all, PEG-ferritin as one of important implements in this experiment should be introduced.

2.3.1 Introduction

NP and their SD play important roles in functional nano-composite material which has low thermal conductivity. As stated before, the process to make two dimensional array of ferritin with NP on a SiO_2 surface, which produces independent NP array after protein shell elimination has been developed. In order to control the materials' properties by nano-composite structures, novel methods which can control the density and separation distances of ferritins in nano-scale is needed. There are many conditions affect the ferritin adsorption density. PEG2000-ferritin (ferritin modified by polyethylene glycol) was used in different concentration of ammonium acetate solution to analyze the relationship between adsorption condition and ammonium acetate (AA) concentration in detail.

2.3.2 Experiment

PEG2000 was used for modification of L-ferritin (Fer8) to synthesize an iron-oxide core inside the ferritin (Figure 2.5). Then, 1×1 cm Si substrate

with 3 nm thick thermal oxide layer were cleaned with acetone, methanol, and then with pure water. After the cleaning process, the substrate was treated by UV-Ozone for 10 min at 115^{o}C in order to make a hydrophilic surface. Then, the substrate was put into pure water for storage before the next step of the experiment. After performing a spin dry process, the PEG2000-ferritin (0.05 mg/ml) with Fe core at the ammonium acetate concentration of 1 mM - 10 mM were dropped on the sample (50 μL) and held for 5 min. Then, the solution was removed through spin-coating. The experiment conditions for spin-coating have been optimized. In order to a make uniform distribution of ferritin, spin-coating conditions are fixed at 360 rpm, 60 sec; 1000 rpm, 60 sec; 5000 rpm, 30 sec. Finally, the NPs on the samples were observed using SEM.

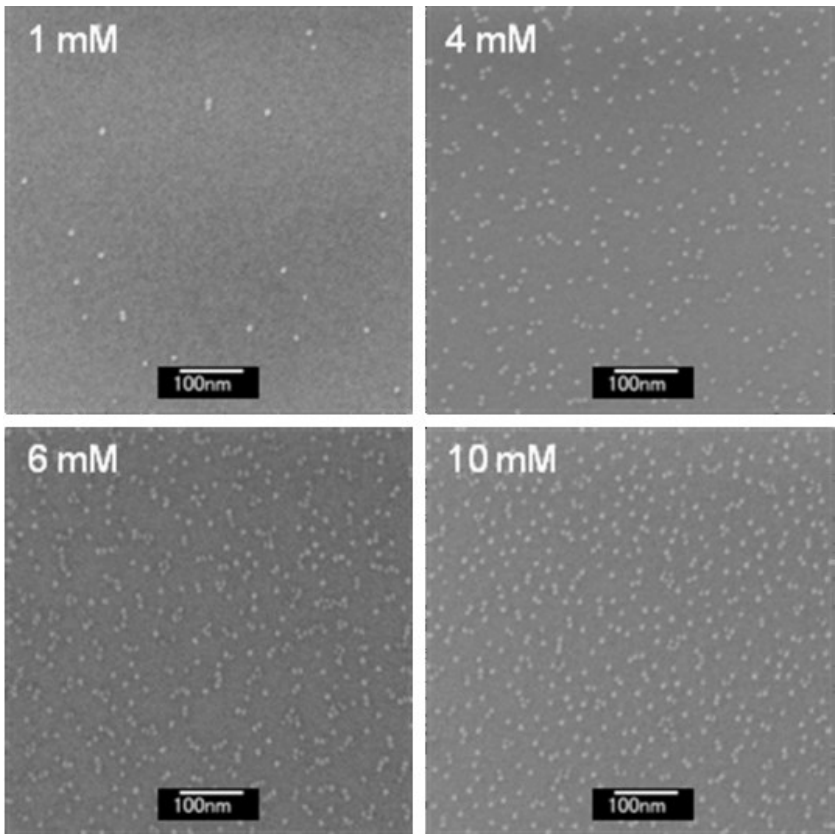

Figure 2.5 SEM images of NPs on SiO_2 surface with ammonium acetate concentration in 1, 4, 6 and 10 mM.

2.3.3 Result and Discussion

Through analysis of the SDs of PEG2000-ferritin on SiO_2 using SEM images (Figure 2.5), the four shortest distances were chosen from distances which were calculated from one center point of NP to other points. Figure 2.6 shows histograms of obtained SD distribution with different concentration of AA. There were two peaks. One peak around 10 nm which comes from aggregation of ferritin molecules, in which all the ferritin molecules contact each other and no spaces. The ferritin aggregation would be caused by the damage of PEG modification on ferritin. The other peak is a longer distance peak which comes from dispersed ferritins owing to the PEG chains. The peak of maximum probability SD (d_m) and FWHM of the distribution was calculated from these histograms. As shown in Figure 2.7, the concentrations of 1, 4, 6 and 10 mM correspond to around 100, 34.4, 26.6 and 26.4 nm, respectively. Through this, it can be clearly seen that the SD of NP decreased and FWHM was narrowed by increasing AA concentration. As observed, the SD (d_m) value or FWHM both have stronger gradient in the area of AA concentration below 4 mM. This result can be explained by using the Debye length (λ). The Debye length is explained approximately as $\lambda \propto I^{-1/2}$ where I is ion strength. Through figure 2.8, the SD (d_m) and Debye length

have a linear relationsip with AA concentration below 4 mM but deviates beyond 6 mM. That means the interaction between ferritins for distribution on substrate is determined by Debye length in AA concentration below 4 mM. In the area of AA concentration beyond 6 mM, Debye length approached the PEG length. Therefore, the effect of PEG and Debye length are both possible effects on adsorption of ferritin. As a result, the AA concentration higher than 6 mM was found to be the optimized condition for controlling the SD with PEG2000-ferritin molecules.

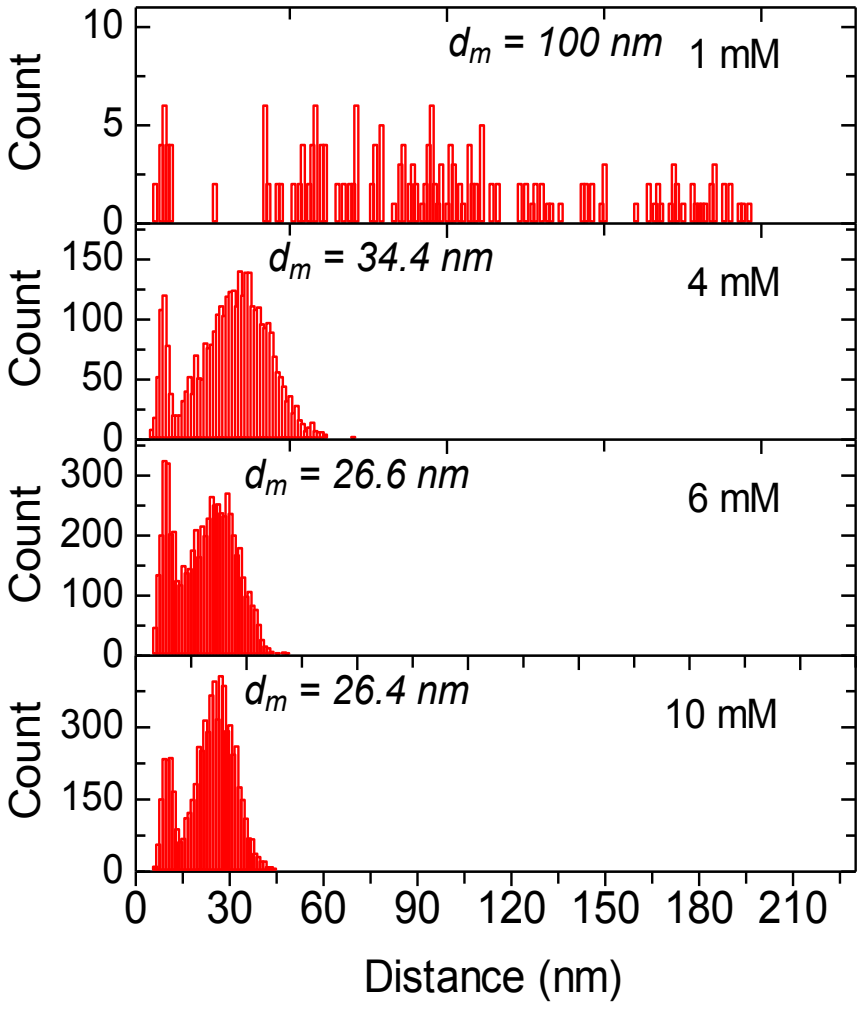

Figure 2.6 Histograms of SDs distribution with the AA concentrations of 1, 4, 6 and 10 mM.

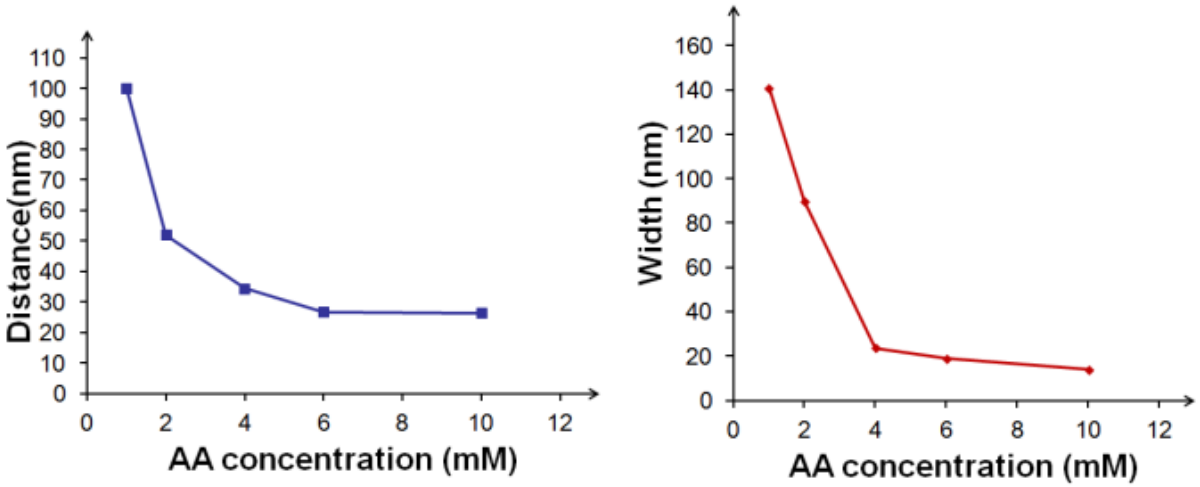

(a) (b)

Figure 2.7 (a) SD mean value dependence with AA concentration. (b) FWHM dependence of AA concentration.

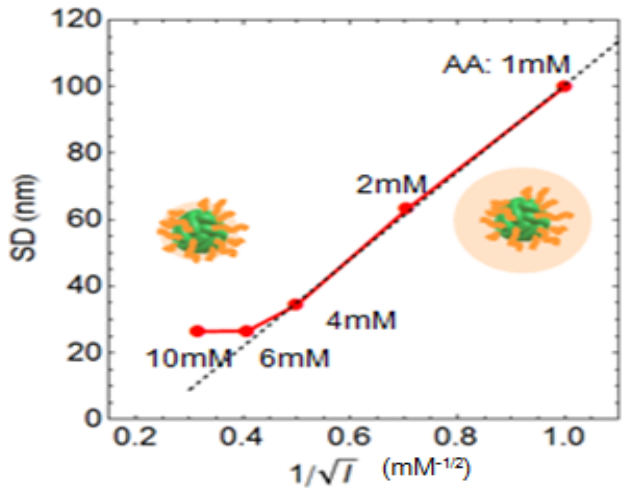

Figure 2.8 Debye lengths in different concentration of ammonium acetate.

2.3.4 Conclusion

PEG2000-ferritn with Fe core was analyzed to control SD of NPs on the

SiO_2/Si substrate in detail. From the analysis of results, the SD and FWHM decreased with increasing AA concentration. Although in the low AA concentration area, according to the reason that Debye length is longer than PEG length, the SD increased quickly. However, in high concentration area, the PEG length is longer than the calculated Debye length. Therefore, SD without apparent change is possible.

2.4 Separated Distances Control by PEG Length

2.4.1 PEG-ferritin on Si

Because the SD of NPs is distributed in a large range, changing AA concentration to control SD is not enough. In order to control SD, a novel method should be established based on the analyses. PEG-ferritin was used to analyze the relationship between adsorption condition and length of PEG.

Experiment and Result

At first, Si substrates with 3 nm thick thermal oxide layer were cleaned by acetone and methanol and then cleaned by pure water. After cleaning process, the samples were treated by UV-Ozone for 10 min at 115^{o}C. Then the samples were put into pure water for storage before the next step of the experiment. After performing a spin dry process, the PEG2000, 5000, 10000, 20000-ferritin (0.05 mg/ml) with Fe core at an AA concentration of 10 mM

were dropped on the samples and held for 3 min. Then, the solution was removed through spin-coating (500 rpm in 2s and 3000 rpm in 30s). Finally, the NPs on the samples were observed using scanning electron microscope (SEM) (Figure 2.9). In order to analyze the NPs SD distribution, the radial distribution function (RDF) was used to evaluate SD. With this function, every distance between two NPs was calculated and the number of NPs in this area of distance was counted. Then, the distribution figure is shown in Figure 2.10. As observed, the SDs' peak shift to the right side along with increasing length of PEG in principle.

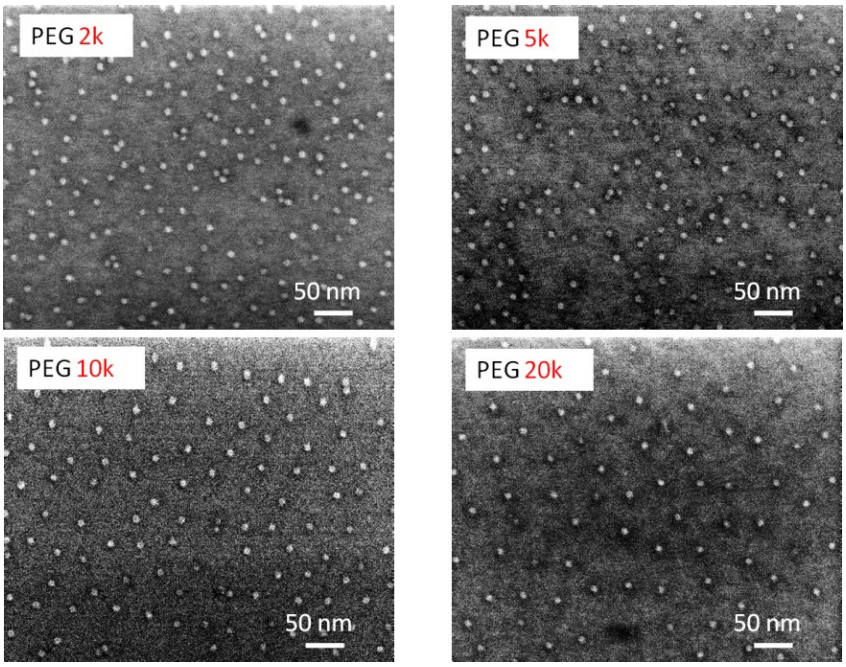

Figure 2.9 Scanning electron microscope (SEM) images of PEGylated with PEG2000, 5000, 10000, 20000-ferritin contented iron core separated distribution (AA concentration is 10 mM).

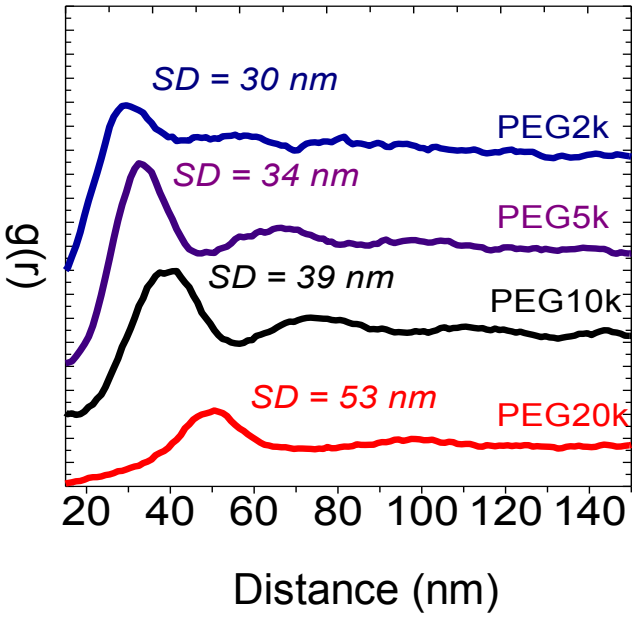

Figure 2.10 Radial distribution function by SEM analysis.

Simulation Result and Discussion

For supporting the hypothesis that the distribution of PEG-ferritin depends on interaction of PEG layer when ion strength is higher than 4 mM, the simulation for adsorption of ferritin and PEG-ferritin was done. The simulation was set with the presupposition as follows (Figure 2.11):

1. All the same type ferritins are set as rigid ball with diameter of DLS data.
2. The simulation is started with the adsorption density designed and certain distribution images (800 nm×600 nm).
3. The random irradiation incident angle and place for one time.
4. One rigid ball is irradiated for one time.

5. Once the rigid ball contacted substrate, it is fixed.
6. If the rigid ball contact the other ball on the substrate, it reflects.

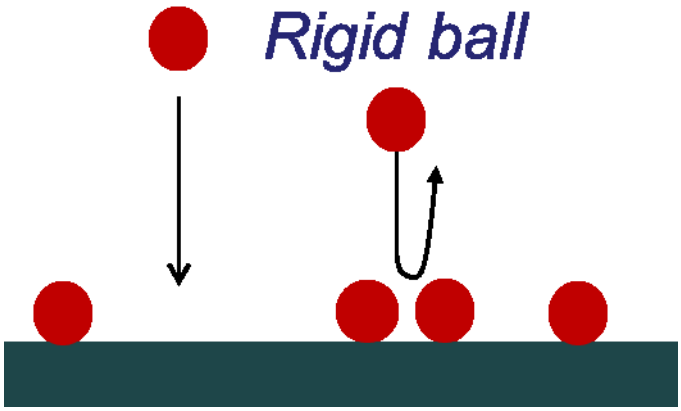

Figure 2.11 Schematic figure of simulation for PEG-ferritin adsorption.

Through this simulation, the ferritins' absorption was simulated. The images of the simulation results (Figure 2.12) were analyzed with the RDF method. Then, the simulation results of PEG5000, 10000, 20000-ferritin fitting the experimental results have been confirmed. Obviously, the simulation results of ferritin and PEG2000-ferritin were slightly smaller than experimental ones (Figure 2.13). From the calculation of Debye length, it was known that the Debye length of ferritin is longer than PEG2000 length but shorter than PEG5000 in 10 mM solution[4]. Therefore, the SD PEG2000-ferritin and PEG5000, 10000, 20000- ferritin are determined by different mechanisms. For PEG2000, distribution is determined by ion strength which decide Debye length. For PEG5000, 10000, 20000- ferritin, distribution should be affected by interaction of PEG layer, which can be explained by that PEG layer's interaction which has a longer work distance than Debye length.

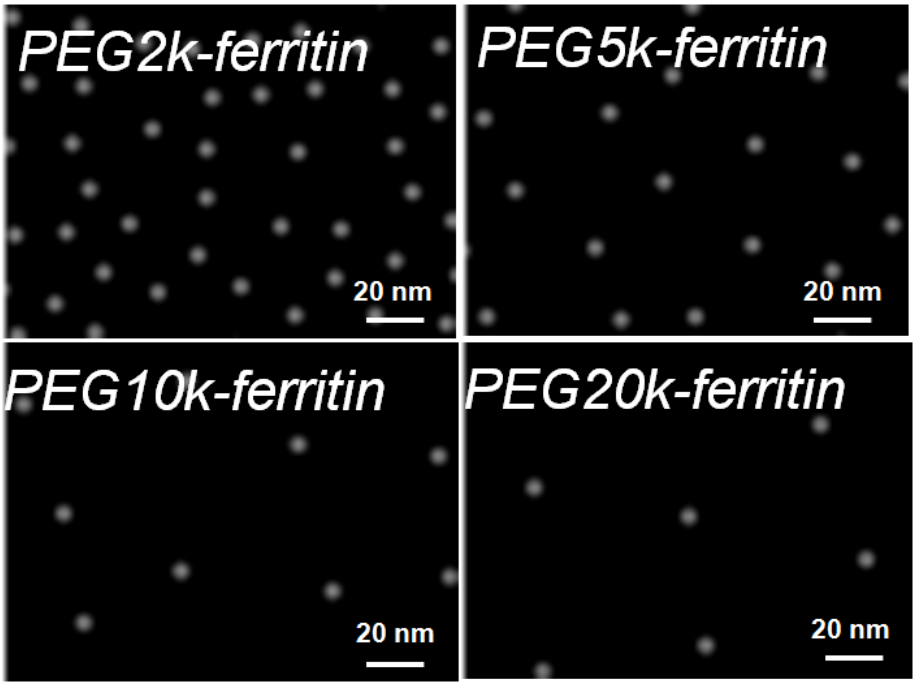

Figure 2.12 Simulation results separated distribution of ferritin PEGylated with 2000, 5000, 10000, 20000 which are considered as rigid ball[31].

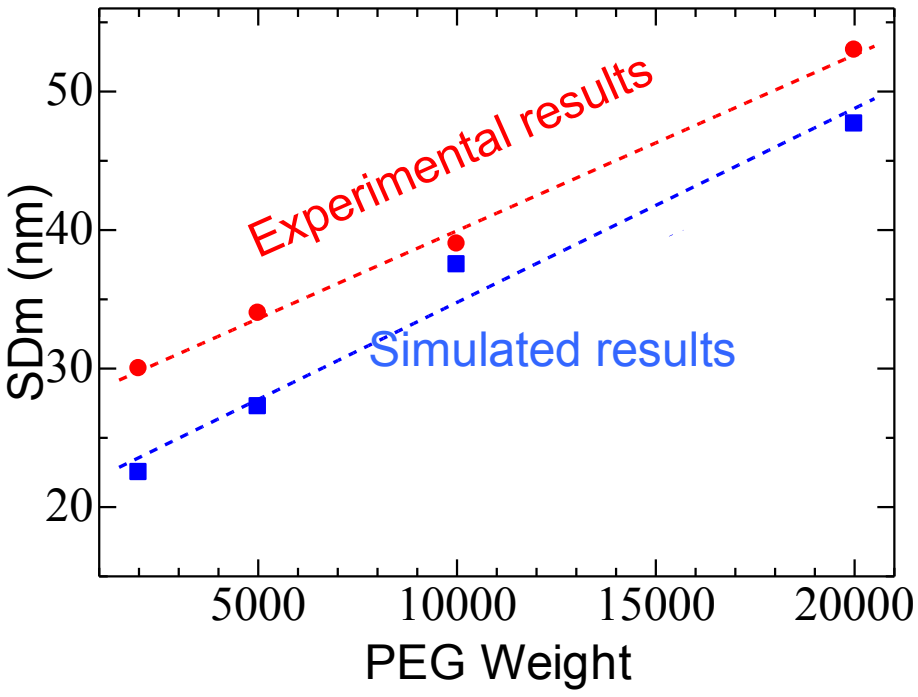

Figure 2.13 Simulation results and experiment results.

Discussion

From the results of PEG-ferritin evaluation, the PEG-ferritin is thought to make an interaction with each other when adsorption occurs. Based on these conditions, PEG2000, PEG5000, PEG10000 and PEG20000 were used to PEGylation of ferritin. The result was obtained (Figure 2.9) and for analysis, the RDF is introduced. Through the calculation of all the distances between ferritin central points, the distribution of NPs was analyzed by RDF (Figure 2.10). The first peak on the left is the most probably the distance of NPs. Furthermore, there is almost no value on the left side of the peak. Thus, if this peak value is controllable, the NPs separation distance is most likely under control.

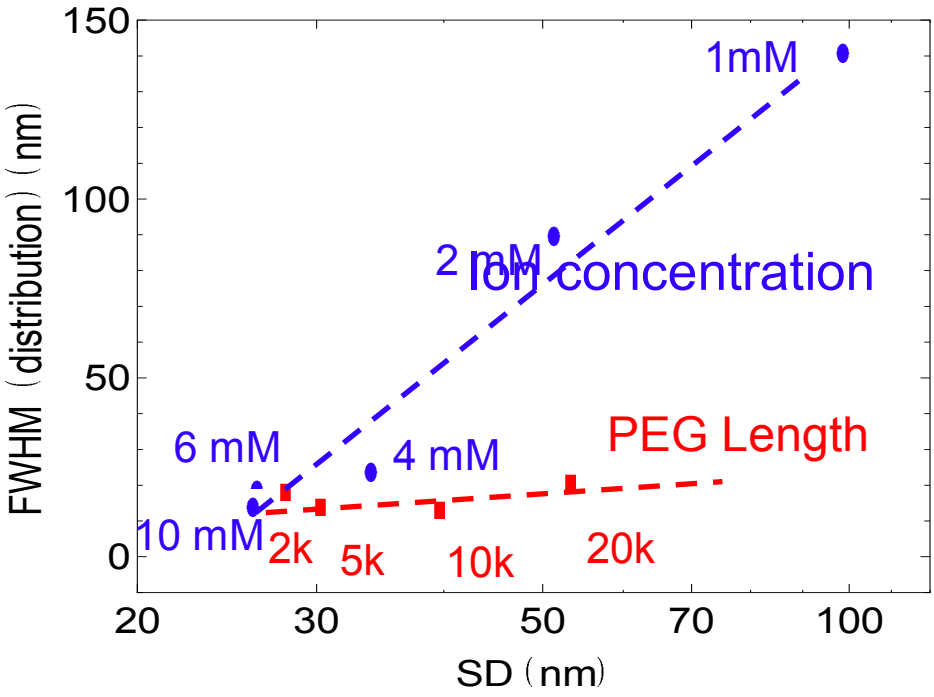

Figure 2.14 Full width at half maximum (FWHM) of distribution as functions of concentration of ammonium acetate and PEG length.

It was considered that all the ferritins should not attach to the substrate at the same time. Some NPs attach first and become fixed while the others attach to the substrate later and finish the distribution though the interaction with fixed NPs. To prove this idea, a comparison between experimental result and simulations was done. According to the result of the FWHM distribution, it was considered that the adsorption density increases along with increasing ion strength. But, the ion strength decides the separation distance roughly because of the wide distribution of SD (Figure 2.14). At the solution condition of 10 mM concentration, the Debye length is shorter than 3 nm. Compare it with the PEG effective length (Table 2.1), the Debye length

is slightly shorter than the length of PEG2000 in solution. So maybe, the electrostatic force in Debye length is the main interaction of PEG2000-ferritin. Although this interaction works at a long distance, it is not strong enough to control the separation distance precisely in a narrow SD region. Thus, a more accurate method is necessary. If longer PEG is used in the same solution concentration, the interaction of PEG layer should determine the separation distance of ferritins. It is also considered as a good solution for the problem of rough distribution.

2.4.2 PEG-ferritin on Different Materials (Ta, Pt, Cr, Bi_2Te_3, TiN)

The density and SD of NPs changed along with a change of materials of the substrate surface. With the consideration of Zeta potential (Table 2.1) or hydrophilicity, the different surface materials lead to a Zeta potential change. Particularly, the SD of NPs distribute in random and the density decreases significantly (Figure 2.15, 2.16). When films of Ta, Ni and Bi_2Te_3 were deposited on the substrates, the adsorption almost did not happen and NPs were rarely seen on the center of substrate. For improvement of absorption, the experimental conditions were optimized. Some particular spin coater rotation speeds were found to very efficiently improve the adsorption. In the experiment, at first, the spin-coating condition was changed at different speed conditions (360 rpm in 30 s, 1000 rpm in 60 s and 5000 rpm in 30 s) after incubation. Then through comparison experiment, it was known that the speed at 1000 rpm was important for adsorption. Through the

optimization of spin coater condition, the NPs distribution was improved significantly. The reason for this phenomenon is still being discussed.

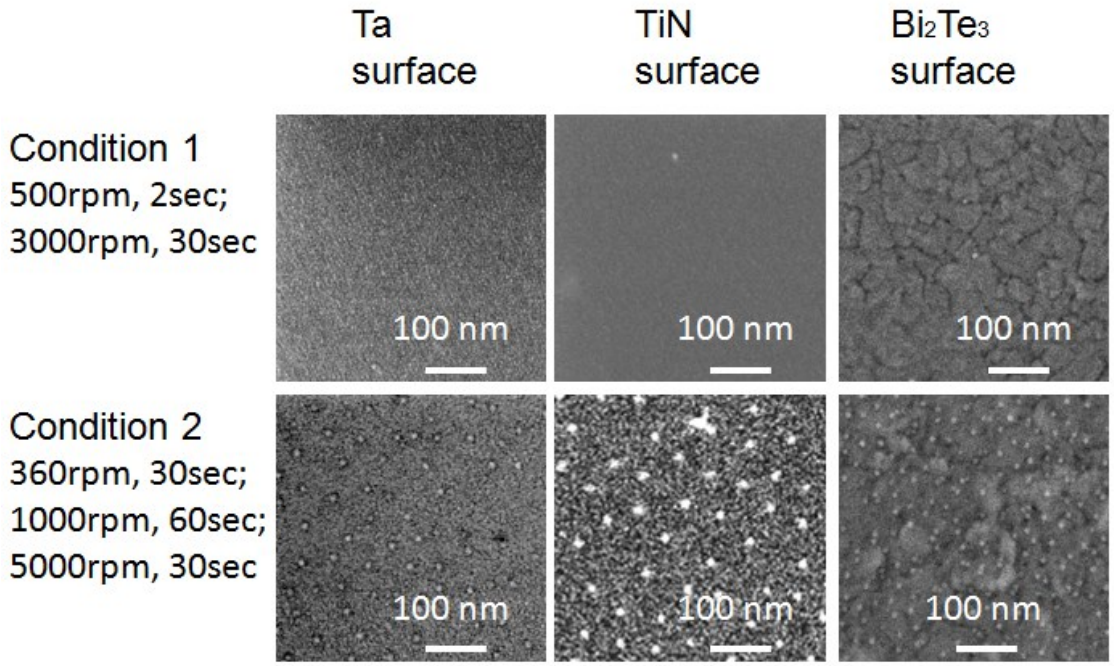

Figure 2.15 Images of PEG10000-ferritin distributed on Ta, TiN and Bi_2Te_3 films at two spin-coater's conditions.

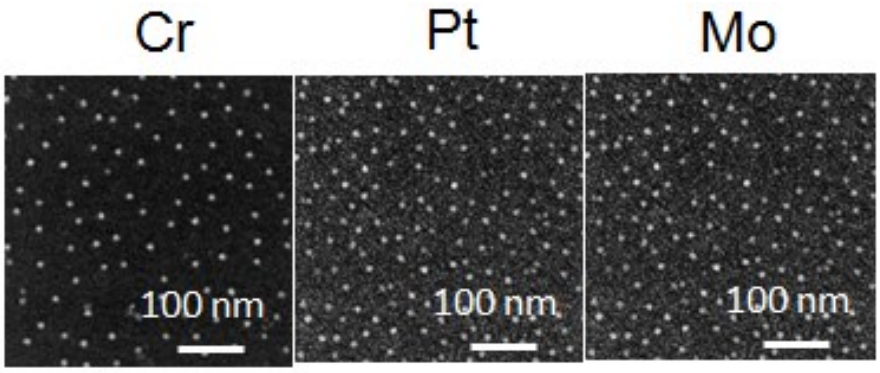

Figure 2.16 Images of PEG10000-ferritin distributed on Cr, Pt and Mo films at spin-coater's condition 2.

2.5 Conclusion

Controllable array of iron nanoparticle was successfully fabricated on SiO_2 and metal surface using PEG ferritins with different molecular weights. This study was able to successfully find a better method for a controllably spaced ferritin array with SD shorter than 100 nm. This study also discussed a method utilizing electrostatic repulsion force and the mechanism of this phenomenon. Because of PEGylation, electrostatic repulsion forces of ferritin against the SiO_2 surface were also reduced. By selecting the modified length of PEG, the NPs distribution can be controlled. With this procedure, much narrower separation distribution can be achieved. The NPs distribution of PEGylated ferritins can be controlled by adjusting the molecular weight of PEG with a proper ionic strength of the solution in order to avoid aggregation. Furthermore, through the simulation, the mechanism of PEG-ferritin distribution was proposed. In addition, the exact control of NPs distribution is believed to be very useful for not only thermoelectric nano-composite materials but also devices fabrication with other properties.

References

[1] Iwahori, K.; Yoshizawa, K.; Muraoka, M.; Yamashita, I. Inorg. Chem.2005, 44, 6393.

[2] I. Yamashita, Thin Solid Film. 393, 12 (2001).

[3] Harrison, P. M.; Andrews, S. C.; Artymuik, P. J.; Ford, G. C.; Guest, J. R.; Hirzmann, J.; Lawson, D. M.; Livingstone, J. C.; Smith, J.M. A.; Treffry, A.; Yewdall, S. J. Probing structure-function relation in ferritin and bacterioferritin. Adv. Inorg. Chem. 1991, 36, 449−486.

[4] Chao He, Mutsunori Uenuma, Naofumi Okamoto, Hiroki Kamitake, Yasuaki Ishikawa, Ichiro Yamashita and Yukiharu Uraoka, A distance-controlled nanoparticle array using PEGylated ferritin, Materials Research Express 1 (2014) 045410.

[5] Wong, K. K. W.; Mann, S. Biomimetic synthesis of cadmium sulfide-Ferritin nanocomposites. Adv. Mater. 1996, 8, 928−932.

[6] Douglas, T.; Stark, V. T. Nanophase cobalt oxyhydroxide mineral synthesized within the protein cage of Ferritin. Inorg. Chem. 2000, 39, 1828−1830.

[7] Yamashita, I.; Hayashi, J.; Hara, M. Bio-template synthesis of uniform CdSe nanoparticles using cage-shaped protein, apoferritin. Chem. Lett. 2004, 33, 1158−1159.

[8] Iwahori, K.; Yoshizawa, K.; Muraoka, M.; Yamashita, I. Fabrication of ZnSe nanoparticles in the apoferritin cavity by designing a slow chemical reaction system. Inorg. Chem. 2005, 44, 6393−6400.

[9] Iwahori, K.; Yamashita, I. Biological path of nanoparticles synthesis. In Dekker Encyclopedia of Nanoscience and nanotechnology; Lyshevski, Sergey Edward, Ed; Taylor and Francis: Oxford, 2006; pp 1−8, DOI: 10.1081/E-ENN2-120042184.

[10] Naito, M.; Iwahori, K.; Miura, A.; Yamane, M.; Yamashita, I. Circularly polarized

luminescent CdS quantum eots prepared in a protein nanocage. Angew. Chem., Int. Edt. 2010, 49, 7006−7009.

[11] Iwahori, K.; Takagi, R.; Kishimoto, N.; Yamashita, I. A size controlled synthesis of CuS nano-particles in the protein cage, apoferritin. Mater. Lett. 2011, 65, 3245−3247.

[12] Feder, J.; Giaever, I. Adsorption of ferritin. J. Colloid Interface Sci. 1980, 78, 144−154.

[13] Nygren, H. Nonlinear kinetics of ferritin adsorption. Biophys. J. 1993, 65, 1508−1512.

[14] Höök, F.; Rodahl, M.; Brzezinski, P.; Kasemo, B. Measurements using the quartz crystal microbalance technique of ferritin monolayers on methyl-thiolated gold: dependence of energy dissipation and saturation coverage on salt concentration. J. Colloid Interface Sci. 1998, 208, 63−67.

[15] Johnson, C.A.; Yuan, Y.; Lenhoff, A.M. Adsorbed layers of ferritin at solid and fluid interfaces studied by atomic force microscopy. J. Colloid Interface Sci. 2000, 223, 261−272.

[16] Adamczyk, Z. Particle adsorption and deposition: role of electrostatic interactions. Adv. Colloid Interface Sci. 2003, 100−02, 267−347.

[17] Kumagai, S.; Yoshii, S.; Yamada, K.; Matsukawa, N.; Fujiwara., T.; Iwahori, K.; Yamashita, I. Electrostatic placement of single ferritin molecules. Appl. Phys. Lett. 2006, 88, 153103.

[18] Yamashita, I. Fabrication of a Two-dimensional array of nanoparticles using ferritin. Thin Solid Films 2001, 393, 12−18.

[19] Yoshii, S.; Yamada, K.; Matsukawa, N.; Yamashita, I. Making monolayer of inorganic nanoparticles on silicon substrate. Jpn. J. Appl. Phys. 2005, 44, 1518−1523.

[20] Yamada, K.; Yoshii, S.; Kumagai, S.; Fujiwara, I.; Nishio, K.; Okuda, M.; Matsukawa, N.; Yamashita, I. High-density and highly surface selective adsorption of protein-nanoparticle complexes by controlling electrostatic interaction. Jpn. J. Appl. Phys. 2006, 45, 4259−4264.

[21] Sano, K.; Yoshii, S.; Yamashita, I.; Shiba, K. In Aqua Structuralization of a Three-dimensional configuration using biomolecules. Nano Lett. 2007, 7, 3200−3202.

[22] Ikezoe, Y.; Kumashiro, Y.; Tamada, K.; Matsui, T.; Yamashita, I.; Shiba, K.; Hara, M. Growth of giant two-eimensional crystal of protein molecules from a three-phase contact line. Langmuir 2008, 24, 12836−12841.

[23] Yamashita, I. Biosupramolecules for nano-devices: biomineralization of nanoparticles and their applications. J. Mater. Chem. 2008, 18, 3813−3820.

[24] Yamashita, I.; Iwahori, K.; Kumagai, S. Ferritin in the field of nanodevices. Biochim. Biophys. Acta 2010, 1800, 846−857.

[25] Meng, F.; Jiang, L.; Zheng, K.; Goh, C. F.; Lim, S.; Hng, H. H.; Ma, J.; Boey, F.; Chen, X. Protein-based memristive nanodevices. Small 2011, 7, 3016−3020.

[26] Watt, G. D.; Kim, J.-W.; Zhang, B.; Miller, T.; Harb, J. N.; Davis, R. C.; Choi, S. H. A Protein-based ferritin bio-nanobattery. J. Nanotechnol. 2012, 2012, 516309.

[27] Miura, A.; Hikono, T.; Matsumura, T.; Yano, H.; Hatayama, T.; Uraoka, Y.; Fuyuki, T.; Yoshii, S.; Yamashita, I. Floating nanodot gate memory devices based in biomineralized inorganic nanodot array as a storage node. Jpn. J. Appl .Phys. 2006, 45, L1−L3.

[28] R. Tsukamoto et al., The 58th Spring Meeting of JSAP, 2011, 25a-BV-19.

[29] R. Tsukamoto et al., The 72th Autumn Meeting of JSAP, 2011, 1p-V-4.

[30] R. Honda, Dr. Thesis, Graduate School of Materials Science, Nara Institute of

Science and Technology, Nara (2013).

[31] R. Matsuyama, Dr. Thesis, Graduate School of Materials Science, Nara Institute of Science and Technology, Nara (2013).

● Chapter 3

3 Sample's Preparation for 3ω Method and Evaluation

3.1 Measurement for Thermal Conductivity of Thin Film

Thermal conductivity measurement is a basic evaluation for materials. However, the thermal conductivity of some low dimensional nanostructures like thin film, nanowire, nanoparticle or nano-composited structure are difficult to evaluate as these have different properties from bulk materials. In all these issues, the thermal conductivity evaluation for thin film is widely useful for many fields such as microelectronics, photonics, thermoelectrics and so on. This is because the thermal loss exists while thermal flow occurs through the materials and this loss is very difficult to quantify. Also, this scale is also too tiny to accurately measure the temperature difference, and other properties. Therefore, direct measurement of thermal conductivity faces some problems in the accurate characterization of thin films. Nevertheless, there are some major methods to measure the thermal conductivity of thermoelectric materials.

The steady-state (absolute or comparative) method uses steady-state techniques to measure in a direct way. It means that the measurement is taken while the temperature of the material does not change with time. Constant signals make the signal analysis straightforward. In geology and geophysics, steady-state method is the most common method for consolidated rock samples which is the divided bar. There are various modifications to these devices depending on the temperature and pressure as well as sample size. A sample of unknown conductivity is placed between two brass plate, one is

hot brass plate at the top, the other is a cold brass plate at the bottom. Heat flux transfers downwards to the heat sink side. Measurements are taken after the sample has reached steady state which usually takes a period of time.

On the other hand, without steady-state, transient methods can measure in some limited conditions which are mentioned above. For instance, laser flash method, Time-Domain Thermoreflectance (TDTR) method, 3ω method, among others. These methods have their own advantages as well as inherent limitations. For example, the laser flash method is used to measure thermal diffusivity of specimen in the thickness direction. This method is based upon the measurement of the temperature rise at the rear face of the specimen produced by a short energy pulse on the front face. With a reference sample specific heat can be found and with known density, the thermal conductivity results can be calculated as follows: $k(T)=a(T)\cdot C_P(T)\cdot\rho(T)$ where k is the thermal conductivity of the sample, a is the thermal diffusivity of the sample, C_P is the specific heat of the sample, ρ is the density of the sample. It is available for various materials over a wide temperature range (−120 °C to 2800 °C). But as an indirect method, in the laser flash method, one should measure not only thermal diffusivity but also specific heat and density in order to calculate thermal conductivity. This will bring more error into the results. Furthermore, the thickness of the samples is a critical condition for this method. If the thickness is reduced to 100 nm level, the measurement will become almost impossible.

Otherwise, TDTR method can be applied most notably to thin film materials, which have properties that vary greatly when compared to the

same materials in bulk. The idea behind this technique is that once a material is heated up, the change in the reflectance of the surface can be utilized to derive the thermal properties. The change in reflectivity is measured with respect to time and the data received can be matched to a model which contain coefficients that correspond to thermal properties. However, this method is not suitable to measure anisotropic thin film, especially, in the in-plane direction measurement. In all these methods, 3ω method is the most accurate measurement for isotropic and anisotropic thin film and a system for 3ω method can be set up simply. Thus, this study focused on the 3ω method.

3.2 Theoretical model for 3ω Method

A widely implemented approach for measuring the cross-plane thermal conductivity in thin film is the 3ω method[1]. Although this method is intended to measure bulk materials due to excellent thermal characterization of thin films down to 20 nm thickness[1-9]. This method is well known as a thin film measurement of the cross-plane and in-plane thermal conductivity. The special feature of 3ω method is that the heater and sensor of the measurement system belong to the same part. And this part is realized by depositing the metal pattern (Figure 3.1) on the film sample. After that, a voltage signal is applied to this metal electrode pattern at a specific ω frequency at which the metal electrode is heated up. The relation between the metal electrode's temperature and the voltage frequency can be evaluated by this measurement.

Depending on this relation, the thermal conductivity can be derived. As a mechanism of 3ω method, at first, the thermal power's signal at 2ω frequency should be known by calculation via Ampere's law. Because of the dependence of temperature and electric resistance, the resistance increase should contain the 2ωfrequency part. After the changed electric resistance was multiplied by electric current at a frequency of ω, the voltage signal at 3ω frequency can be found. Depending on this signal, we can know the temperature of the electrode. The connections between temperature and thermal conductivity are evaluated by solving the simultaneous equations of thermal diffusion equation and electric power equation at frequency 3ω. Then, the relation between the temperature changes and change of frequency of electric signal can be derived as follow:

$$\Delta T(\omega) = \frac{P}{\pi \kappa_s} \int_0^{\infty} \frac{\sin^2(kb)}{\sqrt{(kb)^2 (k^2 + \frac{2i\omega}{D_{sub}})}} dk + \frac{P d_f}{2b\kappa_f} \quad (3\text{-}1).$$

Where P is electric current power, κ_s is thermal conductivity of substrate, κ_f is thermal conductivity of thin film, D_{sub} is thermal diffusivity of substrate, d_f is the thickness of thin film, $2b$ is width of metal line. This formula has two basic requirements, one is that the width of metal line must much smaller than the penetrated depth of thermal flow. That can be expressed as

$$b \ll \sqrt{\frac{D_{sub}}{2\omega}} \quad (3\text{-}2).$$

Another one is $\kappa_f < \kappa_s$ (3-3).

Normally, the formula is approximated into

$$dT = -\frac{P}{4l\pi\kappa} d(ln\omega) + \frac{P d_f}{2b\kappa_f} \quad (3\text{-}4).$$

If the two measurements are taken on the substrate and substrate with thin film, and the two results of measurements are calculated by formula (3-4), through the difference of two solutions, the thermal conductivity of thin film can be solved.

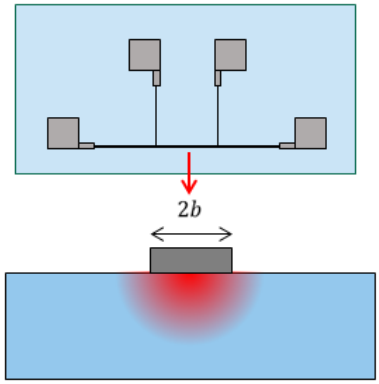

Figure 3.1 Schematic figure of measurement pattern of 3ω method.

3.3 Preparation of Sample

There are several steps for preparation of 3ω samples. Perhaps the different steps exist depending on different fabrication processes. The first common process is cleaning process for substrate. Because electrical conduction across interface between substrate and electrode are forbidden, so there is no need to remove insulator film of substrate and the substrates were cleaned with acetone, methanol and pure water and dried by N_2, finally, 5 minutes UV Ozone treatment. This simple cleaning process aim at removing organic impurities on substrate. After substrate cleaning, the pattern of electrode should be evaporated on substrate. There are two choices for this step, one is using the photolithography process including positive and negative methods;

the other one is evaporating the electrode pattern directly through metal mask. The different methods have different advantages and disadvantages. In this study, I try to use photolithography method as more smart method for changing conditions to confirm all necessary measurement conditions, at first. And then the metal mask was used to save process time and keep stability of process. In this study, positive photolithography method was employed to coat the photoresist on the substrates, then making the pattern by exposure of UV light on glass mask (Figure 3.2 a) and developing by photographic developer, the 3ω method pattern (Figure 3.2 b) where the photoresist was etched can be seen on the substrate. Next the metal such like aluminum was deposited by electron beam (EB) deposition equipment. Finally, by the acetone cleaning the photoresist was lifted off and the metal pattern was finished. For metal mask method, after cleaning processes, the electrode was evaporated on substrate directly.

In preparation for metal electrode pattern of 3ω method measurement, there are several conditions such as thickness of electrode or electrode material should be considered. Metal materials like Pt, Al and Au have been tried, for consideration of measurement and cost, finally, Al was chosen as material of 3ω electrode. In order to test the resistance of electrode, the thickness of Al electrode was varified from 100 nm to 400 nm. We found that 400 nm thickness led more excellent electric signals.

For reason of avoiding leak current, we always deposit SiO_2 thin film as an insulator film before electrode deposition in preparation processes of measurement. And this process also can make sample surface less rough, so

that more uniform electrode is expected, furthermore, less error in this 3ω measurement.

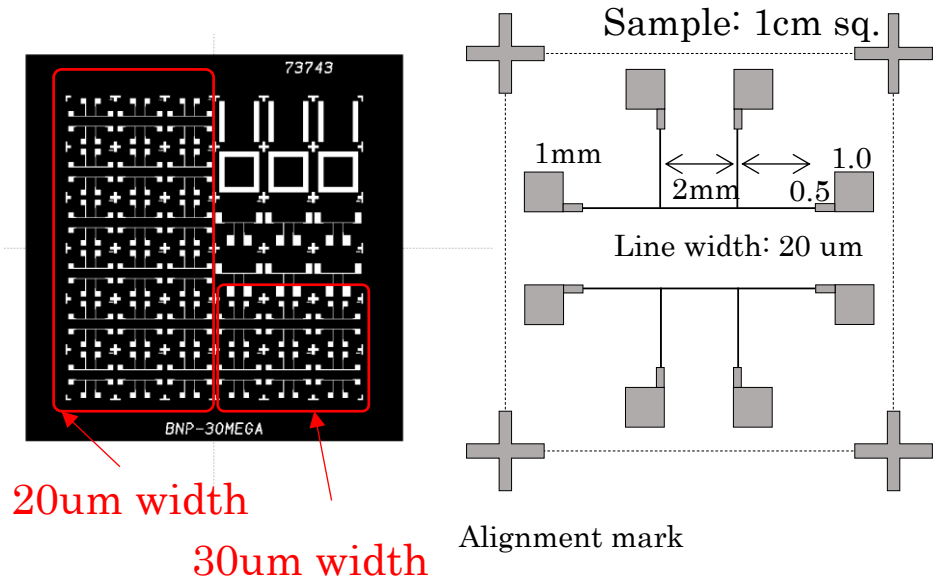

Figure 3.2 Photograph of photolithography mask and schematic figure of electrode pattern of 3ω method.

3.4 Implementation of 3ω Method

The implementation of 3ω method is shown in Figure 3.3. If the metal pattern 3ω method measurement is set on probes, electric signal at frequency ω can be output by function generator. With the analysis written on chapter 3.2, increase of 3ω pattern's temperature $\Delta T(\omega)$ should appear. Through the measurement of this electric signal, the relation between the electric signal

and temperature changes can be derived (shown in formula 3-1). In this relation, we can approximate that electric signal frequency and temperature changes have a linear relationship at the certain frequency region which depends on substrate materials. Therefore, the electric signals with different frequency must be distinguished. But there is a problem that the electric from 1ω to 3ω signals are mixed. In order to solve this issue, the Fourier transform was employed to split measured voltage signal into 1ω and 3ω signals. All these operations are performed by the data logger and controlled by the LabVIEW programs we made (Figure 3.4). Another use of this formula is that the temperature changes can also be derived from the 3ω signal. The thermal conductivity of the substrate is derived from the slope in the linear relationship. Furthermore, based on the substrate's data with identical conditions, the thermal conductivity is derived while the thin film samples' data are also measured. According to formula 3-4, the thermal conductivity can be simply calculated out by eliminating the substrate component.

The measurement system consists of probes, function generator, computer, software and the LabVIEW hardware.

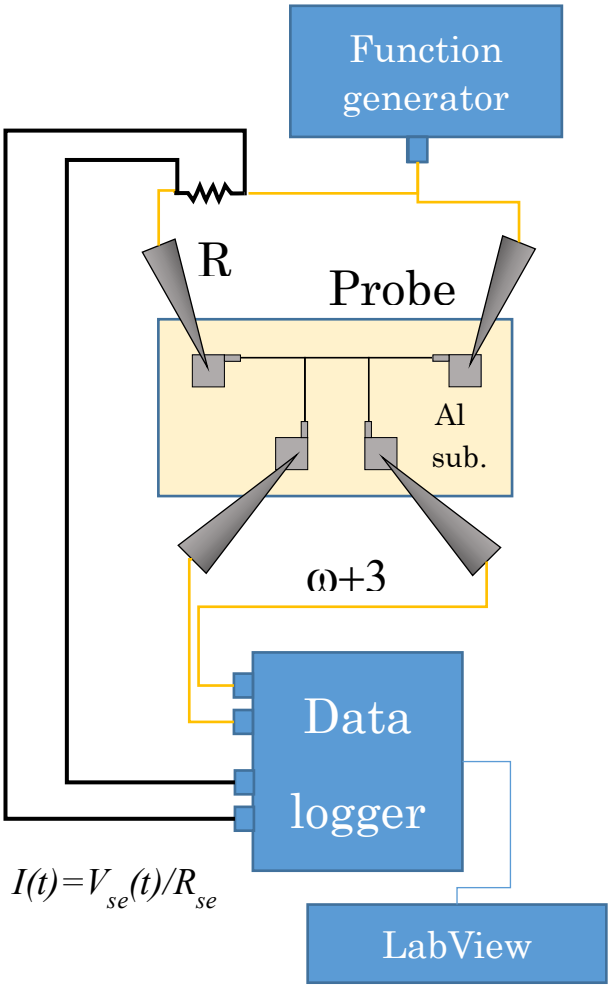

Figure 3.3 Block diagram of 3ω method[10].

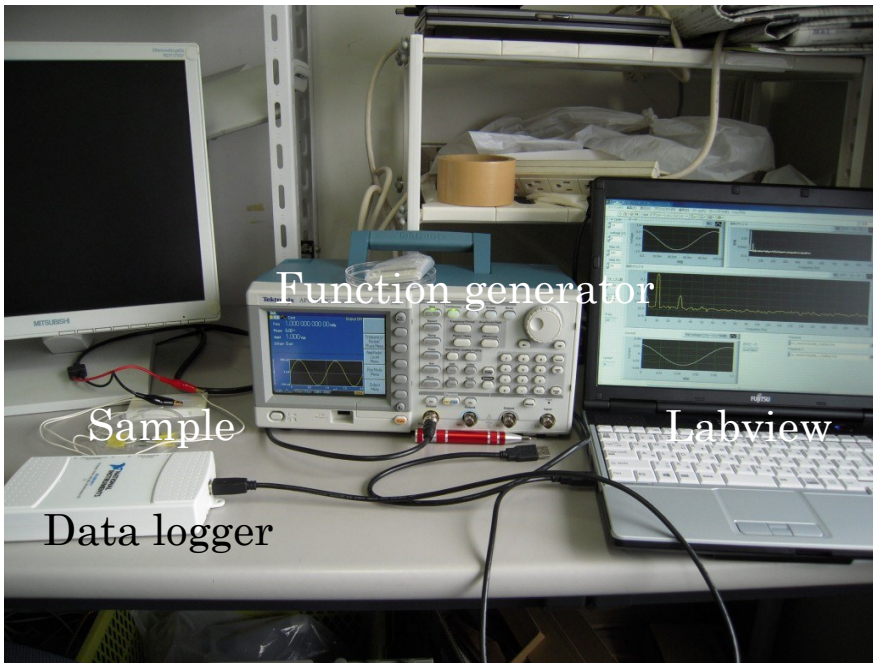

Figure 3.4 Basic equipment consists in our 3ω measurement system.

3.5 Results and Discussion

The 3ω measurement system includes sample preparation and measurement equipment. For the sample preparation, the choice of substrate and thickness of insulator film must be considered at first. On the other side, the set value for voltage and frequency, noise from function generator and contact resistance values with different probes also must be adjusted to carry out the measurement.

As choice of substrate, the basic rule is that the substrate should have higher thermal conductivity than the target film. SiO_2 was chosen as the target film material because SiO_2 is a standard insulator material and the properties is very well- known which makes checking the results convenient. With the measurement system introduced before, measurements were taken on the

alumina and Yttria-stablized-zirconia (YSZ) substrates with 1000 nm SiO_2 thin film deposited by plasma-enhanced chemical vapor deposition (PECVD). From the results (Figure 3.5), it was noted that 3ω method evaluation still exist some issues such as the thermal conductivity values for SiO_2 deviated from normal region and same target film but different value meanwhile the error bar is wide. In order to solve the issues, Test experiments were done with various substrate materials and thickness of insulator film, respectively. SiO_2 thin film with different thickness such as 500 nm and 1000 nm were deposited on various substrates by PECVD at same conditions. Finally, it was found that there is no significant dependence between thickness of insulator film and thermal conductivity value.

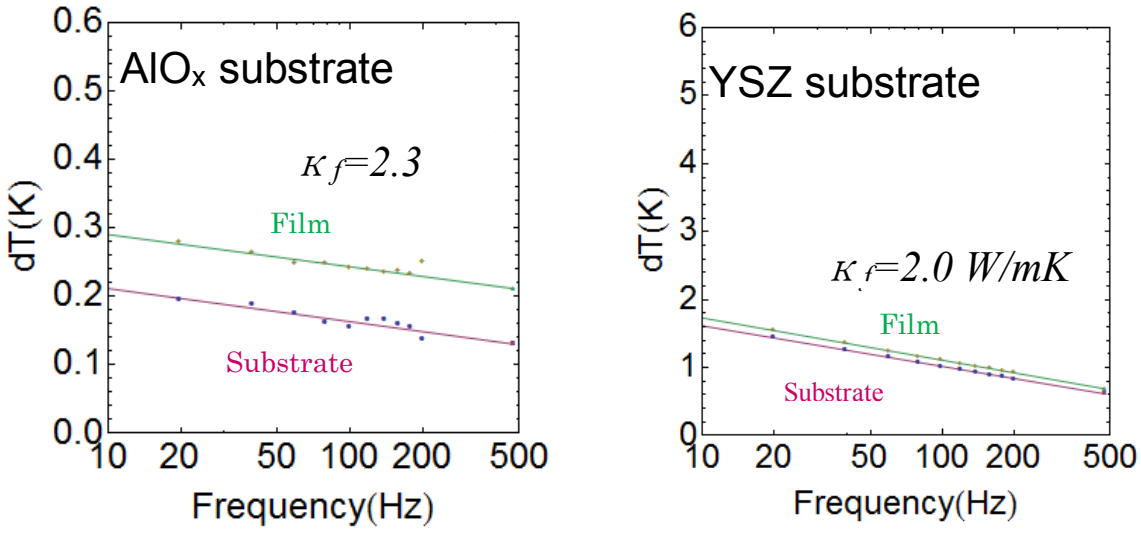

Figure 3.5 Thermal conductivity results of SiO_2 thin film by 3ω method on alumina and YSZ substrates.

In the measurement results (Figure 3.5), even though the same voltage

signal was used, the substrate with higher thermal conductivity like alumina can get much weaker feedback which appears as small ΔT values. On the other hand, strong feedback will happen by using lower thermal conductivity substrates like YSZ substrate. From the derivation of 3ω method formula, the approximation conditions should be discussed. Aside from the relation of substrate and target thin film, in order to keep linear approximation correct, the frequency of electrical signal during measurement must be set in a certain region depending on the substrate materials, electrode pattern size[11, 12], and other factors. This region has been calculated for various substrate materials which were chosen from a wide range of thermal conductivity values (Figure 3.6). From these results, high thermal conductivity substrate materials have wider linear region. Therefore, the wider frequency region can be used as the 3ω measurement. However, because of weak feedback, the electrical signal cannot be detected due to the voltage signal overlapping with the noise signal from function generator. Therefore, after the analysis of the results of the test experiment, aluminum oxide was chosen as the substrate material. This choice depends on our equipment and fabrication process limits.

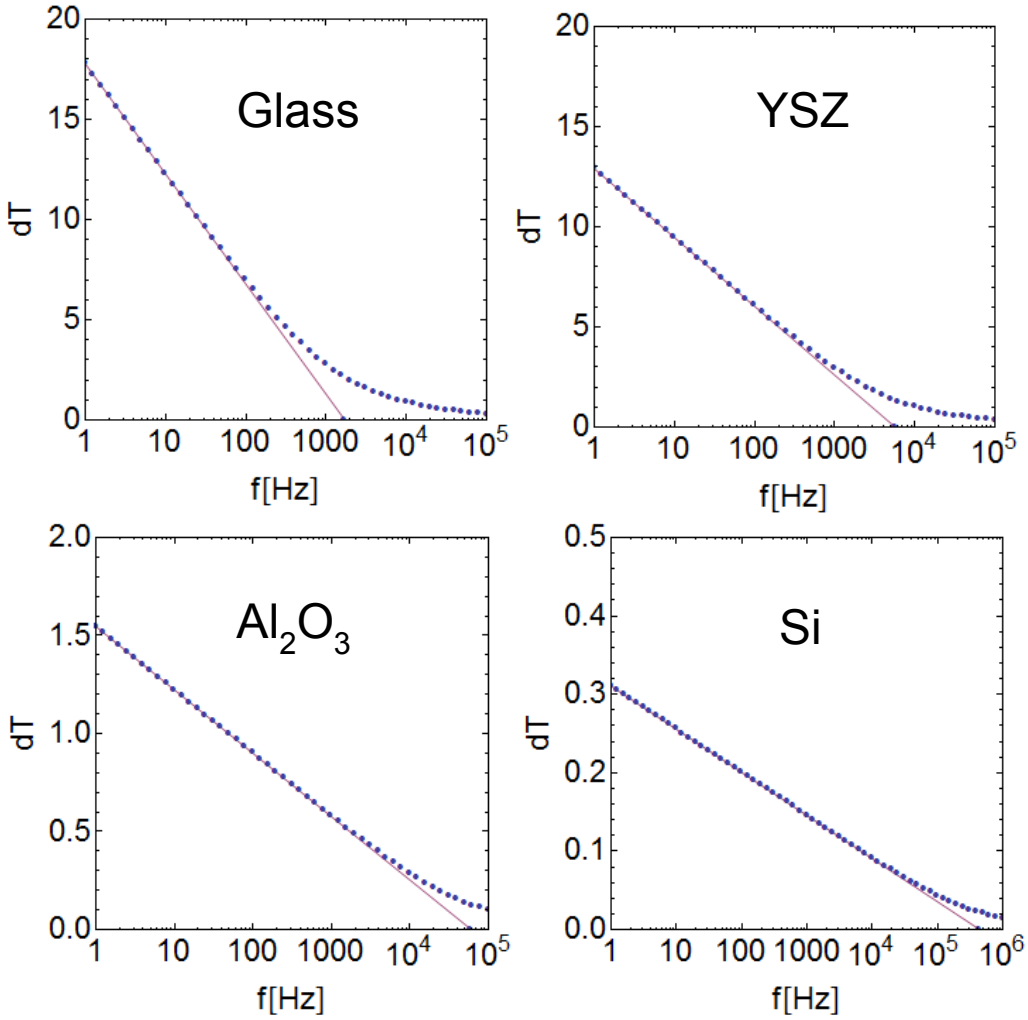

Figure 3.6 Measurement of electric signal frequency's dependency on substrate materials, electrode size, etc.

Besides the frequency, the output electric signal voltage also should be considered. The highest value of voltage in our function generator is 10 V, thus voltage from 4 V to 10 V in step of 2 V has been tested. The results of temperature changes showed that higher voltage output induces a greater temperature change. Considering the noise from equipment itself, measurement cannot be taken accurately without enough feedback from the

temperature change. According to results (Figure 3.7), it is known that the feedback is not stable when voltage is under 8 V. Consequently, high voltage must be used.

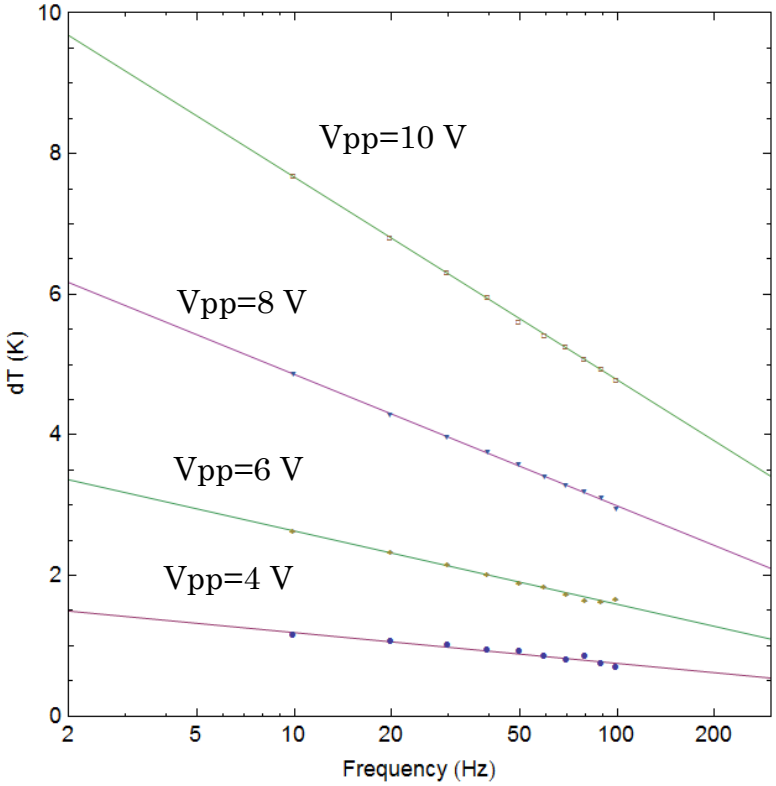

Figure 3.7 Temperature change's dependency of output electric signal voltage.

Aside from the frequency and voltage of the electrical signal, the contact resistance and temperature coefficient of resistance are also important parameters for 3ω measurement. The equipment we set up uses type K thermocouple (Nickel-Chromium / Nickel-Alumel) at a temperature region ranging from -270 to 1260°C with accuracy of ±2.2°C to measure the temperature of the electrode. The control program for temperature

coefficient of resistance measurement is made by LabVIEW (Figure 3.8 (a)). The electrode is warmed up by the current via small temperature changes, then cooled down naturally. The electrode resistance is measured during the temperature change. It should be a linear relationship and the slope value is the temperature coefficient of resistance. Here attention should be given to the measurement conditions of temperature coefficient of resistance and 3ω measurement. And a gold probe is used in order to decrease contact resistance (Figure 3.8 (b)). The probe material properties and size can both reduce the contact resistance.

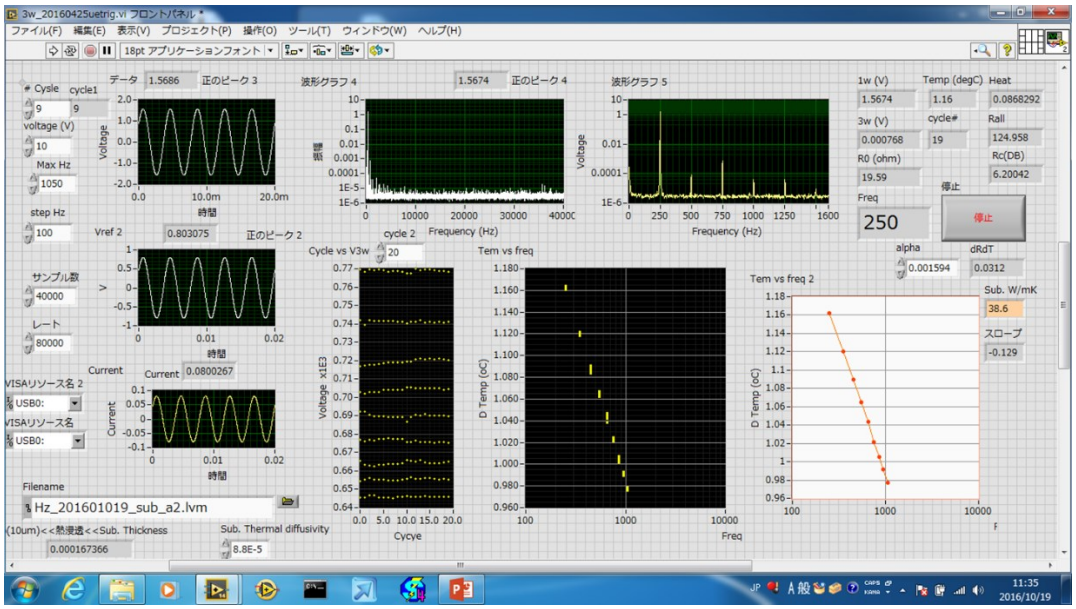

(a)

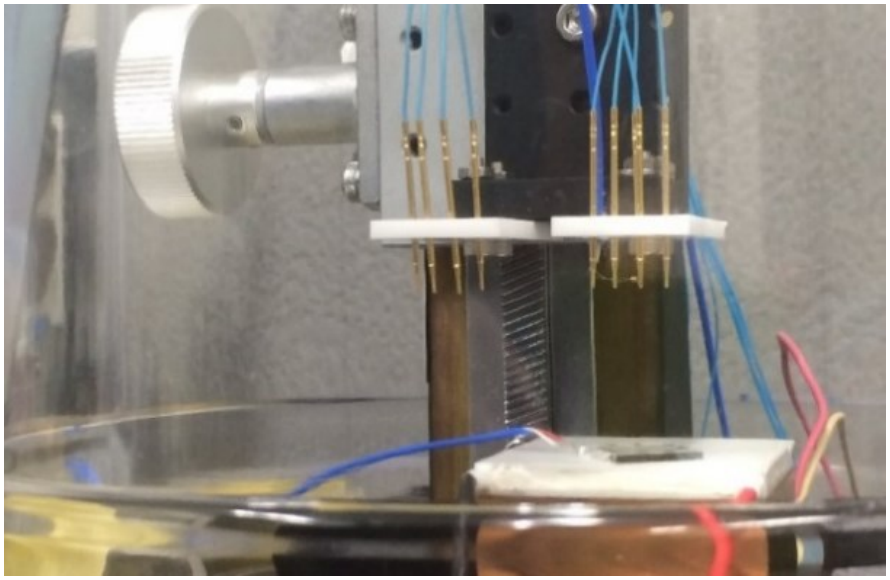

(b)

Figure 3.8 3ω measurement's program interface and probes of system.

The reason for the reduction of contact resistance and temperature coefficient of resistance is explained by approximate calculation according to the formula:

$$\mathrm{dT} = \frac{R_0 \mathrm{R}_a V - \sqrt{{R_0}^2 V\left({\mathrm{R}_a}^2 V + 12 \times (3R_0 + \mathrm{R}_a)^2 V_{3\omega}\right)}}{3{R_0}^2 V\alpha} \quad (3\text{-}5),$$

where R_0 is the measured electrode resistance, R_a is total resistance without 3ω electrode pattern, V is output voltage, $V_{3\omega}$ is 3ω voltage signal value, α is temperature coefficient of resistance. According to equation 3-5, we can find dT to have an inverse proportionality with α. Therefore, if there is a slight shift in the temperature coefficient of resistance, the results have a huge change. On the other hand, for contact resistance, as one part of R_a, it has direct influence on the results. Furthermore, results are more sensitive to contact resistance because the relation between contact resistance and α

depends on the measurement system. Through the analysis of experiment results, contact resistance has a threshold value region (6±1 Ω). If contact resistance is higher than this value, the results of 3ω measurement won't converge at a proper region (Figure 3.9).

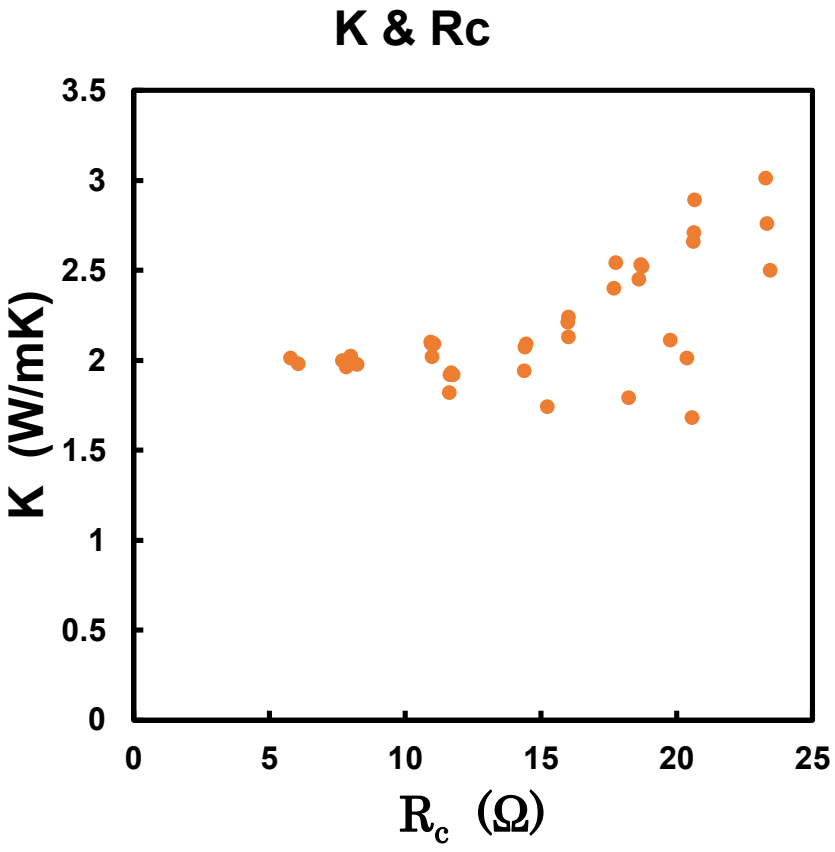

Figure 3.9 Thermal conductivity measurements' dependency of contact resistance.

3.6 Conclusion

In this chapter, 3ω method as a measurement method of thermal conductivity was introduced. The detail of fabrication process, measurement system and parameter setting were also discussed. Through the experiment

results and the theoretical analysis, the stability of 3ω measurement is sensitive to key sizes of electrode pattern and setting parameter.

For the fabrication process, photolithography was used at first. It is really essential to understand the effect of the electrode pattern size. Then, the metal mask was introduced into this study. From optimization of electrode materials, thickness of insulator film, setting parameters of output electrical signal, and others, the ideal conditions were found.

Through the equipment set up, the detail of 3ω measurement can be discussed such as choice of substrate, output voltage signal's amplitude and frequency, contact resistance measurement. Furthermore, even the equipment details such as choosing the correct probe or the noise from function generator were considered and optimized. Finally, the 3ω measurement system we set up was tested, and it was proven that the system was reliable and appropriate. After this chapter, this method is used as an experimental method to measure thermal conductivity of nanocomposited structure samples.

References

[1] D. G. CAHILL, *Thermal Conductivity Measurement from 30 to 750 K*: *the 3ω method*, Rev. Sci. Instrum. 61, 802-808 (1990).

[2] S. M. LEE and D. G. CAHILL, *Heat Transport in Thin Dielectric Films*, J. Appl. Phys. 81, 2590-2595 (1997).

[3] S. M. LEE, D. G. CAHILL and R. VENKATASUBRAMANIAN, *Thermal Conductivity of Si-Ge Superlattices*, Appl. Phys. Let. 70, 2957-2959 (1997).

[4] T. BORCA-TASCIUC, J. L. LIU, T. ZHENG, W. L. LIU, D. W. SONG, C. D. MOORE, G. CHEN, K. L. WANG, M, S, GOORSKY, T. RADETIC and R. GRONSKY, *Temperature Dependent Thermal Conductivity of Symmetrically Strained Si/Ge Superlattices*, ASME HTD 364-3,117-123 (1999).

[5] J. H. KIM, A. FELDMAN and D. NOVOTNY, *Application of the Tree Omega Thermal Conductivity Measurement Method to a Film on a Substrate of Finite Thickness*, J. Appl. Phys.86, 3959-3963 (1999).

[6] R. VENKATASUBRAMANIAN, *Lattice Thermal Conductivity Reduction and Phonon Localization Like Behavior in Superlattice Structures*, Phys. Rev. B 61, 3091-3097 (2000).

[7] T. BORCA-TASCIUC, W. L. LIU, J. L. LIU, T. ZHENG, D. W. SONG, C. D. MOORE, G. CHEN, K. L. WANG, M. S. GOORSKY, T. RADETIC, R. GRONSKY, T. KOGA and M. S. DRESSELHAUSS, *Thermal Conductivity of Symmetrically Strained Si/Ge Superlattices*, Superlattices Microstruct. 28, 199-206 (2000).

[8] S. T. HUXTABLE, A. R. ABRAMSON, C.-L. TIEN, A. MAJUMDAR, C. LABOUNTY, X. FAN, G. ZENG, J. E. BOWERS, A. SHAKOURI and E. T.

CROKE, *Thermal Conductivity of Si/SiGe and SiGe/SiGe Superlattices*, Appl. Phys. Lett. 80, 1737-1739 (2002).

[9] T. BORCA-TASCIUC, D. W. SONG, J. R. MEYER, I. VURGAFTMAN, M.-J. YANG, B. Z. NOSHO, L. J. WHITMAN, H. LEE, R. U. MARTINELLI, G. W. TURNER, M. J. MANFRA and G. CHEN *Thermal Conductivity of* $AlAs_{0.07}Sb_{0.93}$ *and* $Al_{0.9}Ga_{0.1}As_{0.07}Sb_{0.93}$ *Alloys and* $(AlAs)_1/(AlSb)_1$ *Digital Alloy Superlattices*, J. Appl. Phys. 92,4994-4998 (2002).

[10] S. Tanaka: Dr. Thesis, Graduate School of Life Science and Systems Engineering, Kyushu Institute of Technology, Kyushu (2011).

[11] S. M. LEE and D. G. CALHILL *Heat Transport in Thin Dielectric Films* J. Appl. Phys. 81, 2590-2595 (1997).

[12] T. BORCA-TASCIUC, R. KUMAR and G. CHEN *Data Reduction in 3ω Method for Thin-film Thermal Conductivity Determination* Rev. Sci. Instrum. 72, 2139-2147 (2001).

● Chapter 4

4 Effects of NPs in Bismuth Telluride Thin Film

4.1 Introduction

In 1954, Goldsmid demonstrated the excellent thermoelectric properties of bismuth telluride, which were attributed mainly to the large mean molecular mass, low melting temperature and partial degeneracy of the conduction and valence bands of V-VI chalcogenide[1]. Therefore, bismuth telluride has been widely studied as an excellent thermoelectric (TE) material, and it has a perfect performance in the temperature range around 300 K, especially. The non-cubic structure of bismuth telluride contributes to the anisotropy in thermoelectric properties, physical characteristics, as well as the diffusion coefficients of impurities or dopants. It has a tetradymite structure with space group R3m and the lattice is stacked in a repeated sequence of five atom layers: Te^1-Bi-Te^2-Bi-Te^1 along the c-axis (Figure 4.1). The superscripts 1 and 2 show differently bonded tellurium atoms. Te and Bi layers are held together by strong ionic-covalent bonds (Te^1-Bi and Bi-Te^2). The Te^1 bonds between cells are of the van der Walls type and are extremely weak.

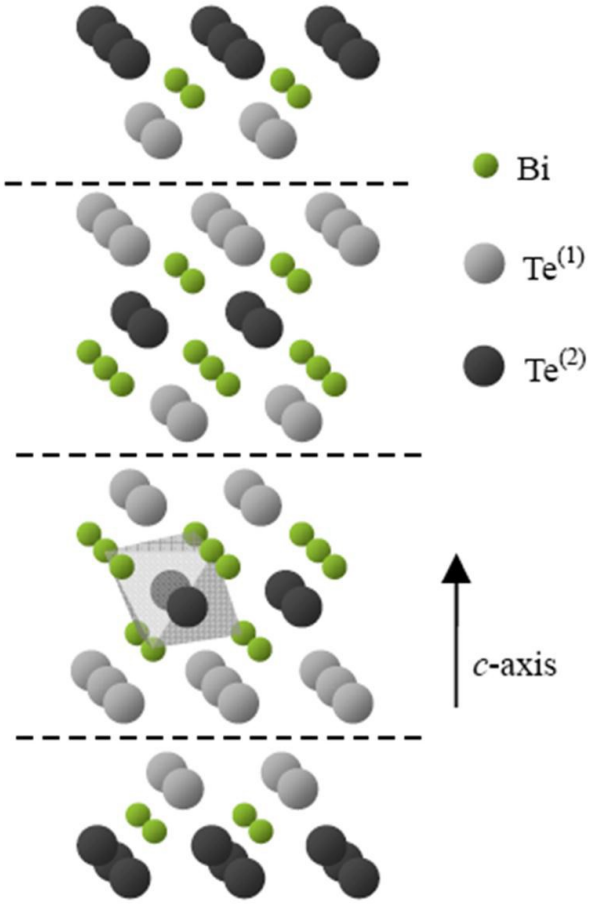

Figure 4.1 Atomic layers in the Bi_2Te_3 crystal structure. Dashed lines indicate van der Walls gaps. The octahedral coordination is highlighted for a $Te^{(2)}$ atom.

There has been a wide variety of power generation device created as a thermoelectric device at the macro scale. Nevertheless, utilizing thermoelectric thin films which can be deposited directly onto the surface of the substrate are more suitable for micro-scale systems. Because the films are not formed under equilibrium conditions and are usually amorphous or polycrystalline, their properties can vary significantly from their single crystal bulk counterparts. (Bi,Sb)Te-based alloys are the best-performing materials near room temperature in bulk form. Therefore, their thin films

have received significant attention as the TE material of choice for microsystems. Because of their compatibility with integrated circuits technology, polycrystalline SiGe alloys and polycrystalline Si are also commonly used in thermoelectric applications. Their use in TE micro coolers and generators have also been investigated. However, their thermoelectric performance is very low compared to that of BiTe compounds[2, 3].

Although ternary alloys have shown increased TE figures of merit over binary films, in order to obtain ZT > 1, superlattices and nanostructured materials have been explored recently. In either case, quantum confinement in one, two, or three dimensions reduces phonon conduction. Therefore, thermal conductivity in that direction is lowered while maintaining electrical conduction, which leads to increasing ZT[4, 5].

Novel experimental results have been reported in recent years to demonstrate increased ZT using nanostructured materials such as thin-film superlattices[6, 7] and thick films of quantum-dot superlattices[8]. Superlattices use alternating layers of different materials with thickness of 1-40 nm in order to create an artificial lattice constant that can influence the dispersion of both electrons and phonons. The lattice mismatch, electronic potential differences at the interfaces, resulting phonon and electron interface scattering, and band structure modifications can be exploited to reduce phonon heat conduction while maintaining or enhancing the electron transport[9]. The most successful results of superlattice research have used MOCVD to produce p-type Bi_2Te_3/Sb_2Te_3 material with a ZT of 2.4, and n-type $Bi_2Te_3/Bi_2Te_{2.7}Se_{0.3}$ material with a ZT of 1.4[10-12].

As nanostructure has been introduced into TE field and led high performance of TE devices. Therefore, it should be expected that Bi_2Te_3 film concluding nanoparticles (NPs) is a high potential TE composited material. To improve the efficiencies of TE materials, TE materials with nanostructure have shown that these materials' thermal conductivities can be reduced through scattering phonon[13], optimization of their electrical properties due to filtering effect[14, 15] or doping. In addition, fabricating NPs with uniform size and controlled distance between NPs is still difficult.

To overcome these problems, we have utilized BNP[16] in this study. BNP uses ferritin, which is one of the proteins that can fabricate NPs with uniform size and distribute them accordingly. PEG-ferritin can control distribution of NPs[17]. As written in chapter 2, we have found the way we can harness the BNP method to control the NPs' separated distances in a certain region, which is shorter than the phonon's Mean Free Path (MFP) and longer than the electron's MFP. In the materials with controlled NPs' distances in Bi_2Te_3 thin films, thermal conductivities were decreased and Seebeck coefficients and electrical conductivities were not changed. Consequently, ZT can be increased[18]. In our research, we optimized the protein concentration, ion strength, rotation speed of spin-coater and chemically modified ferritin, etc. We achieved to control the distance of NPs around 40 nm. Compared to the MFP, that distance is suitable to reduce the thermal conductivity in Bi_2Te_3.

4.2 One-layer nanocomposited structure

$Bi_{0.4}Te_{3.0}$ $Sb_{1.6}$is used as the BiTe thin film, in this study, due to its higher performances compared with highly doped BiTe film[19]. As the first step, thin film were deposited with one layer of NPs. Then, the electrical properties and thermal conductivity of thin film were evaluated to discuss the effect of NPs.

4.2.1Preparation of Sample

Since BiTe is a common TE material, there are a lot of methods to fabricate the BiTe thin film. . Besides the bulk materials' fabrication methods, the fabrication process can be divided into two directions: one is through vacuum process such as sputtering, molecular beam epitaxy (MBE), metal organic chemical vapor deposition (MOCVD), electrochemical deposition (ECD), flash evaporation, thermal evaporation[20], pulsed laser deposition (PLD) etc. and the other one is solution processes such as printing method[21], etc. In this study, we use PLD to deposit the $Bi_{0.4}Te_{3.0}$ $Sb_{1.6}$ thin film.

PLD is a physical vapor deposition (PVD) technique using a high-power pulsed laser beam which is focused inside a vacuum chamber to strike a deposition target of the material (Figure 4.2). This material is vaporized from the target (in a plasma plume) and deposited on a substrate (such as a sapphire substrate facing the target) as a thin film. This process can occur in high vacuum or in the presence of a background gas, such as argon which is commonly used while depositing films to avoid oxidation. For the PLD conditions, we used a laser with power of 0.1 W/cm^2 at a frequency of 5 Hz

in ambient Ar gas with pressure of 17.7 mPa and flow rate of 1 sccm. The substrate heater was set at 250°C.

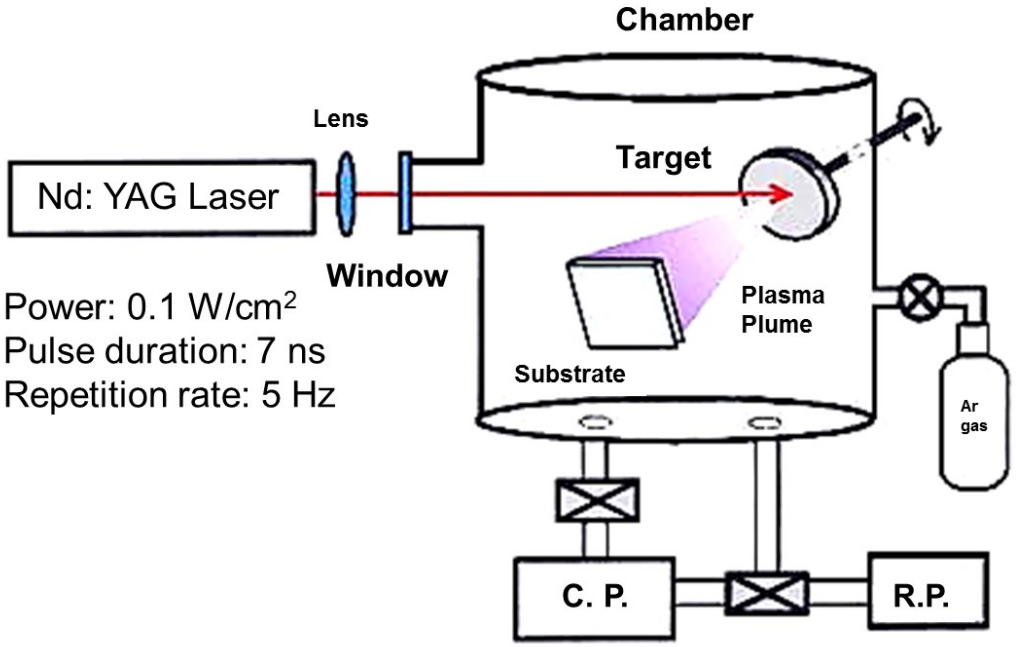

Figure 4.2 Schematic figure of PLD equipment.

(http://www.chm.bris.ac.uk/laser/ashfold/ablation.htm)

In this experiment, we made two plans in order to investigate position dependence of NPs' layer. Plan A is to deposit 100 nm $Bi_{0.4}Te_{3.0}$ $Sb_{1.6}$ thin film first, then distribute the NPs, and finally deposit $Bi_{0.4}Te_{3.0}$ $Sb_{1.6}$ thin film again. Plan B is to deposit 50 nm SiO_2 which is convenient for NPs' distribution at first, then deposit $Bi_{0.4}Te_{3.0}$ $Sb_{1.6}$ thin film after the NPs are distributed (Figure 4.3). The $Bi_{0.4}Te_{3.0}$ $Sb_{1.6}$ thin film was deposited by PLD at conditions given above. SiO_2 film was deposited by TEOS-PECVD at conditions of O_2 flow rate of 300 sccm, TEOS (Tetraethyl orthosilicate) flow

rate of 3 sccm, pressure of 80 Pa, temperature at 300°C and RF power at 150 W.

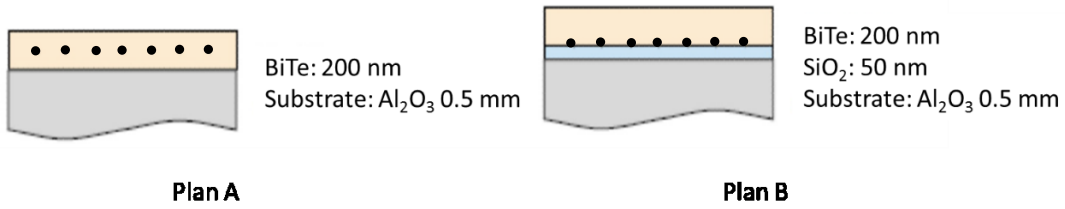

Figure 4.3 Schematic figure of plan A and B.

In plan A and B, to compare the mean free path length of phonons, PEG2k, 10k-ferritin was chosen for BNP in order to find different effects of different SD of NPs in polycrystalline $Bi_{0.4}Te_3Sb_{1.6}$ thin film. According to the introduced evaluation system in chapter 2, SEM images for NPs distribution on surface of $Bi_{0.4}Te_{3.0}$ $Sb_{1.6}$ thin film (Figure 4.4) and RDF results for PEG10k sample (Figure 4.5) show that PEG2k could not make uniform SD but PEG10k was able to make SD at about 46 nm. From calculation, the density of NPs of $4.1x10^{10}$ dot/cm^2 and $1.9x10^{11}$ dot/cm^2 are attained for PEG10k and PEG2k, respectively. Furthermore, the SD of PEG2k has an average value smaller than 30 nm.

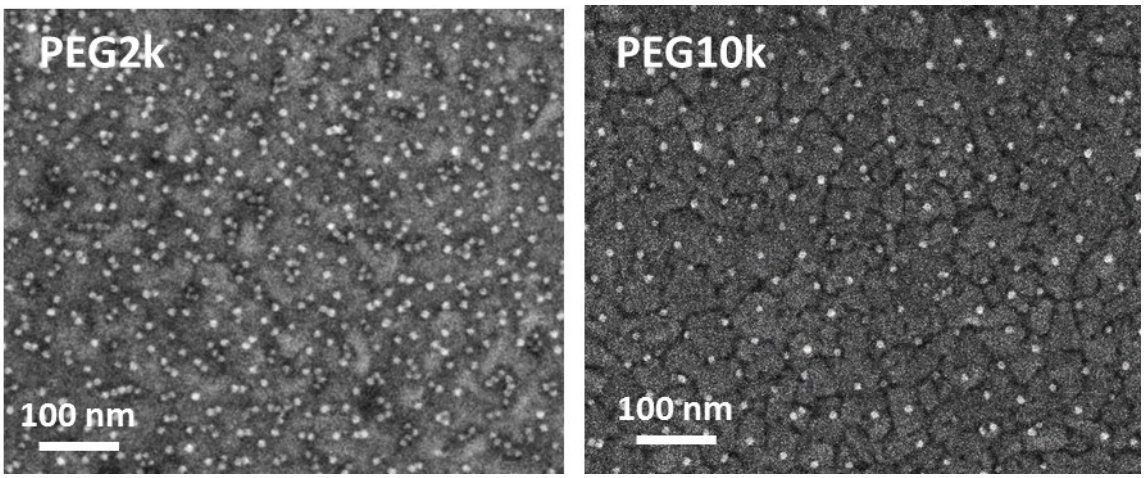

Figure 4.4 SEM images of PEG2k, 10k-ferritin on $Bi_{0.4}Te_{3.0}$ $Sb_{1.6}$ film.

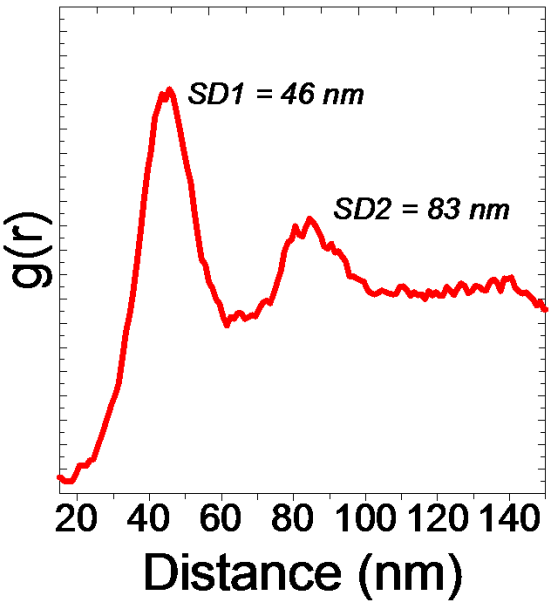

Figure 4.5 RDF results of PEG10k-ferritin on $Bi_{0.4}Te_{3.0}$ $Sb_{1.6}$ film.

After distribution of PEG-ferritin, UV/Ozone treatment at conditions of 40 min and 115°C was done to remove protein shell and PEG on it. In order to confirm the elimination of organic materials and the existence of NPs, XPS (X-ray Photoelectron Spectroscopy) was used to check for residual organic

materials. From the results (Figure 4.6), the carbon 1s peak and nitrogen 1s peak from PEG-ferritin distribution disappeared, indicating that protein and modified PEG was removed completely. But there was still a small carbon 1s peak left which is considered as impurities on substrate due to long time storage. Therefore, more measurement should be taken to investigate the organic residues after UV/Ozone treatment. AFM (Atomic Force Microscope) and FT-IR (Fourier Transform Infrared Spectroscopy) measurements were carried out to confirm organic residues on substrate after UV/Ozone treatment.

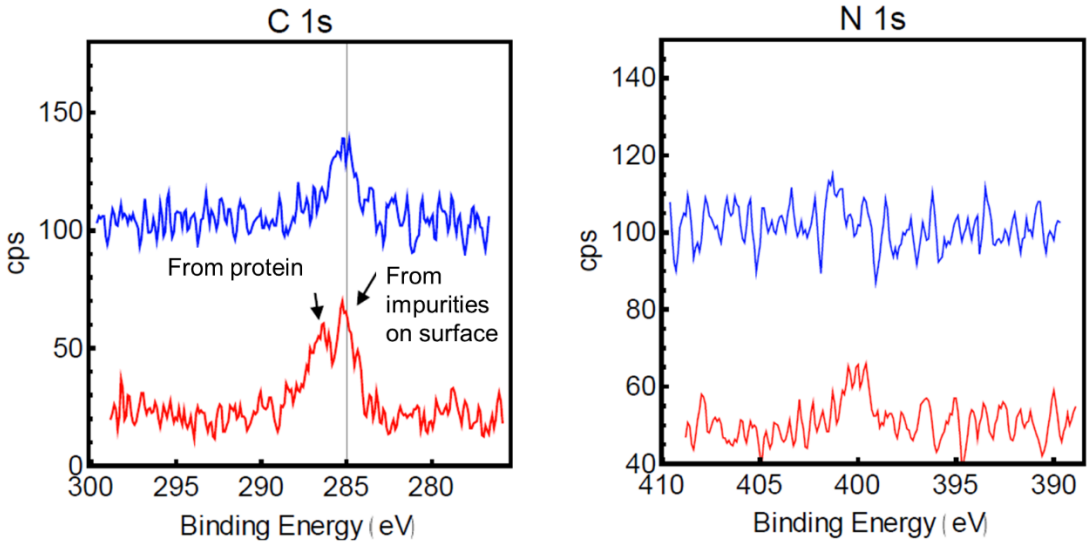

Figure 4.6 XPS results of carbon 1s and nitrogen 1s for samples with protein before and after UV/Ozone treatment comparing to reported data[22].

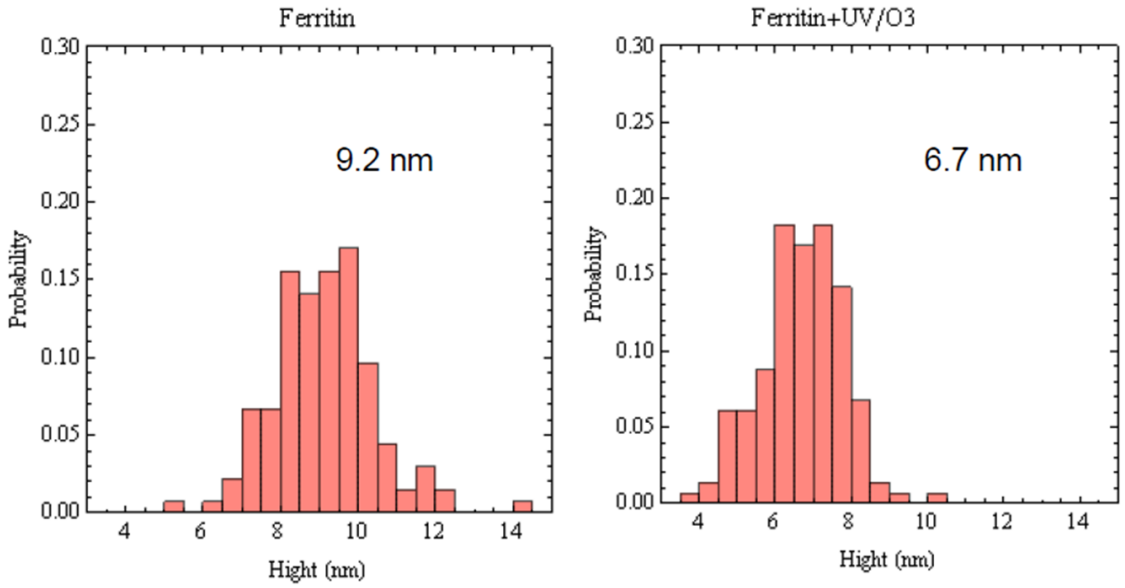

Figure 4.7 AFM results for PEG-ferritin on substrate before and after UV/Ozone treatment.

For AFM measurements, the probe detected a square region, the PEG-ferritin can be observed due to an increased height over the average height of the substrate. From the results (Figure 4.7), the reduction of height, which is more than 2 nm, can be observed after UV/Ozone treatment, indicating that the protein shell should already be removed and also observed by comparing this to the diameter data in chapter 2. This is a direct way to detect the height change after UV/Ozone treatment, and to prove the elimination of organic materials.

4.2.2 Result and Discussion

In contrast to plan A, plan B samples' NPs did not have a significant change

compared to samples without NPs, which is explained by the position of NPs in samples at the bottom of thin film. Because of surface position, NPs do not have enough contact surface with the film. Consequently, no significant effects of NPs can be observed. Therefore, we only show and discuss the results in plan A.

For evaluation of the sample with electrical properties of Seebeck coefficient, electrical resistivity and thermal conductivity, the direct measurement of voltage with a temperature gradient for Seebeck coefficient, Hall effect measurement for electrical and TDTR (Time-Domain Thermoreflectance) method for thermal conductivity were measured. TDTR is a method according to the mechanism that the reflectance of the film changes while temperature is changing. This is detected by the probe laser while the film is being heated up by pump laser irradiation. If the temperature is known, the thermal diffusivity can be derived from the equation below.

$$\mathrm{T(t)} = \frac{Q}{C}\left[1 + 2\sum_{n=1}^{\infty}(-1)^n \exp\left(-(n\pi)^2 \frac{t}{\tau}\right)\right] \quad (4\text{-}1)$$

Where T is the temperature of specimen, Q is the total energy absorbed by the specimen, C is the heat capacity of the specimen, and τ is the characteristic time of heat diffusion across the specimen.

$$\alpha = \frac{d^2}{\tau} \quad (4\text{-}2)$$

In equation 4-2, α is thermal diffusivity of specimen, d is thickness of specimen.

Then, thermal conductivity can be derived from thermal diffusivity through the equation $\kappa = \mathrm{C} \cdot \alpha$ (4-3). According to the thermal conductivity results

measured by TDTR method (Table 4.1), only one layer of NPs cannot affect the scattering phonon. Furthermore, thermal conductivity increased due to higher thermal conductivity of NPs than $Bi_{0.6}Te_3Sb_{1.6}$film.

Table 4.1 Thermal conductivity results from TDTR method by picosecond laser.

Samples	Thermal conductivity (W/mK)
Film concluding high density NPs	0.64
Film only	0.4

Hall effect is a well known method for measuring electrical properties, such as density and carrier mobility. Then, the electrical resistivity can be derived from equation $\sigma = n\mu e$ (4-4) and $\rho = 1/\sigma$ (4-5), where σ is electrical conductivity, n is carrier density, μ is carrier mobility, e is carrier charge, and ρ is electrical resistivity.

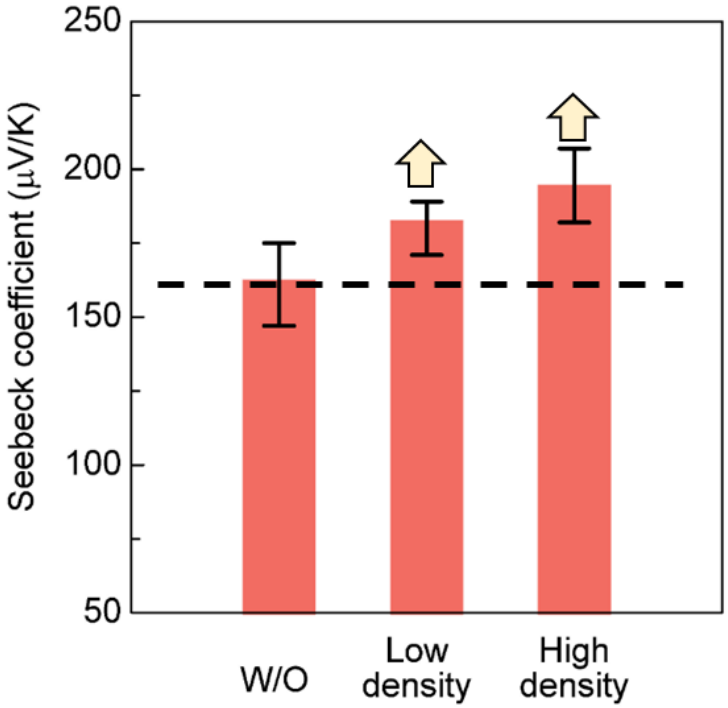

Figure 4.8 Seebeck coefficient results for samples with one layer at high and low density of NPs, and without NPs.

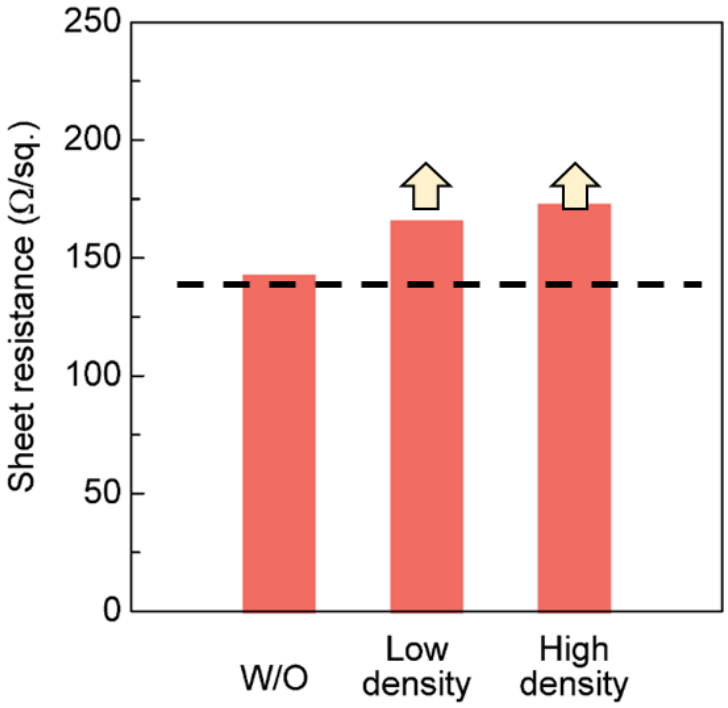

Figure 4.9 Electrical resistivity results for samples with one layer at high and low density of NPs, and without NPs.

As the Seebeck coefficient results (Figure 4.8) and electrical resistivity results (Figure 4.9) show, the Seebeck coefficient increased along with increasing density of NPs. Also, electrical resistivity decreased along with increasing density of NPs, which means that the NPs used here can cause the Seebeck coefficient to increase and electrical resistivity to decrease. In order to explain this phenomenon, two models were found.

One is the filtering effect[14, 15], the carriers in thermoelectric materials with low energy can be located by energy potential barrier which is caused by interface of NPs and film material, leading to the increase of Seebeck coefficient. This effect leads Seebeck coefficient increase with electrical resistivity also increase little. Because of the relation between ZT and Seebeck coefficient, which is expressed in $ZT=\sigma S^2T/\kappa$, change of ZT is more sensitive to Seebeck coefficient changing due to second power. About the explanation of filtering effect, the Seebeck coefficient should be analyzed at first. The seebeck coefficient can be written as

$$S = \frac{1}{eT}\frac{\int_0^\infty E\tau(E)(E-E_f)g(E)\partial_E f_0 dE}{\int_0^\infty E\tau(E)g(E)\partial_E f_0 dE} \quad (4\text{-}6)$$

which is derived by Boltzmann transport equation (BTE). Where g(E) is the density of electronic states, $f_0(E)$ is the Fermi–Dirac function, e is the carrier charge, $\tau(E)$ is the energy-dependent carrier relaxation time, E_f is the Fermi energy, T is the absolute temperature, and here we defined $\partial_E = \partial/\partial E$. As

electrical conductivity here can be written as

$$\sigma(E) = -\frac{2e^2}{3m^*} E\tau(E)g(E)\partial_E f_0 \quad (4\text{-}7),$$

where m* is the effective mass of the carrier. Seebeck coefficient can be derived as

$$S = -\frac{3m^*}{2e^3T} < E - E_f >_\sigma \quad (4\text{-}8),$$

where the average $<\cdots>_\sigma$ is computed using σ(E) as a statistical weight[23, 24]. Since $\partial_E f_0$ is significantly different from zero only in a narrow window around E_f, expanding formula 4-7 around E_f the equation is transformed as

$$\frac{3m^* k_B T}{2e^2}\sigma(E_f + \delta E) = E_f g(E_f)\tau(E_f) + \delta E \left(\tau(E_f)g(E_f) + E_f \left(\frac{d(\tau(E)g(E))}{dE}\right)_{E=E_f} \right) + O((\delta E)^2) \quad (4\text{-}9),$$

where k_B is Boltzmann constant, m* is the effective mass of carriers. This formula indicates that the asymmetry of the statistical weight *σ(E)* around E_f is ruled by the functional shape of *g(E)τ(E)* close to the Fermi energy, which also provides a simple explanation of the low Seebeck coefficient of metals. In spite of metals' large conductivity, both *g(E)* and *τ(E)* are almost flat around E_f, so contributions from electrons within some k_BT from E_f are almost considered as zero. However, in semiconductors, *g(E)* is always asymmetric around the Fermi energy, leading to larger Seebeck coefficient values. With this consideration, any modification of *τ(E)* may be expected that further stretch the asymmetry of *τ(E)g(E)* should lead to improvements of the Seebeck coefficient. Energy filtering is one possible strategy for this

aim.

In this experiment, as shown in the band diagram (Figure 4.10) the holes as carriers in BiTeSb go through the interface between film and NPs which consist of iron or ferric oxide. There is also a potential barrier of about 0.6 eV. This potential barrier can cause lower energy holes located by the NPs. Then, Seebeck coefficient improvement can be observed due to filtering effect.

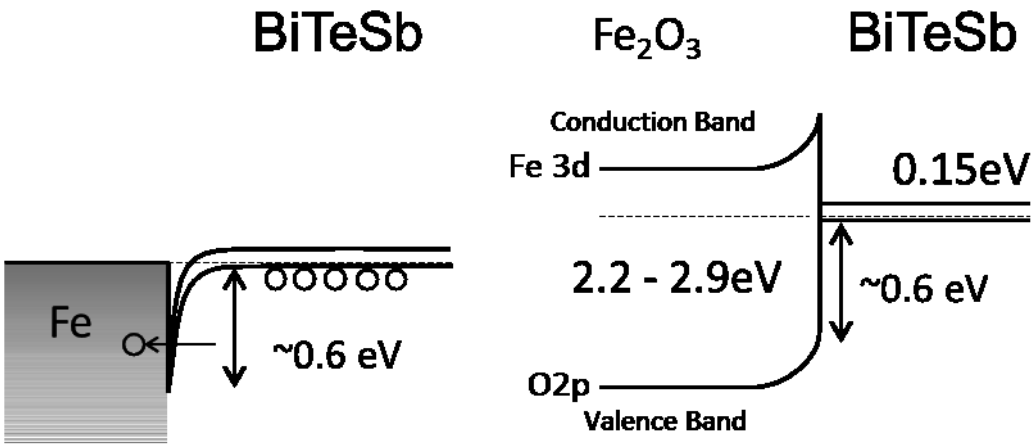

Figure 4.10 Band diagram of Fe/BiTeSb and Fe_2O_3/BiTeSb.

If energy is cut off completely by potential barrier, then Seebeck coefficient can be expressed as the formula below while dominant scattering is assumed as ionized impurity.

$$S = \frac{1}{eT}\left(\frac{4k_BTE_c^3+12(k_BT)^2E_c^2+24(k_BT)^3E_c+24(k_BT)^4+E_c^4}{3k_BTE_c^2+6(k_BT)^2E_c+6(k_BT)^3+E_c^3} - E_f\right) \quad (4\text{-}10),$$

where E_c is the value of cut off energy[25]. According to this formula, Seebeck coefficient value about 200 μV/K can be calculated out approximately.

Another explanation is the de-doping model which have two kinds of model as nondegenerate and degenerate semiconductor model[26]. In iron or ferric oxide it is assumed that carriers are electrons which de-dope the hole in film. For the de-doping process in nondegenerate semiconductor, the Seebek coefficient can be written as

$$S = \frac{k_B}{e}\left(\frac{5}{2} + \gamma - \ln\frac{\sigma}{\sigma_0}\right) \quad (4\text{-}11),$$

where γ is the scattering factor. In degenerate semiconductor, Seebeck coefficient can be written as

$$S = \frac{k_B}{e}\left(\frac{3}{2} + \gamma\right)\frac{A}{\sigma^{2/3}} \quad (4\text{-}12),$$

where A is a constant by materials. Because $Bi_{0.4}Te_3Sb_{1.6}$ is a degenerate semiconductor due to higher energy value for conduction band than Fermi energy value. Therefore, the Seebeck coefficient can be calculated by formula 4-12, in which the scattering factor was determined to have a value of -0.5[26, 27]. The results of this calculation (Figure 4.11) showed that the experimental results of Seebeck coefficient and electrical conductivity fit the theoretical calculation results. Consequently, the de-doping model can also explain the effects of NPs in the $Bi_{0.6}Te_3Sb_{1.6}$ thin film. For a good agreement between experimental and theoretical data, Seebeck coefficient increased due to the de-doping effect.

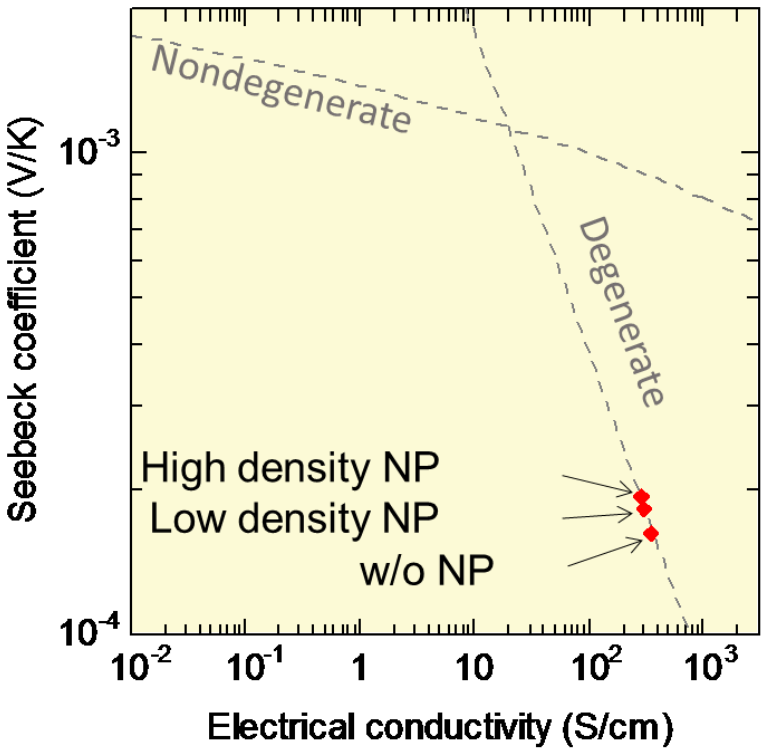

Figure 4.11 A comparison between theoretical calculation results and experimental results by Seebeck coefficient and electrical conductivity.

4.3 Multi-layers nanocomposited structure

After discussion of one layer structure, its improvement as thermoelectric materials has already been shown. For amplification of the NPs effect in thin film, we not only fabricated one layer of NPs but also a nanocomposited structure with multi-layers. Furthermore, in order to discuss the 3 dimensional nanostructure of thin film encapsulated NPs, the preparation of specimen to evaluation are discussed. Cycle processes were also taken which

is identical with plan A.

4.3.1Preparation of Sample

The conditions of fthe abrication process are almost same with one layer sample. For instance, $Bi_{0.6}Te_3Sb_{1.6}$ thin film was deposited by PLD with the same conditions. However, different NPs layer numbers lead to different thickness of $Bi_{0.6}Te_3Sb_{1.6}$ after one-time deposition, due to the total thickness of $Bi_{0.6}Te_3Sb_{1.6}$ thin film being about 200 nm. In this study, to test $Bi_{0.6}Te_3Sb_{1.6}$ thin film only samples, sample with 4 and 9 NPs layers were also fabricated with film thickness of 40 nm and 20 nm, respectively, after one-time deposition. But the processes are same as one layer structure, besides the number of times for depositing the film and distribution of PEG-ferritin. The structure of multi-layered NPs is shown in Fig. 4.12.

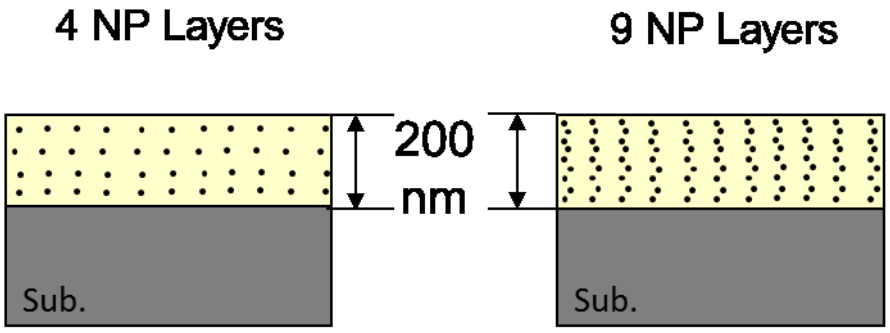

Figure 4.12 Schematic figure of multi-layers NPs composited structure with 4 and 9 layers.

After the fabrication process, in order to confirm the fabricated three dimensional nanostructure, the sample with 9 layers was observed by STEM

(Scanning Transmission Electron Microscopy) and TEM (Transmission Electron Microscope). Images of STEM is sensitive to show elements differences, and images of TEM is more sensitive to indicate the crystal structure. Therefore, the results of STEM (Figure 4.13) and TEM (Figure 4.14) images displayed the NPs with a layer by layer structure and polycrystalline NPs within amorphous film. For one layer structure, the $Bi_{0.6}Te_3Sb_{1.6}$ thin film was polycrystalline film, but in 9 layer structure which one layer NPs embedded in 20 nm film, NPs were considered as great hindrance to the growth of crystal, due to the too many NPs being embedded in film. However, the 9 layer NPs composited structure has been fabricated successfully, according to STEM image which display the layers and NPs within clearly.

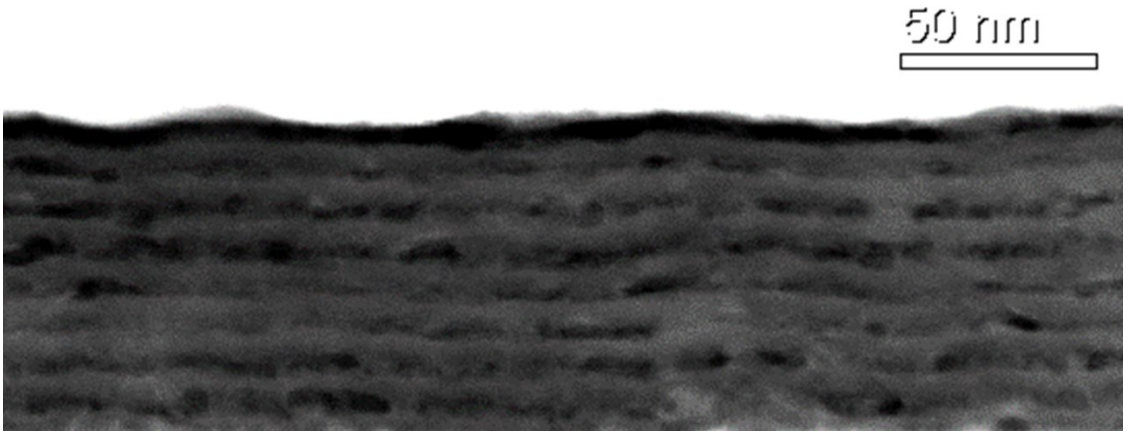

Figure 4.13 STEM image of multi-layers NPs composited structure with 9 layers.

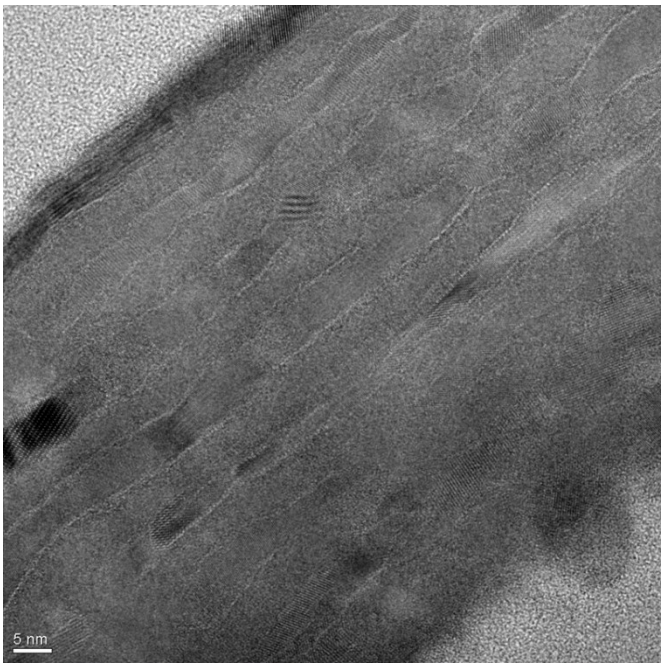

Figure 4.14 TEM image of multi-layers NPs composited structure with 9 layers.

Furthermore, the EDX (Energy dispersive X-ray spectrometry) in TEM was utilized to analyze the composition of the layer and confirm that the layer is exactly a $Bi_{0.6}Te_3Sb_{1.6}$ thin film. As the results (Figure 4.15) showed, Bi, Te and Sb uniformly exist in every layer and NPs in layer are also observed. However, the oxygen uniformly appeared in every layer which means the film is oxidized during the fabrication process. In all fabrication processes, the most possible oxidation process is considered due to long time UV irradiation for eliminating the protein shell.

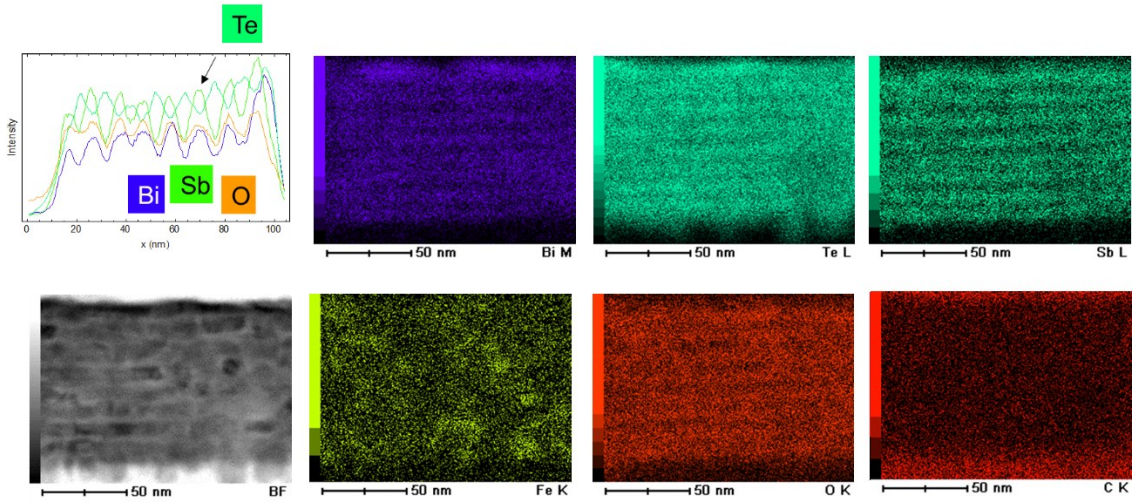

Figure 4.15 EDX images of multi-layers NPs composited structure with 9 layers.

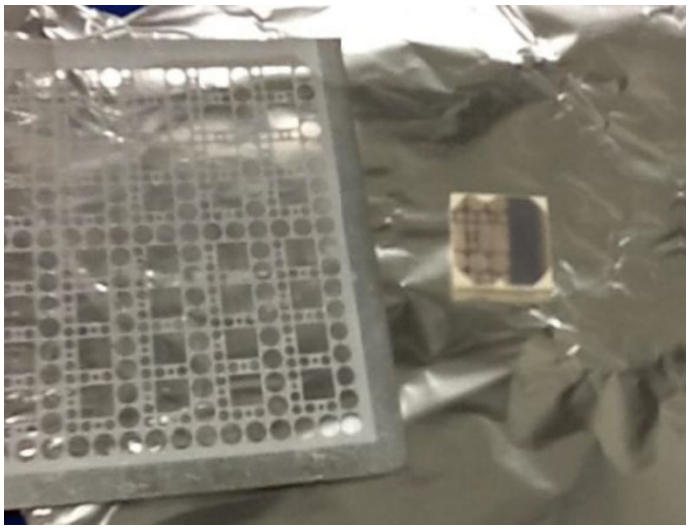

Figure 4.16 Photo of color change before and after UV irradiation.

In order to confirm the oxidation process occurs during UV irradiation, the metal mask was used to cut off the UV light during irradiation. As shown in the photo (Figure 4.16), UV irradiated part had a significant color change from covered part since UV irradiation time of 30 min. This time is shorter than PEG-ferritin elimination process, thereof the film was oxidized in PEG-

ferritin elimination process. Furthermore, the oxidation was confirmed by XPS results (Figure 4.17) between before and after 40 min UV irradiation. As the results showed, the Bi, Te and Sb were oxidized after irradiation, respectively. But from Bi to Sb the oxidation became light.

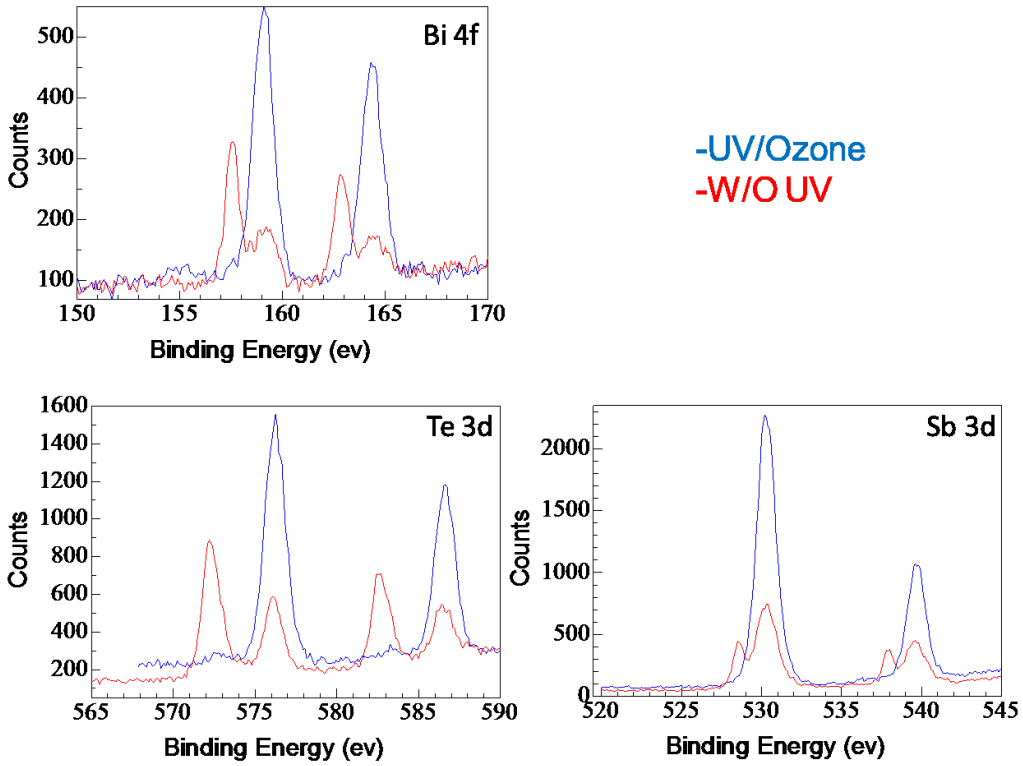

Figure 4.17 XPS results of change before and after UV irradiation for Bi 4f, Te 3d and Sb 3d electrons.

4.3.2 Result and Discussion

Another evaluation for thermoelectric research is the evaluation of thermal conductivity and it measured by the 3ω system introduced in chapter 3. The

results (Figure 4.20) as expected, thermal conductivity in the out of plane direction increased along with the increase in the number of NPs layers due to the decrease of distances between layers. Even though the measuring direction of electrical parameters and thermal conductivity are different, the results still indicate the improvement of ZT value.

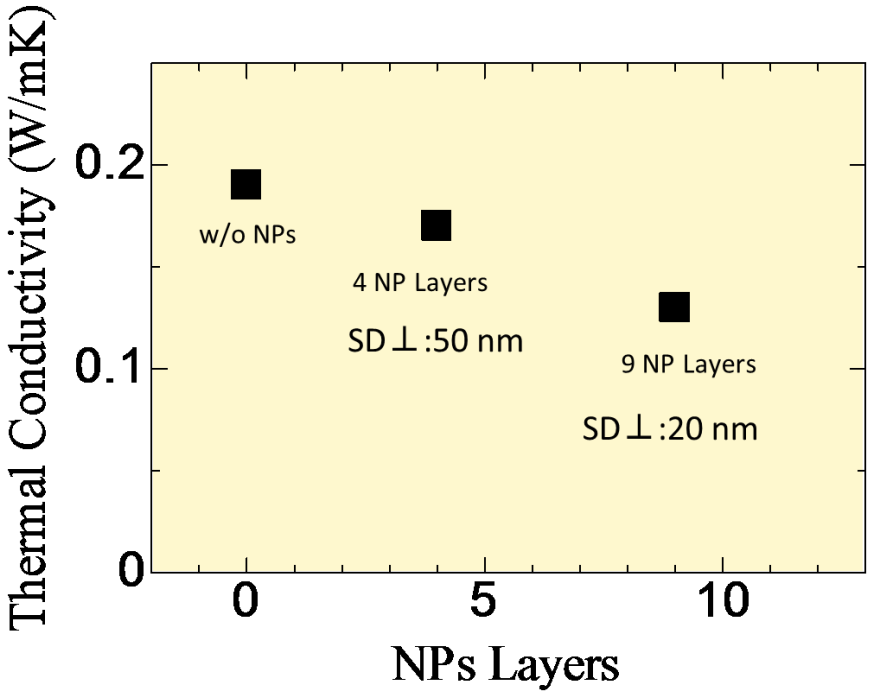

Figure 4.20 Results of multi-layers structure samples with 4, 9 layers and film only without NPs in thermal conductivity measurement.

The porosity-adapted Cahill−Pohl (p-CP) model of minimum thermal conductivity, which can be applied for both polycrystalline and amorphous state[28] was introduced in this study. Compared with the experimental data quantitatively, a simplified limit-case model proposed by Cahill and Pohl[29, 30] which predicts the minimal thermal conductivity κ_{min} was considered as a

solution for the explanation of experimental results. In the model, heat is considered as a random walk of damped and localized Einstein oscillators with different sizes and frequencies, which follow the density of states of the acoustic phonon model. The generalized point is that physically noncoherent but coupled atoms cannot have a lower thermal conductivity than $\kappa_{min}(T)$, with a wealth of experimental data on bulk materials and thin films cited therein to support this conclusion. The minimum thermal conductivity of an amorphous material can be written as[30]

$$\kappa_{min}^{CP}(T) = (\frac{\pi}{6})^{1/3} k_B n^{2/3} \sum_i v_i (\frac{T}{\Theta_i})^2 \int_0^{\Theta_i/T} \frac{x^3 e^x}{(e^x-1)^2} dx \quad (4\text{-}13),$$

where k_B is Boltzmann constant, n is the atom density per unit volume, v_i the speed of sound for each polarization i, and

$$\Theta_i = v_i(\hbar/k_B)(6\pi^2 n)^{1/3} \quad (4\text{-}14),$$

the Debye cutoff frequency expressed as a temperature. Considering that all NPs within films in this study as holes in the porous film, then the minimum thermal conductivity here can be adjusted to the porosity (p-CP model):

$$\kappa_{min}(T) = f(P) \cdot \kappa_{min}^{CP}(T) \quad (4\text{-}15)$$

Where f(P) is a porosity adjusted factor which has a connection with the porous film's thermal conductivity and dense film's thermal conductivity, P is porosity which can be defined as

$$P = 1 - \frac{\rho_f}{\rho_b} \quad (4\text{-}16).$$

Where ρ_f is film density, ρ_b is bulk density. As reported model for Si, porosity adjusted factor can be expressed as

$$f(P) = (1-P)^3 \quad (4\text{-}17)[31].$$

According to this calculation method, the calculated results (Figure 4.21) and experimental results are not same, however, as the comparable values the experimental results show almost same reduction tendency. Holes and NPs have different effects on thermal conduction properties, besides having the same phonon scattering on interface. Thereof p-CP model may be considered as a rough approximation for the situation of phonon scattering on NPs in this study.

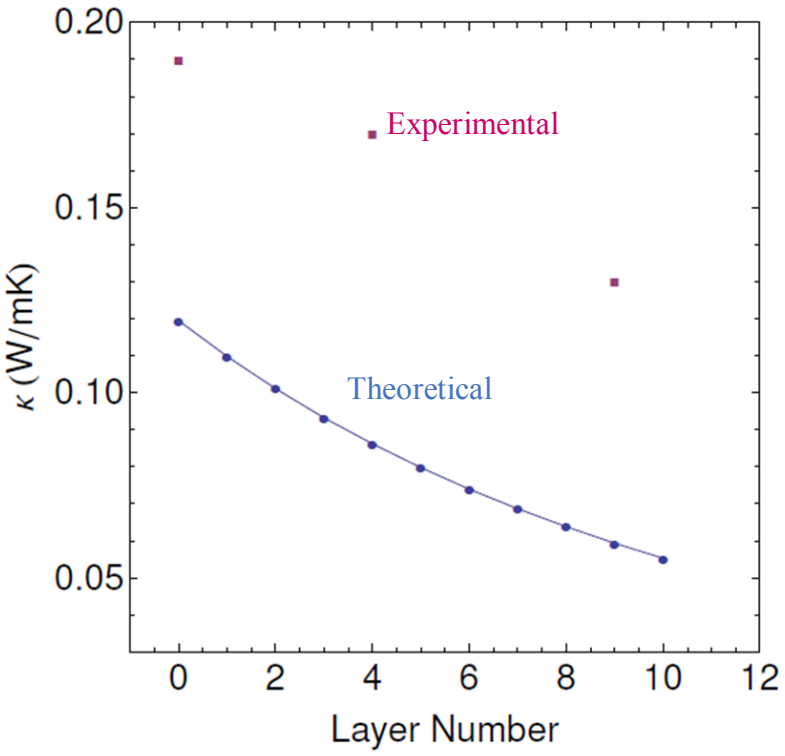

Figure 4.21 Calculated results of multi-layers structure samples with 4, 9 layers and film only without NPs in CP model.

4.4 Conclusion

In this chapter, NPs were embedded in thermoelectric material $Bi_{0.4}Te_3Sb_{1.6}$ thin film by BNP. At first, in order to evaluate the thermoelectric properties, Seebeck coefficient, electrical conductivity and thermal conductivity were measured by direct methods, Hall effect measurement and TDTR method, respectively. The electrical results agreed with the assumption of the NPs' effect in $Bi_{0.4}Te_3Sb_{1.6}$ thin film such as filtering effect and de-doping. However, the thermal conductivity results did not show an agreement with the prediction that thermal conductivity decreased due to phonon scattering, which we consider to be because the quantity and size of NPs in thin film were much weaker to affect thermal conductivity. On the contrary, the thermal conductivity increased along with NPs embedded in film because of higher thermal conductivity of NPs.

Furthermore, three dimensional structure was fabricated to amplify the phonon scattering effect of NPs. After the investigation of three dimensional nanostructure, it was confirmed that multi-layer NPs structure was fabricated successfully. And the thermal conductivity decreased as design. CP model was also introduced in this study to approximate the phonon scattering effect. Even though the approximation is rough, but amplification of phonon scattering along with increasing NPs layer has been proved.

Reference

[1] Rowe, D.M. CRC handbook of thermoelectrics. CRC, 1995.

[2] Fan, X., Zeng, G., Croke, E., et al. High cooling power density SiGe/Si microcoolers. Electronics Letters 37, 2 (2001), 126-127.

[3] Huang, I.Y., Lin, J.C., She, K.D., Li, M.C., Chen, J.H., and Kuo, J.S. Development of low-cost micro-thermoelectric coolers utilizing MEMS technology. *Sensors and Actuators A: Physical 148*, 1 (2008), 176-185.

[4] Dresselhaus, M.S., Lin, Y.M., Cronin, S.B., et al. Quantum wells and quantum wires for potential thermoelectric applications. Semiconductors and Semimetals 71, (2001), 1-121.

[5] Hicks, L.D. and Dresselhaus, M.S. Effect of quantum-well structures on the thermoelectric figure of merit. Physical Review B 47, (1993), 12731-75559.

[6] Shakouri, A. Nanoscale thermal transport and microrefrigerators on a chip. Proceedings of the IEEE 94, 8 (2006), 1613-1638.

[7] Venkatasubramanian, R., Siivola, E., Colpitts, T., and O'Quinn, B. Thin-film thermoelectric devices with high room-temperature figures of merit. Nature 413, (2001), 597-602.

[8] Harman, T.C., Taylor, P.J., Walsh, M.P., and LaForge, B.E. Quantum dot, 169 superlattice thermoelectric materials and devices. Science 297, 5590 (2002), 2229-2232.

[9] Böttner, H., Chen, G., and Venkatasubramanian, R. Aspects of thin-film superlattice thermoelectric materials, devices, and applications. MRS Bulletin 31, 03 (2006), 211-217.

[10] Bulman, G.E., Siivola, E., Shen, B., and Venkatasubramanian, R. Large external

DeltaT and cooling power densities in thin-film BiTe-superlattice thermoelectric, 166 cooling devices. Applied Physics Letters 89, (2006), 122117.

[11] Bulman, G.E., Siivola, E., Wiitala, R., Venkatasubramanian, R., Acree, M., and Ritz, N. Three-stage thin-film superlattice thermoelectric multistage microcoolers with a T max of 102 K. Journal of Electronic Materials 38, 7 (2009), 1510-1515.

[12] Venkatasubramanian, R., Siivola, E., Colpitts, T., and O'Quinn, B. Thin-film thermoelectric devices with high room-temperature figures of merit. Nature 413, (2001), 597-602.

[13] J. F. Li, W. S. Liu, L. D. Zhao, and M. Zhou, NPG Asia Mater. 2 152-158 (2010).

[14] K. Kishimoto et al Journal of Applied Physics 92, 5331 (2002).

[15] Sergey V. Fallev et al PHYSICAL REVIEW B 77, 214304 (2008).

[16] I. Yamashita, Thin Solid Film. 393, 12 (2001).

[17] R. Tsukamoto, M. Godonoga, R. Matsuyama, M. Igarashi, J. Heddle, S. Samukawa, I. Yamashita, Langmuir, 2013, 29 (41), pp 12737–12743.

[18] Keith T. Regner,Daniel P. Sellan,Zonghui Su,Cristina H. Amon,Alan J.H. McGaughey and Jonathan A. Malen, Nature Communications 4, 2013, 1640.

[19] M. Takashiri, T. Shirakawa, K. Miyazaki, H. Tsukamoto, "Fabrication and Characterization of $Bi_{0.4}Te_{3.0}Sb_{1.6}$ Thin Film by Flash Evaperation Method", Journal of Alloys and compounds, 2007. Vol. 441, pp. 246-250.

[20] N. Ghafouri: Dr. Thesis, Department of Electrical & Computer Engineering, University of Michigan, Michigan (2012).

[21] S. Tanaka: Dr. Thesis, Graduate School of Life Science and Systems Engineering, Kyushu Institute of Technology, Kyushu (2011).

[22] K. Ohara: Dr. Thesis, Graduate School of Materials Science, Nara Institute of Science

and Technology, Nara (2012).

[23] H. Fritzsche, Solid State Commun., 9 (1971), p. 1813.

[24] A. Shakouri, Annu. Rev. Mater. Res. 41 p. 399.

[25] J. Hyeong Bahk, Z. Bian, and A. Shakouri, Phys. Rev. B 87, 075204 – Published 14 February 2013.

[26] M. C. Nicolaou: Dr. Thesis, Department of Mechanical and Industrial Engineering, Northeastern University, Boston, Massachusetts (2008).

[27] N.F. Mott and H. Jones, The Theory of the Properties of Metals and Alloys, Dover Publications, New York (1958).

[28] B. Cui, L. Zeng, D. Keane, M. J. Bedzyk, D. B. Buchholz, R. P. H. Chang, X. Yu, J. Smith, T. J. Marks, Y. Xia, A. F. Facchetti, J. E. Medvedeva and M. Grayson, Thermal Conductivity Comparison of Indium Gallium Zinc Oxide Thin Films: Dependence on Temperature, Crystallinity, and Porosity, J. Phys. Chem. C 2016, 120, 7467−7475.

[29] Cahill, D. G.; Pohl, R. O. Lattice vibrations and heat transport in crystals and glasses. Annu. Rev. Phys. Chem. 1988, 39, 93−121.

[30] Cahill, D. G.; Pohl, R. O. Heat flow and lattice vibrations in glasses. Solid State Commun. 1989, 70, 927−930.

[31] Gesele, G.; Linsmeier, J.; Drach, V.; Fricke, J.; Arens-Fischer, R. Temperature-dependent thermal conductivity of porous silicon. J. Phys. D: Appl. Phys. 1997, 30, 2911.

● Chapter 5

5 Effects of FeO_x NPs in SiO_2 Thin Film

5.1 Introduction

Thermal conduction at the nanoscale is totally different to that of the macroscale. Recent improvements in theoretical calculation and experimental techniques have enabled a large number of interesting observations and understanding of thermal conduction processes at the nanoscale. In this chapter, according to the recent advances in theoretical calculations used in amorphous materials and nanoscale thermal transport studies, computational results will be compared to the experimental results. Furthermore, discussion on current understanding of the novel phenomena of nanoscale thermal conduction will be done, based on the contrast between experimental and computational results. The perspectives here challenge the understanding and controlling nanoscale thermal conduction by nanostructure.

As introduced in chapter 4, the FeO_x NPs in $Bi_{0.4}Te_{3.0}Sb_{1.6}$ thin film actually decreased the thermal conductivity when enough FeO_x NPs are embedded. This phenomenon can be explained by phonon scattering. However, according to the Wiedemann-Franz law and its relationship with thermal conduction in semiconductor materials which was discussed in chapter 1, the explanation just focused on phonon is not enough because $Bi_{0.4}Te_{3.0}Sb_{1.6}$ is a degenerate semiconductor and the electrical current in thermal conduction cannot be ignored. Furthermore, for investigation and control of heat transfer by nanostructures, effect of electric current or grain boundary should be

prevented, therefore, normal amorphous insulator material SiO_2 was selected as a thin film material to research the relationship between nanostructure and thermal conduction in thin film. On the other hand, as distribution of protein and FeO_x NPs by BNP, PEG20k-ferritin was chosen to fabricate the nano-composite structure. This is because the separation distance (SD) made by PEG20k-ferritin is an appropriate value with the mean free path in SiO_2. This is the case since PEG20k-ferritin can distribute the longest SD and that the mean free path of SiO_2 have a large distribution range (10 nm-1 μm).

The heat transport in this study should be treated in terms of the transport of phonons. As known, phonons contain two kinds of modes, acoustic and optical phonon modes. The optical phonon modes which obey the Einstein model commonly contribute little to thermal conduction which is always ignored except for at very high temperature region, due to their tiny group velocity. Therefore, the acoustic phonon modes which obey the Debye model mainly contribute to thermal conduction. Although the phonon concept was discovered around the beginning of the 20th century, the understanding and the control technologies in nanoscale thermal conduction based on phonons compared to electronic properties and optical properties were much delayed. Along with the refinement down to the nanoscale, the influence of size effects on the thermal conductivity of phonon in crystalline thin films has been widely researched topic[1-4], since a deeper knowledge of phonons in the nanoscale is necessary. Therefore, in this study, the main direction is to deepen the understanding of thermal conduction in the nanoscale region from the perspective of phonon.

All the nanostructures discussed in this chapter are composite nanostructure embedded with NPs, protein shell and hybrid structure with organic protein shell, and inorganic NPs inside protein. The simulation by molecular dynamics (MD) was employed to explain the nano-composite structure embedded with FeO_x NPs and approximation of the nanostructure embedded with organic materials by porosity model. Theoretical analysis from mean free path of phonons was also used for protein shell only and hybrid structure with organic and inorganic materials.

5.2 Multi-layers nanocomposited structure in SiO_2 Thin Film

In chapter 4, the fabrication of nanostructure such as deposition of $Bi_{0.4}Te_{3.0}Sb_{1.6}$ thin film by PLD and distribution of FeO_x NPs by BNP, have been introduced. However, in this chapter, the material of thin film has been changed into SiO_2. Instead of PLD, electron beam deposition equipment was used to deposit amorphous SiO_2 thin film at conditions of 6×10^{-4} Pa, 8 kV work voltage, and 15 mA work current. On the other hand, experimental conditions of BNP are still the same with that in chapter 2 and 4.

5.2.1 Experimental Process

In order to compare to experimental data, the total thickness of SiO_2 film is

also 200 nm. The number of FeO_x NP layers are 0, 3, and 5, respectively, due to shorten the experimental period of time. Therefore, every sample was fabricated with depositing SiO_2 5 times, and thickness is 40 nm for every time. Because it is convenient to do a comparison between each other with same fabrication conditions.

According to the principles of 3ω measurement system discussed in chapter 3, the sapphire substrates were chosen to fabricate samples. The main discussion in this study is to analyze the changes of thermal conductivity in the out-plane direction with different nanostructures through different theoretical models. The details of experiment are below:

i. 1×1 cm sapphire substrates with 3 nm thick thermal oxide layer were cleaned by acetone, methanol, and pure water. After the cleaning process, UV-Ozone treatment was done for 10 min at 115°C in order to dry substrates and remove organic impurities.

ii. SiO_2 film was deposited on substrates by TEOS-PECVD at conditions of O_2 flow rate of 300 sccm, TEOS (Tetraethyl orthosilicate) flow rate of 3 sccm, pressure of 80 Pa, temperature at 300°C and RF power at 150 W. According to the discussion in chapter 3, stability of results from 3ω measurement asks for less surface rough and selection of frequency for measurement signal, furthermore, for distribution by BNP, flat SiO_2 surface is necessary. Therefore, thickness of SiO_2 film was determined as 80 nm.

iii. After the deposition process, UV-Ozone treatment was done for 10 min at 115°C in order to make a hydrophilic surface. Then, the substrates were

put into pure water for storage until the protein distribution.

iv. For the protein distribution, at first, the samples were spin-dried. Then the solution of PEG20k-ferritin (0.05 mg/ml) with Fe core at an AA concentration of 10 mM, was dropped on the samples with 3 and 5 FeO_x NPs layers (30 μL) and held for 1 min. Next, the solution was spin-dried using the optimized spin coater conditions of 360 rpm, 60 sec; 1000 rpm, 60 sec; 5000 rpm, 30 sec.

v. All the samples were subjected to UV-Ozone treatment for 40 min at 115^{o}C in order to eliminate the organic materials completely, after the distribution process.

vi. All the samples were put inside chamber of electron beam deposition equipment, 40 nm SiO_2 thin film was deposited on FeO_x NPs directly.

vii. UV-Ozone treatment was done with all samples for 10 min at 115^{o}C in order to make hydrophilic surfaces. Then, the substrates were put into pure water for storage until the protein distribution.

viii. For the second protein distribution, the samples were spin-dried, at first. Then the PEG20k-ferritin solution which is the same as step iv was dropped on the samples with 5 FeO_x NPs layers (30 μL) and held for 1 min. Next, the solution was spin-dried using the optimized spin coater conditions as above.

ix. UV-Ozone treatment was done with all the samples for 40 min at 115^{o}C in order to eliminate the organic materials completely, after the distribution process.

x. All the samples were placed inside electron beam deposition chamber,

and 40 nm SiO_2 thin film was deposited on the FeO_x NPs directly.

xi. The UV-Ozone treatment was done with all the samples for 10 min at 115°C in order to make hydrophilic surfaces. Then, the substrates were put into pure water to store until protein distribution.

xii. For the third time of protein distribution, the samples were spin-dried at first. Then, the PEG20k-ferritin solution which is same as step iv. was dropped on the samples of 3 and 5 FeO_x NPs layers (30 μL) and held for 1 min. Next, the solution was spin-dried using the optimized spin coater conditions as above.

xiii. The UV-Ozone treatment was done with all samples for 40 min at 115°C in order to eliminate the organic materials completely, after the distribution process.

xiv. All the samples were put inside chamber of electron beam deposition equipment, 40 nm SiO_2 thin film was deposited on FeO_x NPs directly.

xv. The UV-Ozone treatment was done with all samples for 10 min at 115°C in order to make hydrophilic surfaces. Then, the substrates were put into pure water to store until protein distribution.

xvi. For the fourth time of protein distribution, the samples were spin-dried at first. Then the PEG20k-ferritin solution which is same as step iv. was dropped on the sample of 5 FeO_x NPs layers (30 μL) and held for 1 min. Next, the solution was spin-dried using the optimized spin coater conditions as above.

xvii. The UV-Ozone treatment was done with all samples for 40 min at 115°C in order to eliminate the organic materials completely, after the

distribution process.

xviii. The samples were put inside chamber of electron beam deposition equipment, 40 nm SiO_2 thin film was deposited on FeO_x NPs directly.

xix. The UV-Ozone treatment was done with all samples for 10 min at 115ºC in order to make hydrophilic surfaces. Then, the substrates were put into pure water to store until protein distribution.

xx. For the fifth time of protein distribution, the samples were spin-dried at first. Then the PEG20k-ferritin solution which is same as step iv. was dropped on the samples of 3 and 5 FeO_x NPs layers (30 μL) and held for 1 min. Next, the solution was spin-dried using the optimized spin coater conditions as above.

xxi. The UV-Ozone treatment was done with all samples for 40 min at 115ºC in order to eliminate the organic materials completely, after the distribution process.

xxii. All the samples were put inside chamber of electron beam deposition equipment, 40 nm SiO_2 thin film was deposited on FeO_x NPs directly.

xxiii. Three kinds of samples, which are SiO_2 film only and SiO_2 film concluding 3 and 5 FeO_x NPs layers, were fabricated (Figure 5.1). All these samples put onto metal mask of 3ω measurement pattern, about 430 nm thick Al was deposited by electron beam deposition equipment.

xxiv. Finally, all the samples were measured by 3ω measurement system which was set up by ourselves, in the out-plane direction (chapter 3).

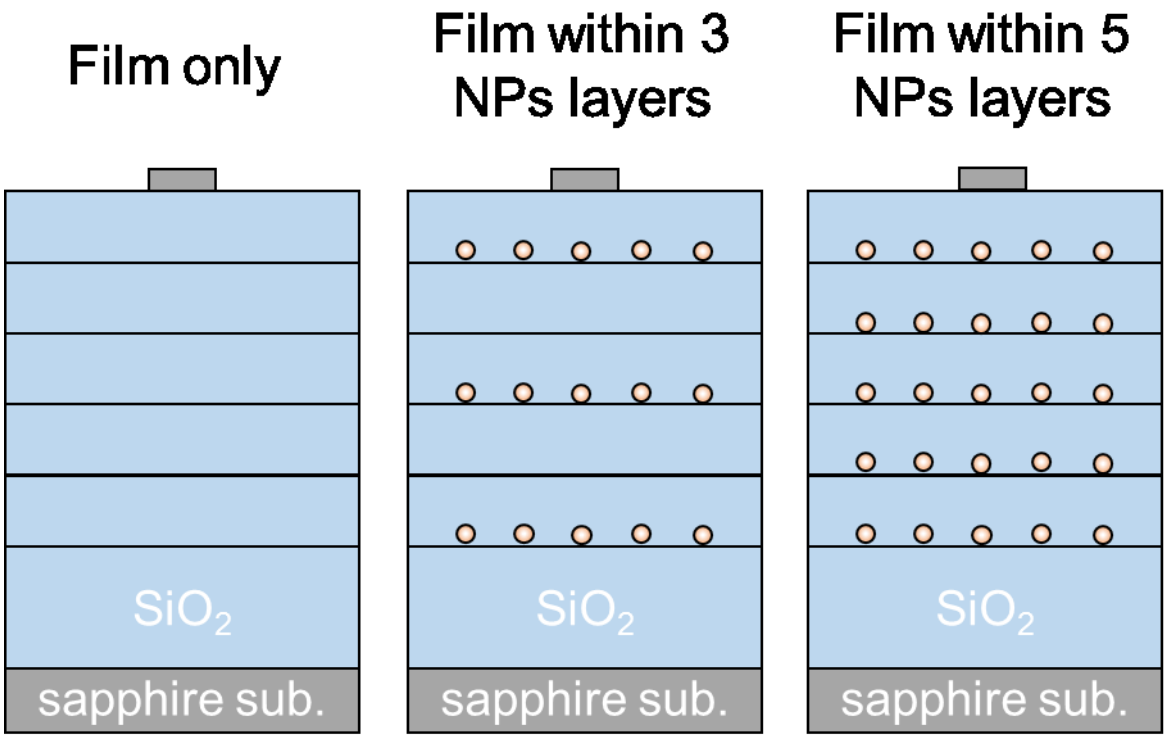

Figure 5.1 Schematic figure of nanocomposite samples' structure.

5.2.2 Results and Discussion by MD simulation of Perturbation Theory

The 3ω measurement results (Figure 5.2) showed that thermal conductivity for samples with only SiO_2 film, SiO_2 film concluding 3 and 5 NPs layers increased along with increase of NPs layers, which indicate that NPs increase the thermal conductivity. Every error range was made by six samples. And this result is opposite to the results in $Bi_{0.4}Te_{3.0}Sb_{1.6}$ thin film in chapter 4. However, the properties of thermal conduction in these two situations are totally different from each other. For instance, the mean free path of phonons or ratio of contribution of thermal conductivity for electrons and phonons are different. Therefore, even with same nanostructure, $Bi_{0.4}Te_{3.0}Sb_{1.6}$ and SiO_2

thin film should have different NP effects.

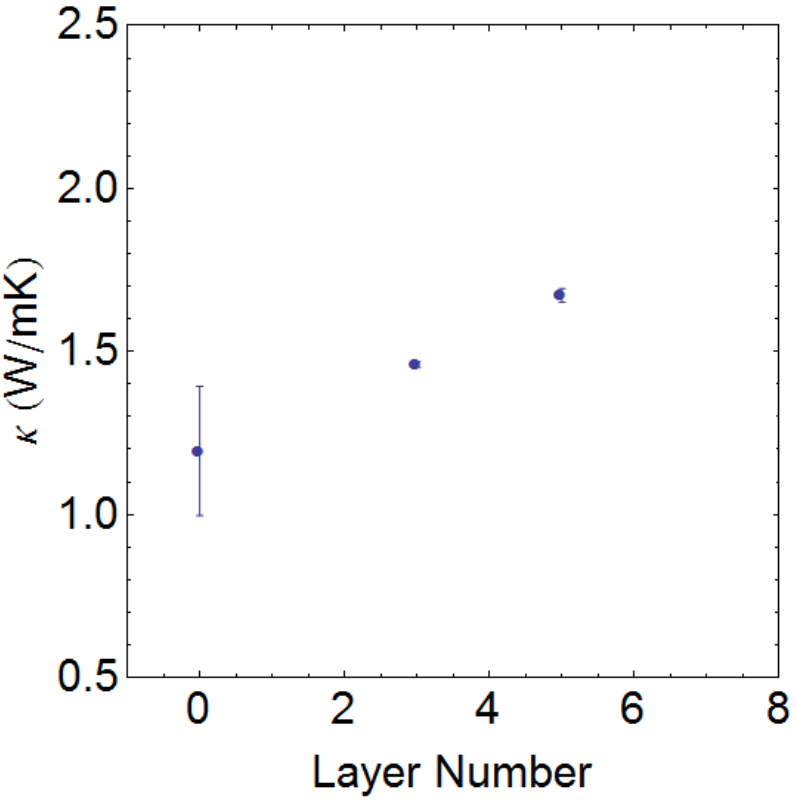

Figure 5.2 Results of 3ω measurement for samples SiO_2 film only, SiO_2 film concluding 3 and 5 NPs layers.

In order to explain the phenomenon, MD simulation was employed to analyze the nanocomposite structures. Recently, MD simulations are becoming very important tools to analyze properties of thermal conduction by phonons. Through MD simulations, more complex potential functions, not just simple pair potentials such as Morse types or Lennard-Jones, are available[5, 6]. For instance, it was possible to do calculation with many-body potentials for complex solids, interfaces and molecules[7, 8]. Furthermore, the first principles calculations which are based on non-empirical potentials, have turned to widely be usable, such as application for calculation of

phonon transport properties[9-11]. Along with the development of synthesis and characterization of materials at the nanoscale, it is becoming more and more important to understand and control thermal conduction of interfaces or nanostructures[12]. At the nanoscale, thermal conduction is different from the macroscale, especially in situations where the scale is shorter than the phonon mean free path. The non-equilibrium molecular dynamics (NEMD) simulations offer a method to calculate these properties directly. On the other hand, equilibrium molecular dynamics (EMD) simulations are widely used to calculate bulk thermal conductivity through the Green-Kubo (GK) formula and the linear response theory[13-15]. The common method of using NEMD to calculate thermal conductivity includes putting a perturbation into the system and detecting the response from the system. Although the perturbation can be applied in different ways, the most common choice is the steady temperature gradient or heat flux, through which the thermal conductivity of system can be derived directly. Another important application of the perturbation is to put it onto the Hamiltonian of the system. Nevertheless, NEMD methods using perturbation have much faster convergence compared to the GK method.

For MD simulations, there are many software packages such as LAMMPS[16], GROMACS[17], DL_POLY[18] and NAMD[19], which enable even non-experts who do not understand code well, to easily do MD simulations and calculate various properties. However, in thermal conductivity calculation by MD, very small technical error can cause mistakes in the calculations[20-23]. All the MD methods have their advantages and disadvantages. Therefore, it is

important to understand the limited conditions of each method. In this study, SCIGRESS which was made by FUJITSU Co., was employed to simulate thermal conductivity in non-equilibrium molecular dynamics (MD-ME module). The method in simulation is called perturbation method in which applying perturbation on Hamiltonian leads to a linear response. And the gradient of the line is the value of thermal conductivity. Fe_2O_3 and Al_2O_3 also have the same crystal structure (hR30) and kinds of potentials (Born-Mayer-Huggins), and iron oxide NPs was considered as Fe_2O_3 in the simulation. Therefore, Al_2O_3 was utilized as the NPs' material to approximate Fe_2O_3 NPs, due to a lack of potential packages for Fe_2O_3. Furthermore, for huge calculation with real size of models, one tenth size was used to model the subunit of nanostructure (Figure 5.3), because there are no significant change with diminishing size in a certain range, once the scale is smaller than limit value. The stability of subunit will decrease due to perturbation. The potential model which was utilized to MD simulation, is CMAS94 composed of pairwise additive interaction of Coulomb, van der Waals force, and repulsive interactions, in Born Mayer Huggins (BMH) type potential[24]. And BMH potential can be expressed as

$$\varphi_{ij}(r) = \frac{Z_i Z_j e^2}{4\pi\varepsilon_0 r} + A_{ij} b e^{\frac{\sigma_i+\sigma_j-r}{\rho}} - \frac{C_i}{r^6} - \frac{D_i}{r^8} \quad (5\text{-}1),$$

where the first item is a Coulomb item, the second item is repulsive interactions item, the third item is the instantaneous dipole–induced dipole forces item, the fifth item is instantaneous quadrupole–induced dipole forces item; and ε_0 is dielectric constant of vacuum, Z_i and Z_j are valence of ion, A_{ij} is Pauling factor, b is parameter to express strength of repulsive force, σ_i is

parameter to express size of ion, ρ is softness parameter, C_{ij} is parameter of dipole–induced dipole interaction, D_{ij} is parameter of quadrupole–induced dipole interaction.

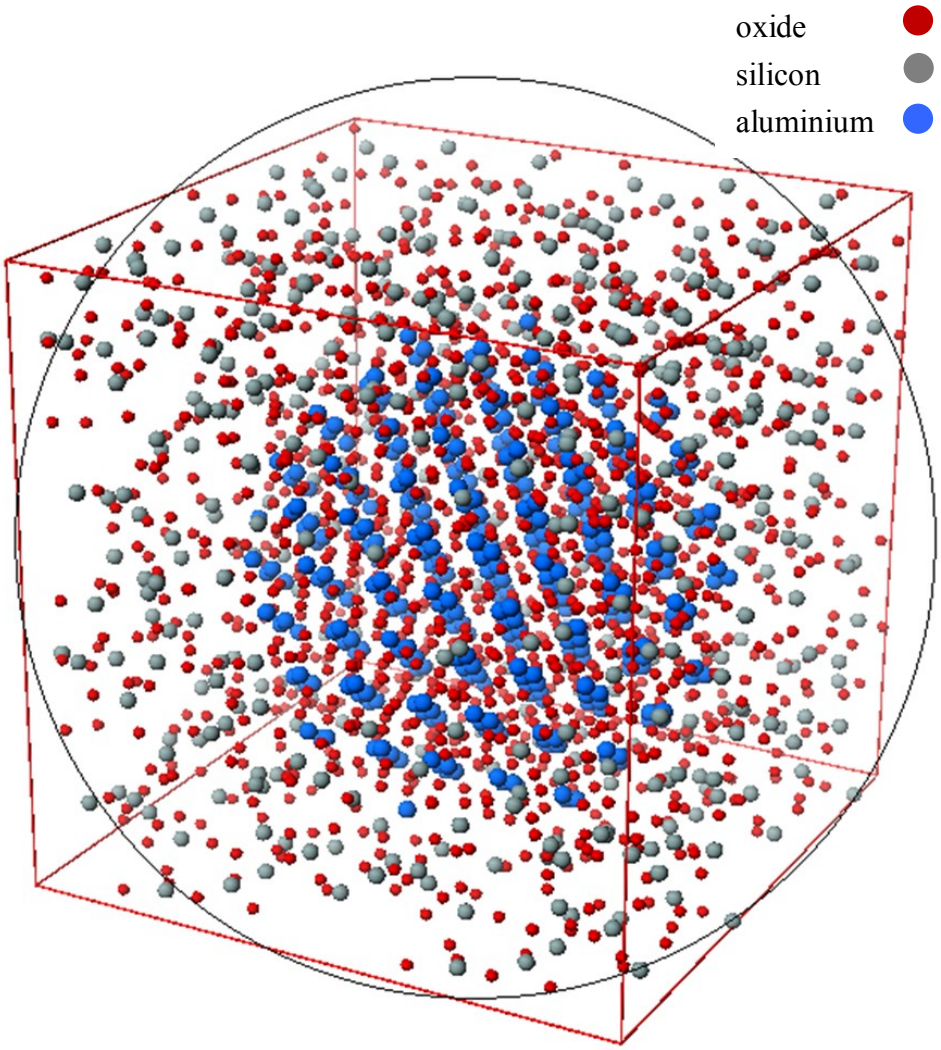

Figure 5.3 Image of subunit nanostructure for simulation model in SCIGRESS.

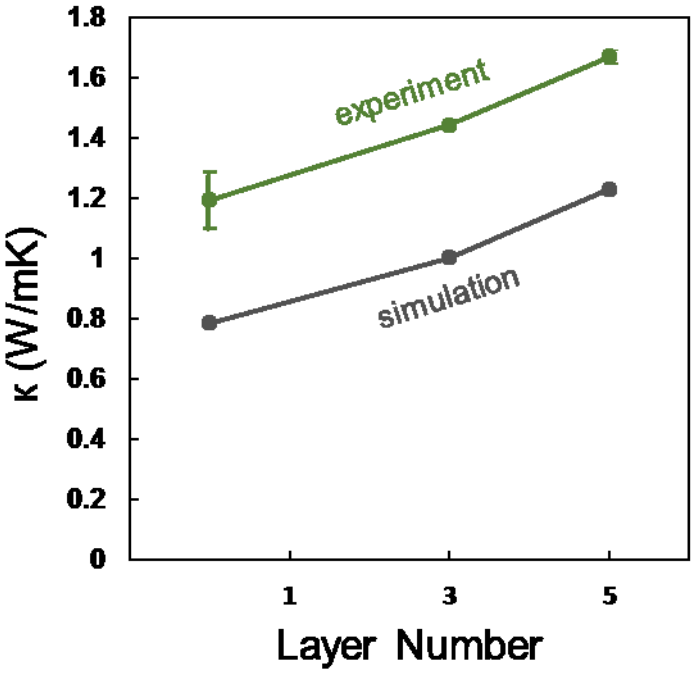

Figure 5.4 Comparison between experimental results and results of simulation for samples SiO_2 film only, SiO_2 film concluding 3 and 5 NPs layers.

Through the comparison between the MD simulation results and the experimental results for SiO_2 film only samples, SiO_2 film with 3 and 5 NPs layers (Figure 5.4), the gradient of thermal conductivity change with layer number increase is almost the same. This observation was made even though there is a shift between results of MD simulation and experiment due to errors in MD simulation model or 3ω measurement. Therefore, the calculations in this MD simulation should be considered as an ideal verification and explanation. The simple explanation is that thermal conductivity of NPs is more than 20 times higher than the film. Therefore, even though phonons scattering occurred, the whole nanocomposite structure still caused a raise of thermal conductivity. Furthermore, the

thermal conductivity will increase along with NPs layers increase.

5.3 Nano Hybrid structure concluding Multi-layers PEG20000-ferritin with and without core (apo-ferritin) in SiO_2 Film

Nanocomposite structure embedded with NPs has been analyzed and the results show that thermal conductivity increased. The samples include only inorganic materials. Therefore, an interesting idea was considered, that if the organic materials left with NPs to fabricate a hybrid structure or protein shell without inorganic NPs, consequent results are really expected. For instance, higher effect of phonon scattering will occur, that causes a desirable decrease of thermal conductivity. As a novel idea, a hybrid structure with organic and inorganic materials has already been theoretically demonstrated and realized for devices[25, 26]. In the future, hybrid of organic and inorganic materials will play a major role in the development of advanced functional nanomaterials.

In this section, hybrid organic-inorganic materials are fabricated and analyzed in theory. For the hybrid structure, multi-layers of PEG20k-ferritin with and without NPs core in SiO_2 thin film as hybrid structure will be fabricated and discussed.

5.3.1 Experimental Process

The fabrication processes for hybrid structure are almost the same with experimental processes of nanocomposite structure in section 5.2.1, only without the organic materials' elimination processes by UV/Ozone for 40 min since the protein shells should remain. Nanostructure with organic protein shell is a more complex structure, but serial processes become simpler due to 40 min that is saved in every layer fabrication cycle.

As a test experiment, samples with one PEG20k-ferritin layer were fabricated first (Figure 5.5). After the cleaning process and SiO_2 thin film deposition, SEM images were taken after the bio nano process to observe the distribution of PEG20k-ferritin. As the SEM images (Figure 5.6) showed, NPs inside PEG20k-ferritin distributed uniformly, which indicate proteins used this time are the same as before.

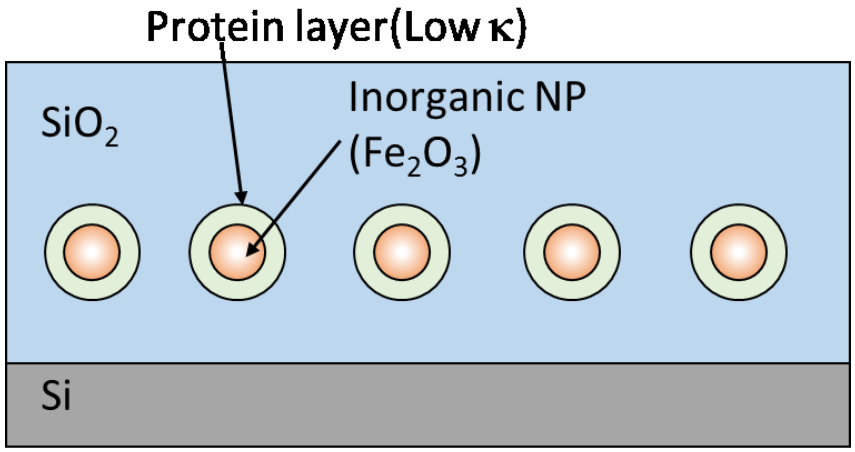

Figure 5.5 Schematic figure for one layer of PEG20k-ferritin with FeO_x NPs core.

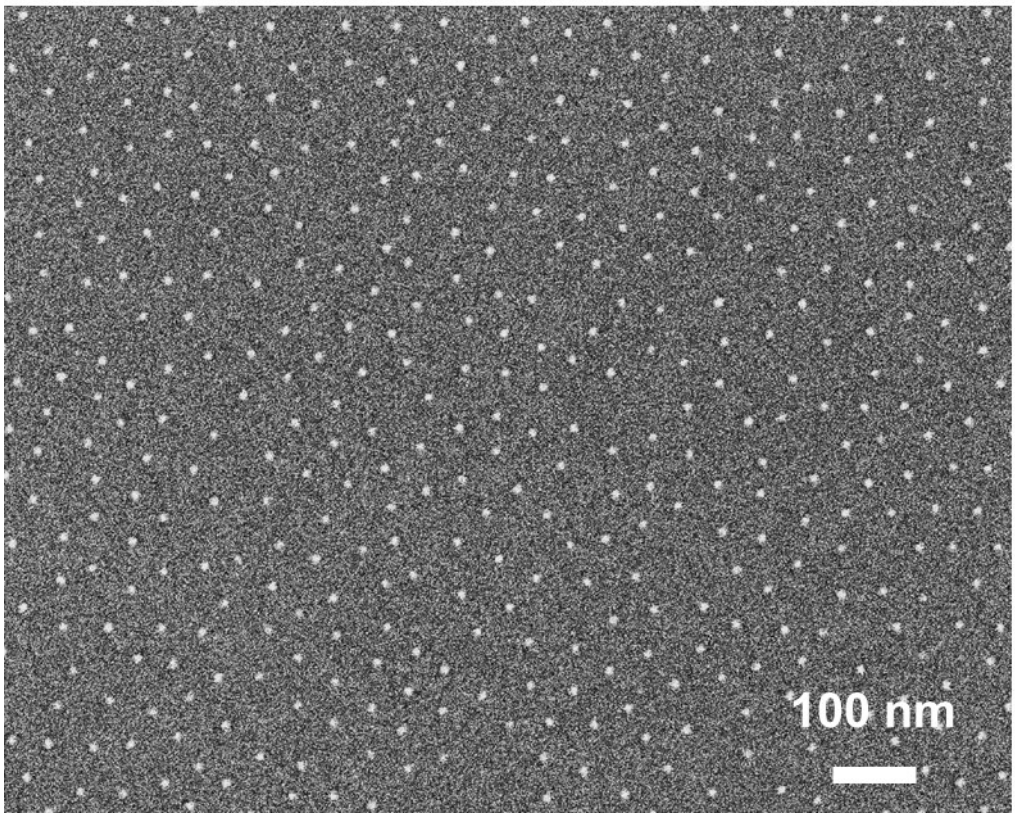

Figure 5.6 SEM image for sample of one PEG20k-ferritin layer with FeO_x NPs core.

After the fabrication of one layer samples, cross-sectional TEM images were taken to confirm the nanostructure and film properties. According to the cross-sectional TEM images (Figure 5.6), PEG20k-ferritins, which were embedded inside the SiO2 thin film, still kept structure. In the images, the black central part is NPs of iron oxide, and white shell part is considered as protein and PEG.

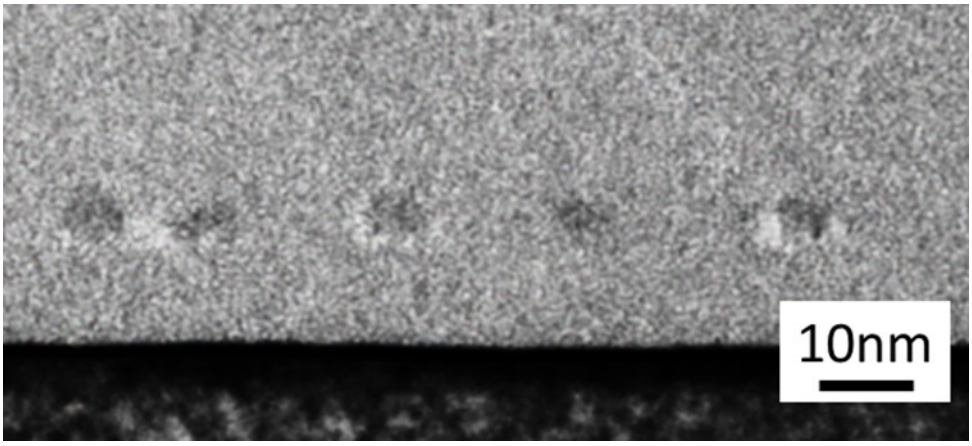

Figure 5.7 Cross-sectional TEM images for one layer of PEG20k-ferritin with FeO_x NPs core.

As a final evaluation step for the experiment, electrode patterns for 3ω measurement were deposited by electron beam deposition equipment on one layer sample. The samples were then measured by 3ω measurement system in the out-plane direction (Figure 5.8). According to the thermal conductivity results (Table 5.1), the thermal conductivity reduced about 7% due to PEG20k-ferritin embedded which is considered as the effect of phonon scattering by the shell of the organic materials.

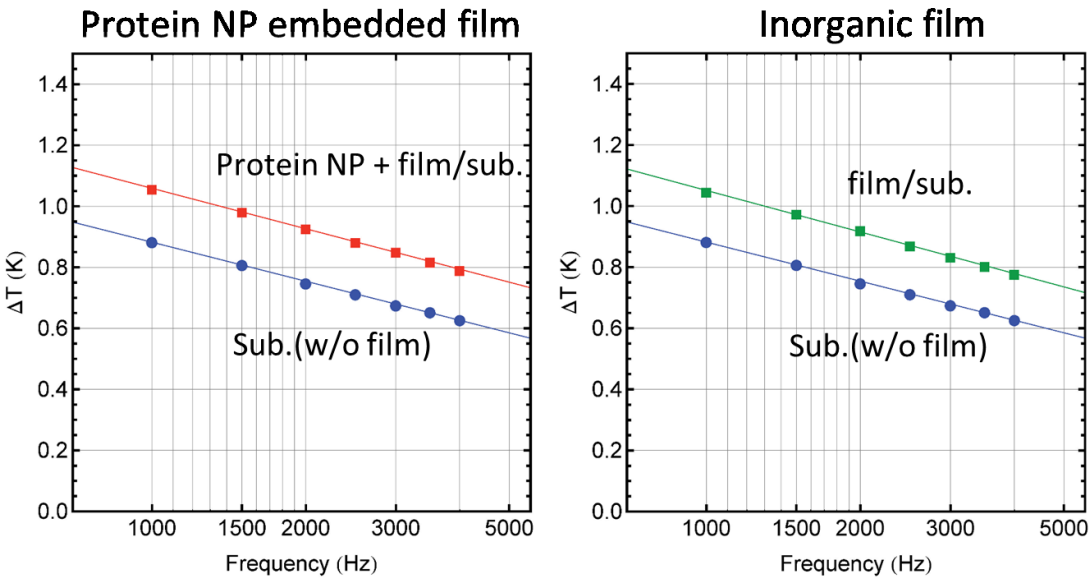

Figure 5.8 3ω measurement results for comparison between one PEG20k-ferritin (with FeO_x core) layer sample and thin film only sample.

Table 5.1 3ω measurement results for contrast between one PEG20k-ferritin (with FeO_x core) layer sample and thin film only sample.

Samples	**Thermal conductivity (W/mK)**
Film only	1.41
Protein embedded film	1.32

However, the decreased value is too small to validate the reduction, comparing to error region of 3ω measurement system. Therefore, multi-layers nanostructure of PEG20k-ferritin (with FeO_x core) were fabricated following the processes in the nanocomposite structure with NPs except for

the elimination of protein shell by UV/Ozone (Figure 5.9). Furthermore, PEG20k-ferritin without NPs core (apo-ferritin) were also utilized to fabricated nanostructure samples with same processes due to investigate effects of core inside (Figure 5.10). However, the numbers of apo-ferritin layers are different from the samples concluding NPs.

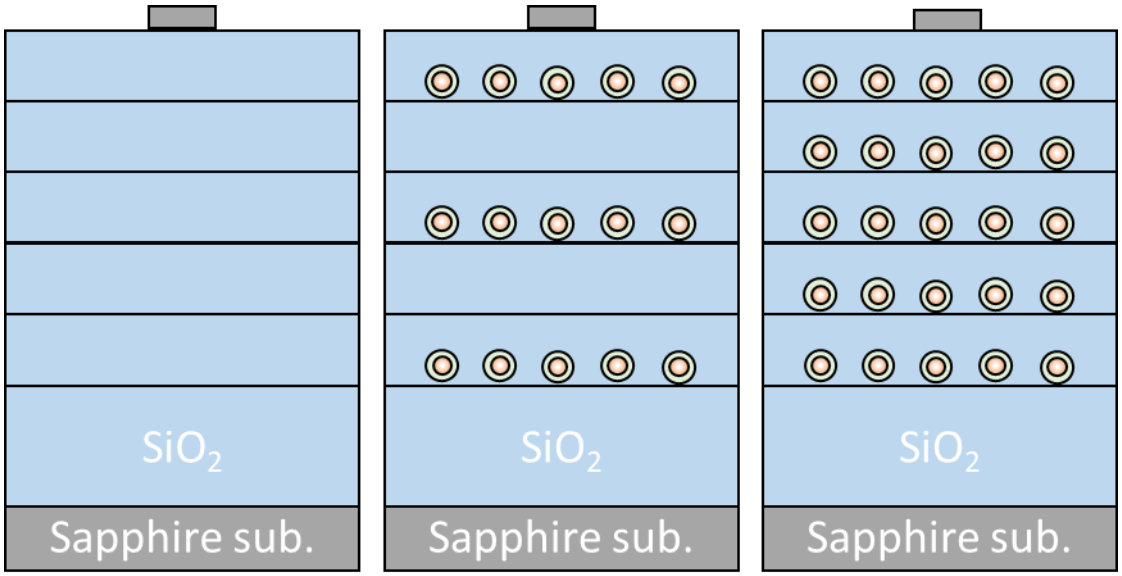

Figure 5.9 Schematic figure of multi-layers PEG20k-ferritin samples' structure.

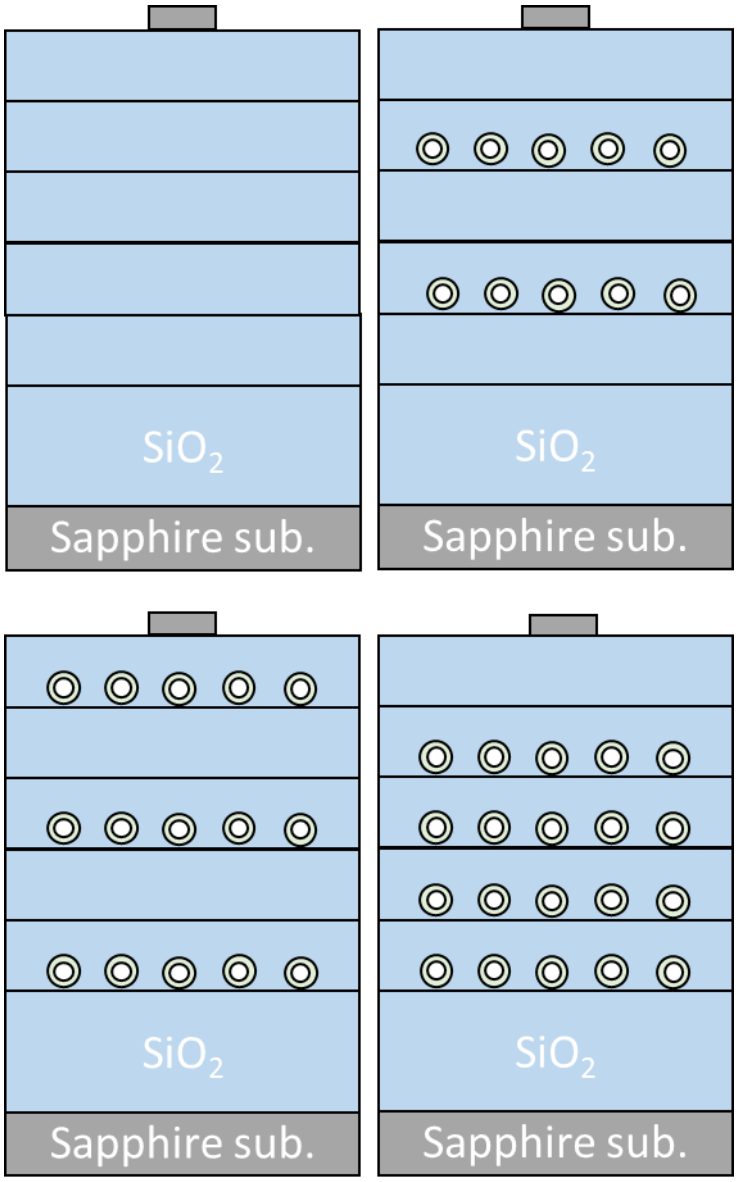

Figure 5.10 Schematic figure of multi-layers apo-ferritin samples' structure.

Following the same evaluation methods, cross-sectional TEM images were taken to confirm the multi-layered nanostructure. According to the cross-sectional TEM images (Figure 5.11), multi-layered nanostructure was fabricated successfully. Furthermore, the dots in the SiO_2 film show the white shell and black core which were assumed as protein ferritin with PEG and

FeO_x NPs, respectively. Furthermore, the NPs were confirmed by Fe elements' EELS (Electron Energy Loss Spectroscopy) mapping and the images showed that FeO_x cores still exist inside PEG20k-ferritin without diffusion (Figure 5.12). Namely, the hybrid structure which contains PEG20k-ferritin shell and NPs inside, is stable after the fabrication processes. There are some damage on the upper layer of protein shells due to milling process for fabrication of cross-sectional TEM samples. For another consideration, the shape and structure of protein shell should change due to denaturation after drying process and SiO_2 deposition. However, the organic materials which were left from PEG-ferritin still enclose the NPs and contribute to phonon scattering.

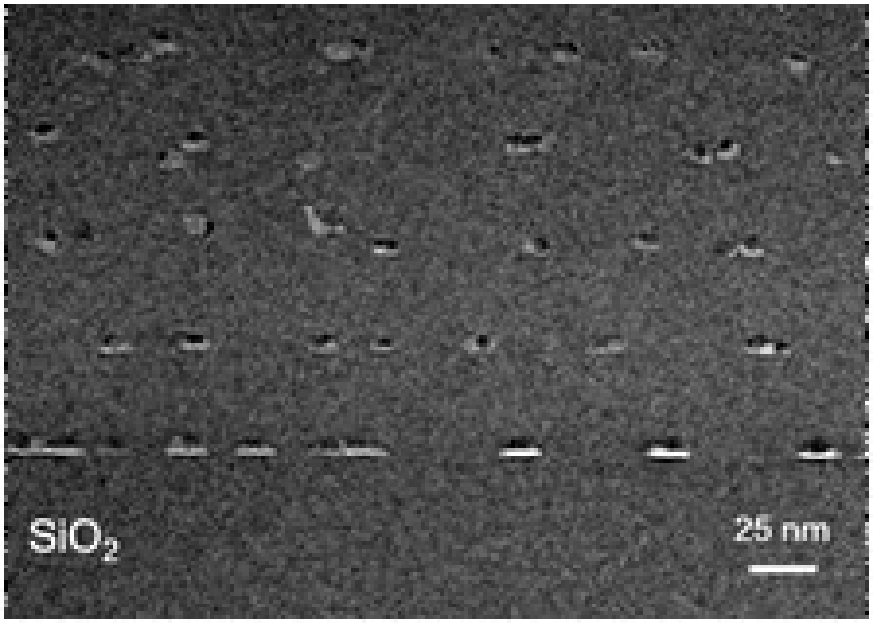

Figure 5.11 TEM images for sample of hybrid nanostructure with 5 layers FeO_x NPs of PEG-ferritin.

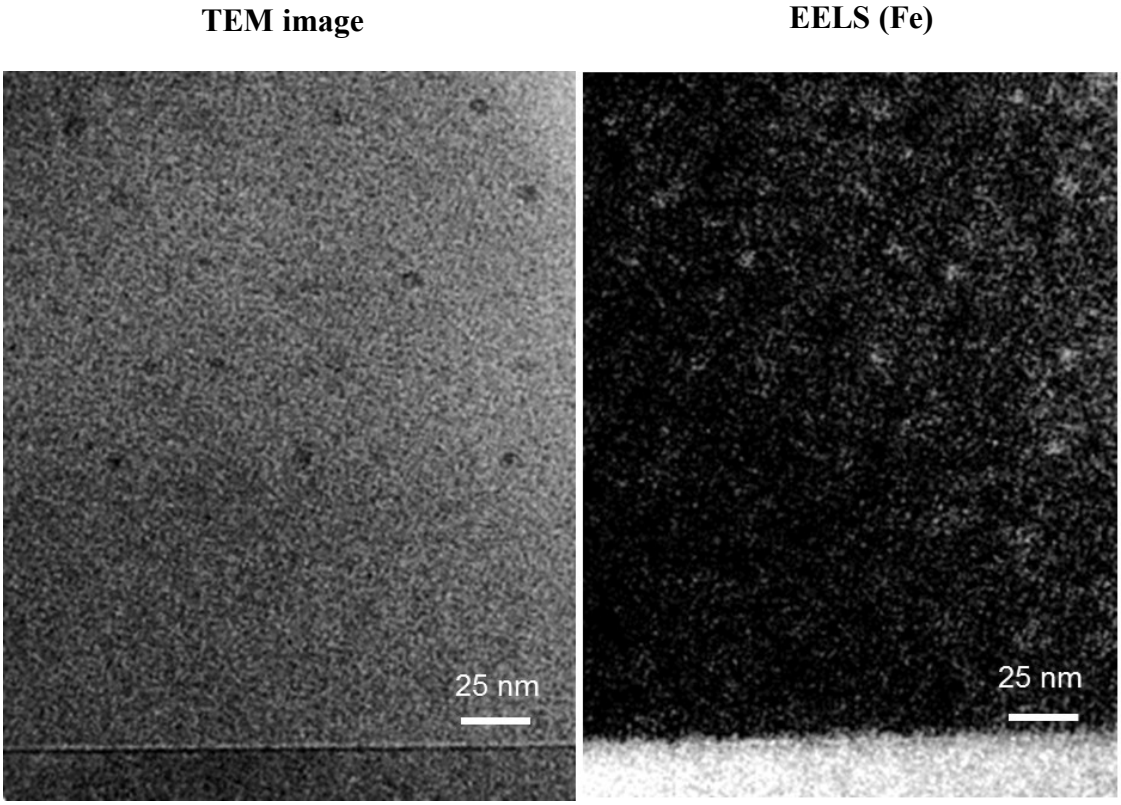

Figure 5.12 EELS mapping for multi-layers FeO_x NPs within PEG20k-ferritin by TEM.

5.3.2 Theoretical Analysis for Thermal Conductivity in Amorphous SiO_2 Film

Following the confirmation of nanostructure, samples were measured by 3ω measurement system. From the results of 3ω measurement in the out-plane direction (Figure 5.13), the thermal conductivity actually decreased along with increase in the number of layers. Even though only embedded NPs cause an increase of thermal conductivity, NPs wrapped by PEG20k-

ferritin can actually depress the thermal conductivity. We considered that the organic materials shell have more effect on the phonon scattering in amorphous SiO_2 thin film. However, the assumption needs theoretical support. Therefore, the calculations of thermal conductivity based on phonon properties were carried out.

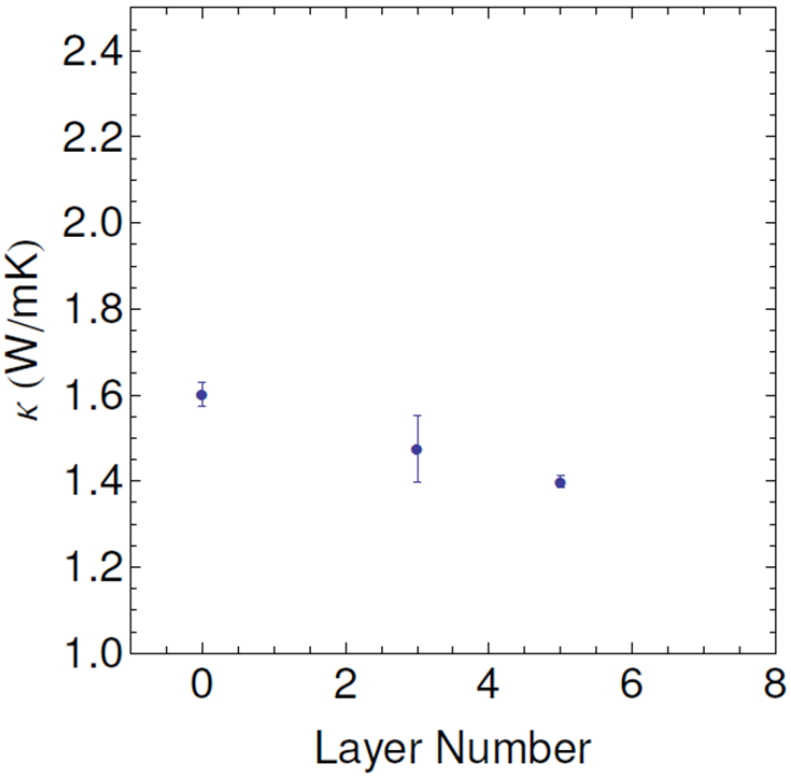

Figure 5.13 3ω measurement results of 3, 5 PEG20k-ferritin layers samples and thin film only sample.

According to phonon modes divided in disordered solids (e.g., alloys, amorphous materials) which can be classified as propagated phonons (propagating and delocalized, i.e., phonon like), diffusions (non-propagating and delocalized), and located phonons (non-propagating and localized) [27-29],

the relations of thermal conductivity by those kinds phonons can be expressed as

$$\kappa_p = \kappa_{pr} + \kappa_{AF} \quad (5\text{-}2),$$

where κ_p is thermal conductivity contributed from phonons, κ_{pr} is thermal conductivity contributed from propagating phonon modes[30] and κ_{AF} is thermal conductivity contributed from non-propagating phonon modes predicted by the AF theory[31]. For propagating phonon modes, thermal conductivity can be written as[32, 33]:

$$\kappa_{pr} = \frac{1}{V}\int_0^{\omega_{cut}} DOS(\omega)C(\omega)D_{pr}(\omega)\, d\omega \quad (5\text{-}3),$$

where V is the system volume, ω_{cut} is the maximum frequency of propagating phonon modes, DOS(ω) is the phonons' vibrational density of states (DOS), C(ω) is the phonon mode specific heat which is divided by phonon frequencies, and $D_{pr}(\omega)$ is the phonon mode diffusivity. And DOS can be calculated by

$$\mathrm{DOS}(\omega) = \frac{3V\omega^2}{2\pi^2 \upsilon_s^3} \quad (5\text{-}4),$$

where υ_s is an appropriate sound speed. The specific heat can be calculated by the full quantum formula

$$\mathrm{C}(\omega) = \mathrm{k}_B\left[\frac{\hbar\omega/2\mathrm{k}_B T}{\sinh(\hbar\omega/2\mathrm{k}_B T)}\right]^2 \quad (5\text{-}5),$$

where $\hbar$ is the Planck constant divided by 2π. The propagating phonon modes' diffusivity can be expressed as

$$\mathrm{D}_{\mathrm{pr}}(\omega) = \frac{1}{3}\upsilon_s^2\tau(\omega) = \frac{1}{3}\upsilon_s l(\omega) \quad (5\text{-}6),$$

because of $l(\omega) = \upsilon_s\tau(\omega)$ (5-7),

where $\tau(\omega)$ is the lifetime of frequency-dependent phonon mode and l(ω) is the MFP of phonon. Furthermore, the lifetimes can be modeled as

$$\tau(\omega) = \mathrm{B}\omega^{-n} \quad (5\text{-}8),$$

where *B* is a constant coefficient that incorporates the effect of temperature. In amorphous materials, the scaling exponent *n* has been tested by experimental and numerical methods, two and four are found as values of *n*[33-43]. A value of two corresponds to anharmonic scattering[44], while a value of four corresponds to Rayleigh type scattering by point defects[45]. Through the calculation test, the value four for n is much smaller than a value of two in this study. Therefore, the calculations were done without a value of four which was approximated as zero and ignored. Another operation that was done is the transformation of the formula 5-3 from the expression of frequency to the expression of MFP, according to the formula 5-7. Thereby, the formula 5-2 can be written as

$$\kappa_p(l^*) = \int_{l_{cut}}^{l^*} \kappa(l)\mathrm{d}l + \kappa_{AF} \quad (5\text{-}9),$$

where l^* is the maximum MFP and l_{cut} is the MFP at the cutoff frequency which can be calculated from the maximum frequency of propagating phonon modes by formula 5-7. In this study, it was assumed that the layers of PEG20k-ferritin can cut MFP off., Namely, the distance between layers was chosen as maximum MFP (l^*). And κ_{AF} is used as the value of 1.4±0.1 W/mK[27]. Thereby the calculations were carried out, the results of calculation and experiment showed that the gradient of thermal conductivity's change almost the same in experiment and calculation. However, there is a value shift between theoretical and experimental data which is considered as

acceptable error region due to error bar in experiment or theoretical model. Therefore, the theoretical model can explain the experimental phenomena perfectly.

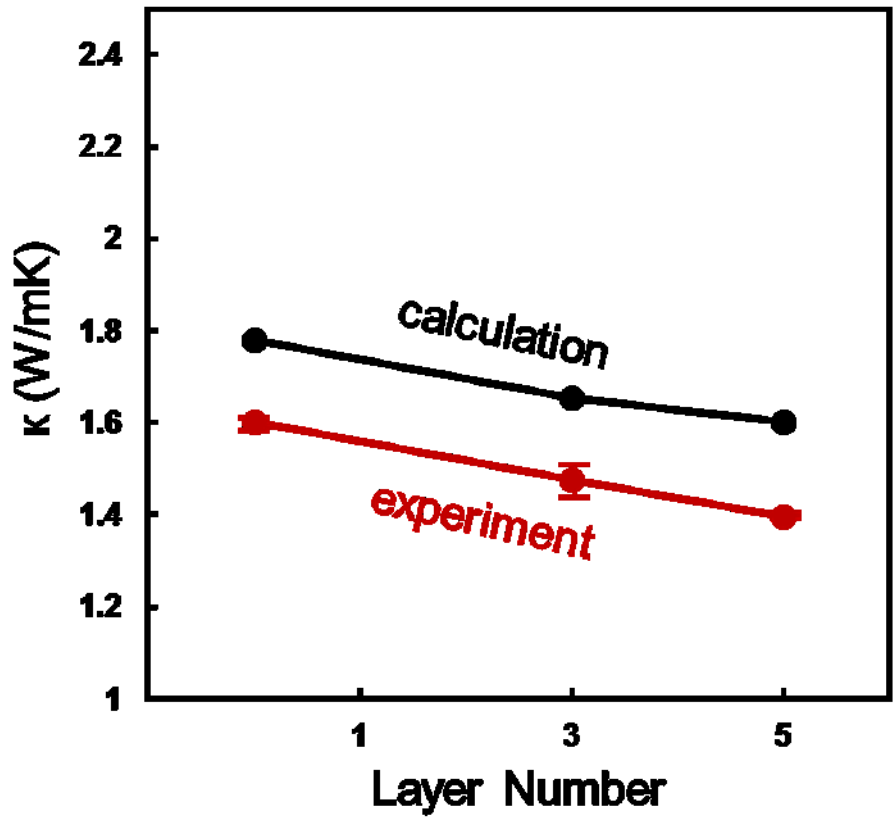

Figure 5.14 Theoretical calculation and experiment results of 3, 5 PEG20k-ferritin layers samples and thin film only sample.

Furthermore, the results for apo-ferritin also showed a decrease of thermal conductivity along with protein layers increased (Figure 5.15). However, the data is not stable in 3ω measurement and error ranges are wide. Furthermore, the cross-sectional TEM images are also taken, but there are no clear

nanostructure that can be observed suggesting that the apo-ferritin shrank or were even broken after film deposition. Therefore, the data could not show the properties of multi-layered structure.

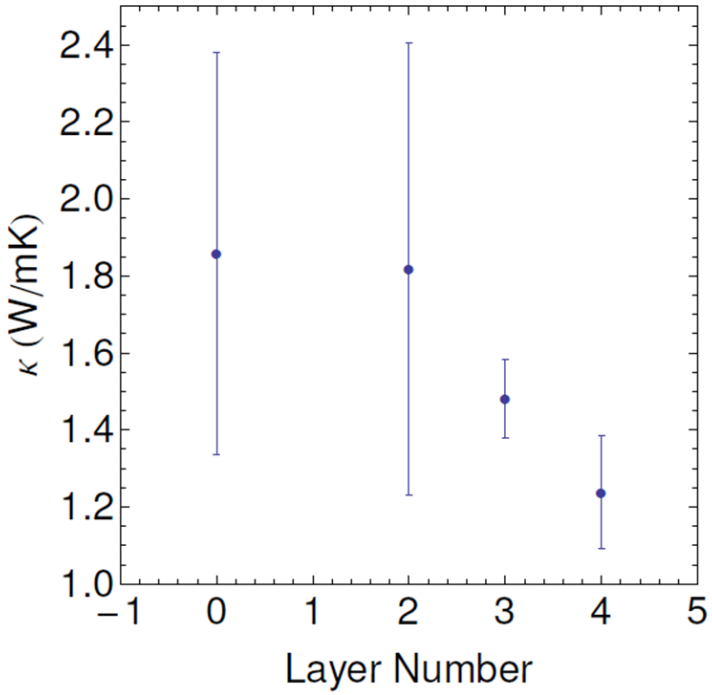

Figure 5.15 3ω measurement results of 2, 3, 4 apo-ferritin layers samples and thin film only sample.

5.4 Conclusion

In this chapter, the change of thermal conductivity in amorphous SiO_2 thin film was discussed with employment of nanostructures. Compared to the nanostructure in chapter 4, amorphous SiO_2 could avoid the phonon

scattering at the grain boundary and thermal conductivity contribution from electron. Furthermore, nanocomposite structure of multi-layers NPs and hybrid structure of inorganic FeO_x NPs and organic PEG20k-ferritin shell were utilized to control the change of thermal conductivity (Δκ). From the results (Figure 5.16), the existence of the organic material shells could lead to the tendency of thermal conductivity to change.

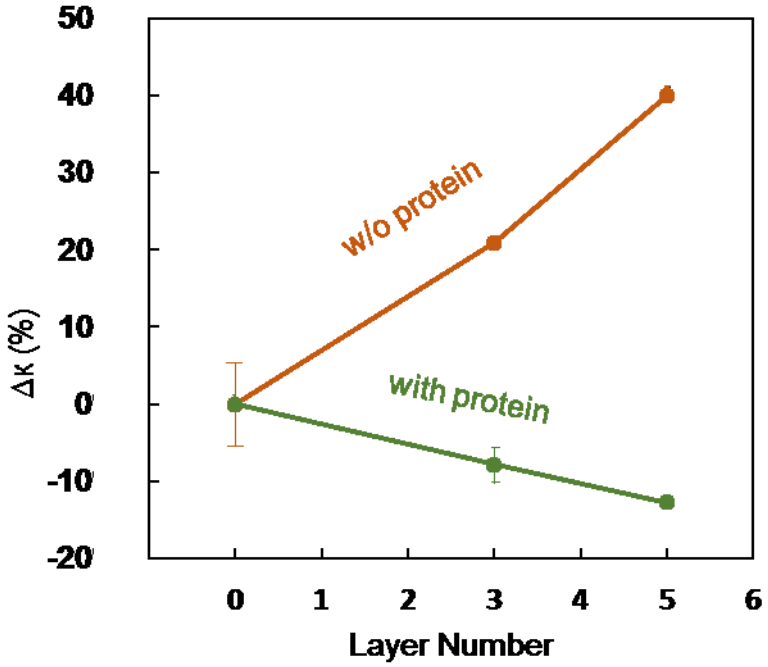

Figure 5.16 Contrast between nanocomposite structure samples and hybrid structure samples with of 3, 5 NPs layers and 3, 5 PEG20k-ferritin layers, respectively.

For FeO_x NPs, there should be phonon scattering effect on the interface between NPs and thin film. However, because material of NPs have much higher thermal conductivity than the thin film material, the thermal conductivity increased along with NPs embedded in thin film.

On the other hand, without the elimination processes of protein shell, nevertheless higher thermal conductivity NPs still exist inside protein shell, but the thermal conductivity actually decreased due to strong phonon scattering effect on the interface between organic and inorganic materials. Namely, organic protein shell can efficiently scatter phonon from inside or outside, or even cut off the MFP of phonon. All these assumptions had been proven by MD simulation and calculation with different phonon modes for thermal conductivity. Therefore, the nanostructures designed were fabricated successfully, and thermal conductivity in materials embedded in nanostructures were reduced or raised. And the techniques of fabricating nanostructures in this chapter exhibited a novel method to control thermal conduction in the nanoscale. That should have great applications for not only improvement of thermoelectric materials but also common materials science, as refinement is being made in the nanoscale or beyond.

Reference

[1] G. Chen, Nanoscale Energy Transport and Conversion: A Parallel Treatment of Electrons, Molecules, Phonons, and Photons (Oxford University Press, New York, 2005).

[2] D. Li, Y. Wu, P. Kim, L. Shi, P. Yang, and A. Majumdar, Appl. Phys. Lett. 83, 2934 (2003).

[3] A. M. Marconnet, M. Asheghi, and K. E. Goodson, J. Heat Transfer 135, 061601 (2013).

[4] H. Zhang, C. Hua, D. Ding, and A. J.Minnich, Sci. Rep. 5, 9121 (2015). I. Yamashita, Thin Solid Film. 393, 12 (2001).

[5] P.M. Morse, Diatomic Molecules according to the wave mechanics II. Vibrational levels, Phys. Rev., 34 (1929) 57.

[6] J.E. Lennard-Jones, On the Determination of Molecular Fields, Proc. R. Soc. Lond. A, 106 (1924) 463.

[7] A.J.H. McGaughey, M. Kaviany, Phonon Transport in Molecular Dynamics Simulations: Formulation and Thermal Conductivity, Advances in Heat Transfer, 39 (2006) 169.

[8] S. Maruyama, Molecular dynamics method for microscale heat transfer, Adv. Numer. Heat Transfer, 2 (2000) 189.

[9] K. Esfarjani, G. Chen, H.T. Stokes, Heat transport in silicon from first-principles calculations, Phys. Rev. B, 84 (2011) 085204.

[10] D.A. Broido, M. Malorny, G. Birner, N. Mingo, D.A. Stewart, Intrinsic lattice thermal conductivity of semiconductors from first principles, Appl. Phys. Lett., 91 (2007) 231922.

[11] J. Shiomi, K. Esfarjani, G. Chen, Thermal conductivity of half-Heusler compounds from first-principles calculations, Phys. Rev. B, 84 (2011) 104302.

[12] G. Chen, Nanoscale Energy Transport and Conversion, Oxford University Press, New York, 2005.

[13] Kubo, R. (1957) "Statistical-mechanics theory of irreversible processes. I. General theory and simple application to magnetic and conduction problem", J. Phys. Soc. Jpn. 12, 570.

[14] Green, M.S. (1951) J. Chem. Phys. 19, 1036.

[15] De Groot, S.R. and Mazur, P. (1962) Non-equilibrium Thermodynamics (North-Holland, Amsterdam), p 8.

[16] S. Plimpton, Fast parallel algorithms for short-range molecular dynamics, J. Comp. Phys., 117(1) (1995) 1.

[17] D.v.d. Spoel, E. Lindahl, B. Hess, G. Groenhof, A.E. Mark, H.J.C. Berendsen, GROMACS: Fast, flexible and free, J. Comp. Chem, 26 (2005) 1701.

[18] I.T. Todorov, W. Smith, K. Trachenko, M.T. Dove, DL_POLY_3: new dimensions in molecular dynamics simulations via massive parallelism, Mat. Chem., 16 (2006) 1911.

[19] J.C. Phillips, R. Braun, W. Wang, J. Gumbart, E. Tajkhorshid, E. Villa, C. Chipot, D. Skeel, L. Kale, K. Schulten, Scalable molecular dynamics with NAMD, J. Comp. Chem, 26(1781) (2005).

[20] P.K. Schelling, S.R. Phillpot, P. Keblinski, Comparison of atomic-level simulation methods for computing thermal conductivity, Phys. Rev. B, 65 (2002) 144.

[21] A. Tenenbaum, G. Ciccotti, R. Gallico, Stationary nonequilibrium states by molecular dynamics Fourier's law, Phys. Rev. A 25 (1982) 2778.

[22] J.R. Lukes, D.Y. Li, X.-G. Liang, C.-L. Tien, Molecular dynamics study of solid thin-film thermal conductivity, J. Heat Transfer, 122 (2000) 536.

[23] P. Chantrenne, J.-L. Barrat, Finite size effects in determination of thermal conductivities: comparing molecular dynamics results with simple models, J. Heat Transfer, 126 (2004) 577.

[24] M. Matsui, Phys Chem Minerals, 23, 345, (1996).

[25] J. Shen, E. Xu, Z. Kou, S. Li, A coupled cluster approach with a hybrid treatment of connected triple excitations for bond-breaking potential energy surfaces, J. Chem. Phys. 132, 114115 (2010).

[26] H. J. Bolink, H. Brine, E. Coronado, M. Sessolo, Phosphorescent Hybrid Organic-Inorganic Light-Emitting Diodes, Adv. Mater. 22, 1 (2010).

[27] J. M. Larkin and A. J. H. McGaughey, PHYSICAL REVIEW B 89, 144303 (2014).

[28] P. B. Allen, J. L. Feldman, J. Fabian, and F. Wooten, Philos. Mag. B 79, 1715 (1999).

[29] P. B. Allen and J. L. Feldman, Phys. Rev. B 48, 12581 (1993).

[30] J. M. Ziman, Electrons and Phonons (Oxford University Press, New York, 2001).

[31] J. L. Feldman, M. D. Kluge, P. B. Allen, and F. Wooten, Phys. Rev. B 48, 12589 (1993).

[32] J. L. Feldman, M. D. Kluge, P. B. Allen, and F. Wooten, Phys. Rev. B 48, 12589 (1993).

[33] J. L. Feldman, P. B. Allen, and S. R. Bickham, Phys. Rev. B 59, 3551 (1999).

[34] X. Liu, J. L. Feldman, D. G. Cahill, R. S. Crandall, N. Bernstein, D. M. Photiadis, M. J. Mehl, and D. A. Papaconstantopoulos, Phys. Rev. Lett. 102, 035901 (2009).

[35] H.-S. Yang, D. G. Cahill, X. Liu, J. L. Feldman, R. S. Crandall, B. A. Sperling, and J. R. Abelson, Phys. Rev. B 81, 104203 (2010).

[36] Y. He, D. Donadio, and G. Galli, Appl. Phys. Lett. 98, 144101 (2011).

[37] C. Masciovecchio, G. Baldi, S. Caponi, L. Comez, S. Di Fonzo, D. Fioretto, A. Fontana, A. Gessini, S. C. Santucci, F. Sette et al., Phys. Rev. Lett. 97, 035501 (2006).

[38] G. Baldi, V. M. Giordano, G. Monaco, and B. Ruta, Phys. Rev. Lett. 104, 195501 (2010).

[39] G. Baldi, V. M. Giordano, and G. Monaco, Phys. Rev. B 83, 174203 (2011).

[40] G. Baldi, M. Zanatta, E. Gilioli, V. Milman, K. Refson, B. Wehinger, B. Winkler, A. Fontana, and G. Monaco, Phys. Rev. Lett. 110, 185503 (2013).

[41] J. Horbach, W. Kob, and K. Binder, Euro. Phys. J. B: Condens. Matter Complex Syst. 19, 531 (2001).

[42] J. L. Feldman, J. Non-Cryst. Solids 307–310, 128 (2002).

[43] J. K. Christie, S. N. Taraskin, and S. R. Elliott, J. Non-Cryst. Solids 353, 2272 (2007).

[44] J. Callaway, Phys. Rev. 113, 1046 (1959).

[45] P. G. Klemens, Proc. Phys. Soc. A 68, 1113 (1955).

● Chapter 6

6 Conclusion and Future Work

6.1 Conclusion

In materials science, there have been a lot new research directions which brought many excellent achievement. For instance, the methods such as employing nanostructures to improve properties in materials science have exhibited novel techniques to enable great improvements by using just common materials. However, properties of materials in nanoscale are different from bulk or macroscale. Research of nanoscale properties such as thermal conductivity have attracted a lot of concerns. However, fabrication of uniform nanostructures and evaluation of properties in nanoscale are key issues and still difficult. In this study, the bio nano process (BNP) was employed to fabricate uniform nanostructure. Furthermore, organic materials could be imported to make hybrid structure with inorganic materials due to BNP. On the other hand, 3ω method was utilized as a measurement tool to evaluate the thermal conductivity in the out-plane direction for thin film with nanostructures. Thereby nanostructures which contain nanocomposite structure with FeO_x NPs and hybrid structure with PEG-ferritins, were embedded into thermoelectric material polycrystalline $Bi_{0.4}Te_{3.0}Sb_{1.6}$ and insulator material amorphous SiO_2 to improve the efficiency and control the thermal conduction, respectively. The results obtained in this study are important from both a scientific and an engineering point of view.

In chapter 2, the protein ferritin was selected as a cage to carry and distribute NPs on the two dimensional surface. At first, for improvement of

the absorption of ferritin, conditions of ferritin solution were optimized to a concentration of 0.01 mg/ml and ammonium acetate (AA) ion concentration of 10 mM. Furthermore, in order to improve the separation distances (SD) of NPs, modification of PEG2k, 5k, 10k and 20k were employed. The evaluation of modification by MALDI-TOF/MS and situation of PEG-ferritin in solution by DLS. Finally, distributions were evaluated by probability distribution function through SEM images of NPs. It was found that SD increased and uniformness improved with the weight of modified PEG.

In chapter 3, in order to evaluate the thermal conductivity, 3ω measurement system was set up. Through measurements of many different kinds of substrates such as glass, silicon, YSZ, sapphire, etc. and SiO_2 thin film, the system was optimized from the hardware like probe, stage, thermo-couple, etc. to the software such like value of voltage signal, frequency region, etc. of measurement. Finally, it was confirmed that the 3ω measurement system can measure thermal conductivity of thin film in the out-plane direction correctly. And this system was utilized to evaluate the thermal conductivity of thin film with nanostructures in the out-plane direction in this study.

In chapter 4, nanocomposite structure with FeO_x NPs were embedded into thermoelectric material polycrystalline $Bi_{0.4}Te_{3.0}Sb_{1.6}$ by bio nano process. At first, one-layer structure was fabricated. In order to confirm the NPs, SEM images, AFM and XPS analysis were used. After the electric properties evaluation by Hall effects measurement and direct measurement for Seebeck coefficient, it was known that the Seebeck coefficient (S) increased and

electrical resistivity (ρ) also increased due to filtering effect or de-doping of holes. Totally, the power factor (S^2/ρ) increased and this is an improvement for thermoelectric materials. On the other hand, the thermal conductivity did not have a significant change because the NPs volume ration for NPs is too small. Furthermore, in order to amplify the effects of NPs, multi-layered structures of NPs were fabricated and evaluated. According to the results of the thermoelectric measurements for electrical properties and 3ω measurement, electrical conductivity increased without a significant change in the Seebeck coefficient. In addition, thermal conductivity decreased along with the increase of layer number. Through cross-sectional TEM images, it was known that the polycrystalline film changed into amorphous when NPs are embedded. This might be the reason for the change of the electrical properties and are considered for future work. The decrease of thermal conductivity was explained as phonon scattering after comparing with the CP model calculation.

In chapter 5, in order to focus on the nanoscale thermal conduction contributed from phonons, multi-layer NPs and PEG20k-ferritin were embedded in SiO_2 thin film. The 3ω measurement results in out-plane direction showed that nanocomposite structure with only NPs raised the thermal conductivity. On the other hand, the hybrid structure with protein shell and NPs inside reduced thermal conductivity. For explanation of the phenomena, MD simulation in perturbation methods and calculations with divided phonon modes were employed to calculate thermal conductivity. Furthermore, experimental results were analyzed and proven. This method

should be a novel way to control thermal conduction in nanoscale.

6.2 Suggestions for Future Work

In this study, the most important result is the development of a serial bio nano processes to fabricate hybrid nanostructures with organic and inorganic materials, which can amplify or depress thermal conduction. On the other hand, with application of the nanocomposite structure, the efficiency of thermoelectric materials $Bi_{0.4}Te_{3.0}Sb_{1.6}$ was improved. Furthermore, compared to results of the theoretical model, deep understandings of nanoscale thermal conduction were realized. However, there are still a lot of issues left which prevent us from understanding the effects of nanostructures in thin films. The following are suggested as future work.

1. Measurement of thermal conductivity in the in-plane direction.

All the 3ω measurement in this study, is in the out-plane direction measurement. However, for applications of thin film materials, the in-plane direction 3ω measurement is important to know. For thin films, it is very difficult to measure the thermal conductivity in the in-plane direction due to thermal loss from out-plane direction. According to theoretical model of 3ω measurement, the change of width of 3ω measurement electrode and multi-pattern can solve these problems. Therefore, 3ω measurement system for in-plane direction should be a future work to evaluate nanostructures further.

2. Simulation for hybrid structure.

The MD simulation for multi-layers NPs was performed. However, the hybrid structure with organic and inorganic materials was calculated by theoretical model, the deeper analysis such as MD simulations should be done as a future work.

3. Changing the materials of NPs and thin film.

Multi-layers FeO_x NPs or PEG-ferritins within $Bi_{0.4}Te_{3.0}Sb_{1.6}$ or SiO_2 thin film, are fabricated. Through analysis of nanostructures' effect on thermal conductivity, novel methods were found to manage nanoscale thermal conduction. However, the electrical properties are bad for application in thermoelectric materials. Therefore, a change of thin film's materials, by which the electrical properties will be improved, is necessary. NPs' material should also be changed in order to make the film more efficient. A lot of materials could be used by BNP.

4. Application for flexible device

Once the thermal properties and electrical properties are improved through the optimization of materials, the applications of nanostructure which was discussed in this research, such as thermoelectric device could be expected in future. Furthermore, the flexible device should be a possible application, because all fabrication processes in this research are not high temperature processes.

● List of publications

Academic journals

Chao He, Mutsunori Uenuma, Naofumi Okamoto, Hiroki Kamitake, Yasuaki Ishikawa, Ichiro Yamashita and Yukiharu Uraoka, A distance-controlled nanoparticle array using PEGylated ferritin, Materials Research Express 1 (2014) 045410

Presented Works

International conferences (Reviewed, oral)

Chao He, et al.: "Distance Controlled Nanoparticles Using PEG-ferritin for New Functional Devices", The 2013 International Meeting for Future of Electron Devices, Kansai, June 5th, 2013

Chao He, et al.: "Control of Separation Distances of Ferritin by Polyethylene Glycol", the 2013 JSAP (Japan Society of Applied Physics)-MRS (Materials Research Society) Joint Symposia, September 16-20, 2013

Chao He, et al: "Improving Thermoelectric Properties by Nanoparticle Inclusion in Bi_2Te_3 Thin Film", The 2015 International Conference on Thermoelectrics (ICT 2015), June 28th, 2015.

Chao He, et al: “Improved Thermoelectric Properties by embedding protein shells in Thin Film”, 14th European Conference on Thermoelectrics (ECT2016), September 20-23, 2016.

International conferences (No review, poster)

Chao He, et al: “Controlled Separation Distances of PEGylated Ferritin”, The 2013 International Device Physics Young Scientist Symposium (IDYS 2013), March 4th, 2013

Domestic conferences (No review, oral)

何超、本田良一、上武央季、上沼睦典、石河泰明、山下一郎、浦岡行治：“PEG 修飾フェリチンの分散配置制御”、 第 60 回応用物理学会春季学術講演会、神奈川工科大学、3 月・2013

何超、上沼睦典、本田良一、上武央季、石河泰明、山下一郎、浦岡行治：“PEG サイズによるフェリチンの分散配置制御”、 第 60 回応用物理学会秋季学術講演会、同志社大学、9 月・2013

何超、上沼睦典、岡本尚文、石河泰明、山下一郎、浦岡行治：“PEG フェリチンの 2 次元結晶配列”、第 75 回応用物理学会秋季学術講演会、北海道大学、9 月・2014

何超、上沼睦典、岡本尚文、岡本尚文、上武央季、山下一郎、浦岡行治：“薄膜中のナノ粒子制御による熱電特性改善”、日本機械学会第６回マイクロ・ナノ工

学シンポジウム、島根県松江市くにびきメッセ、10 月・2014

Domestic conferences (No review, post)

何超、上沼睦典、藤本裕太 、石河泰明、山下一郎、浦岡行治 : “ナノ粒子制御による熱電特性の改善”、第 76 回応用物理学会秋季学術講演会、名古屋国際会議場、9 月・2015

何超、上沼睦典、岡本尚文、山下一郎、浦岡行治 : “タンパク質による有機無機ハイブリッドナノ構造の作製”、第 77 回応用物理学会秋季学術講演会、新潟県新潟市朱鷺メッセ、9 月・2016

Appendix:

Radial Distribution Function

Consider a simple atomic liquid or colloidal suspension. The average density $\rho g(r)$ at a distance r of a given particle is defined to be $\rho g(r)$, i.e.

$$\rho(r) = \rho g(r) \quad (1)$$

Here ρ is the average density in the fluid. Notice that $\rho(r)$ is a conditional density; it is the density at r, given a particle is present in the origin. A qualitative picture of $g(r)$ is given in figure 17; it is called the radial distribution function.

It is clear that $g(r)$ should go to 1 for large r. At very short r the radial distribution function must be zero. In per square meter region, $g(r)=N/(2\pi\rho \cdot dr)$, where N is the number of NPs in per square meter. Because ρ is constant, it can be ignored in calculation of most probility SD. Thus, the formula was approximated to $g(r)=N/(2\pi \cdot dr)$ in my study. Outside the van der Waals diameter, there is a peak because the remaining NPs try to diffuse into the region occupied by the one at the origin.

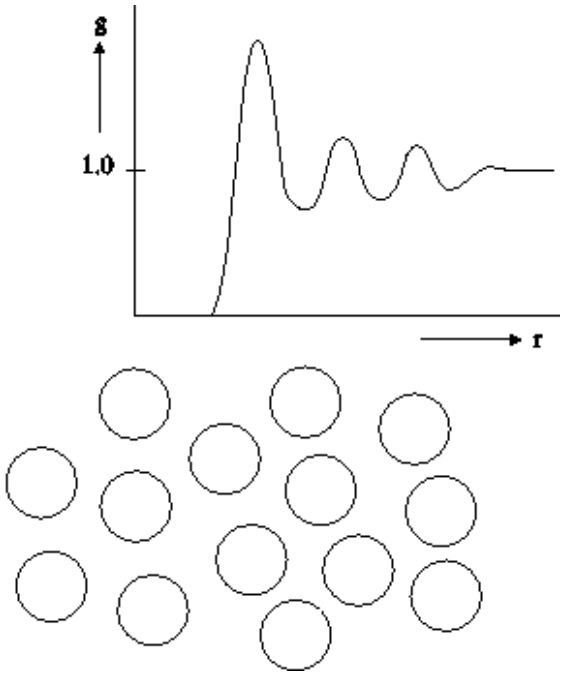

Figure 17 Schematic of radial distribution function.